Universidad de los Andes

Plasmon resonances and tunneling in sub-nanometric systems

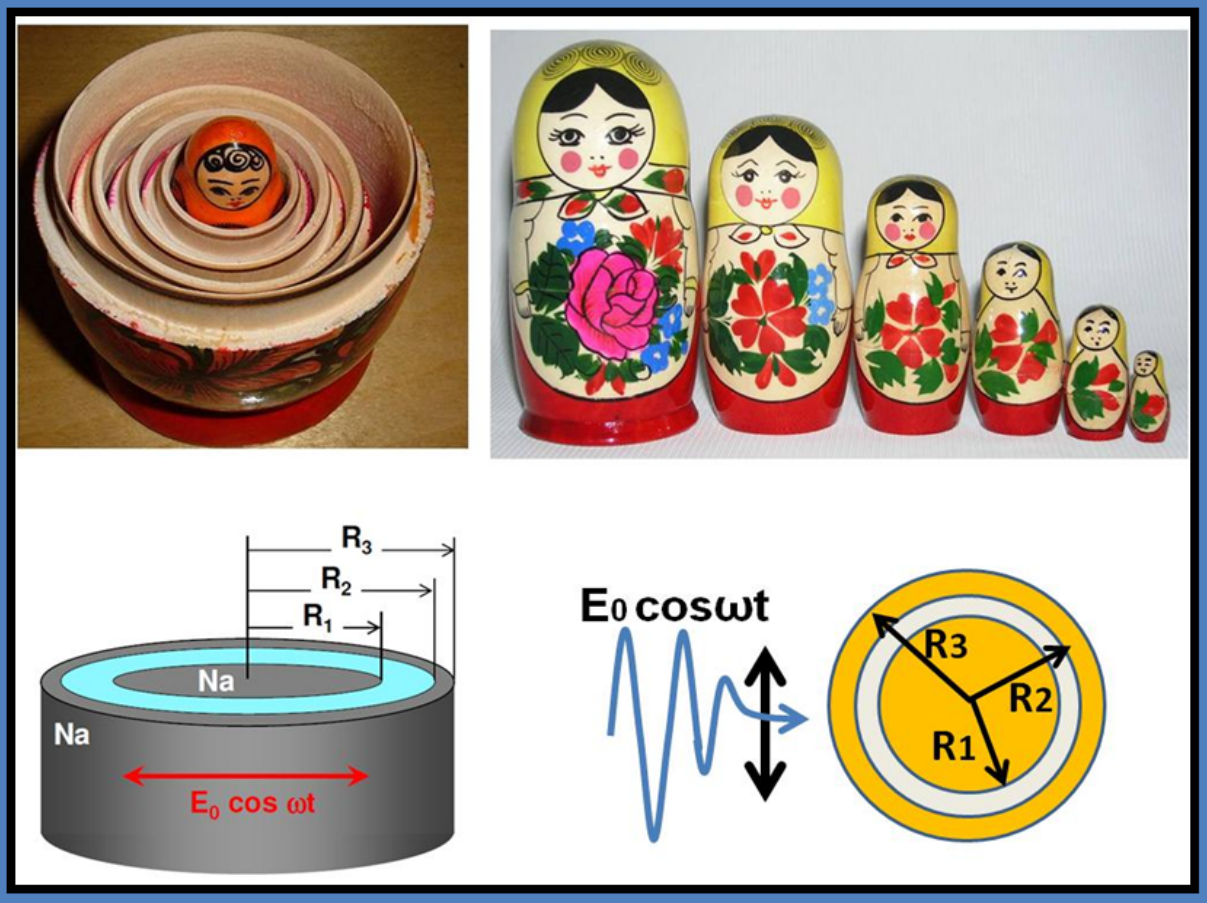

Mario Zapata Herrera

PhD Thesis

Supervised by
Dr. Ret. Nat. Angela S. Camacho B.

Department of Physics
Grupo de Física Teórica de la Materia Condensada
Universidad de los Andes

Plasmon resonances and tunneling in sub-nanometric systems

Thesis developed by

MARIO ZAPATA HERRERA

for the degree of

Doctor en Ciencias Física

Supervised by

Dr. Ret. Nat. Angela Stella Camacho Beltrán

Bogotá-Colombia, December 2015.

"Muchos años después, frente al pelotón de fusilamiento, el coronel Aureliano Buendía había de recordar aquella tarde remota en que su padre lo llevó a conocer el hielo. Macondo era entonces una aldea de veinte casas de barro y cañabrava construidas a la orilla de un río de aguas diáfanas que se precipitaban por un lecho de piedras pulidas, blancas y enormes como huevos prehistóricos. El mundo era tan reciente, que muchas cosas carecían de nombre, y para mencionarlas había que señalarlas con el dedo. Todos los años, por el mes de marzo, una familia de gitanos desarrapados plantaba su carpa cerca de la aldea, y con un grande alboroto de pitos y timbales daban a conocer los nuevos inventos. Primero llevaron el imán. Un gitano corpulento, de barba montaraz y manos de gorrión, que se presentó con el nombre de Melquíades, hizo una truculenta demostración pública de lo que él mismo llamaba la octava maravilla de los sabios alquimistas de Macedonia...

Al ser destapado por el gigante, el cofre dejó escapar un aliento glacial. Dentro sólo había un enorme bloque transparente, con infinitas agujas internas en las cuales, se despedazaba en estrellas de colores la claridad del crepúsculo. Desconcertado, sabiendo que los niños esperaban una explicación inmediata, José Arcadio Buendía se atrevió a murmurar:

—Es el diamante más grande del mundo.

—No —corrigió el gitano—. Es hielo.

José Arcadio Buendía, sin entender, extendió la mano hacia el témpano, pero el gigante se la apartó. "Cinco reales más para tocarlo", dijo. José Arcadio Buendía los pagó, y entonces puso la mano sobre el hielo, y la mantuvo puesta por varios minutos, mientras el corazón se le hinchaba de temor y de júbilo al contacto del misterio. Sin saber qué decir, pagó otros diez reales para que sus hijos vivieran la prodigiosa experiencia. El pequeño José Arcadio se negó a tocarlo. Aureliano, en cambio, dio un paso hacia adelante, puso la mano y la retiró en el acto. "Está hirviendo", exclamó asustado. Pero su padre no le prestó atención. Embriagado por la evidencia del prodigio, en aquel momento se olvidó de la frustración de sus empresas delirantes y del cuerpo de Melquíades abandonado al apetito de los calamares. Pagó otros cinco reales, y con la mano puesta en el témpano, como expresando un testimonio sobre el texto sagrado, exclamó:

—Este es el gran invento de nuestro tiempo."

Gabriel García Márquez. *Cien Años de Soledad*

Dedicada a mis padres Magdala y Mario

Acknowledgements

The quest for knowledge from the mathematical description of Nature, for me, is one of the most beautiful adventures in the complexity of mankind and in its most fundamental version, known as physics, one of the disciplines of greatest acceptance and impact on western society, at least since the time of Galileo. This makes acknowledging in general to the whole human race for having accomplished to the end of this thesis, would be just a humble pretentiousness, from the tiny glance of a human being, fellow of the trip in this spaceship called Earth that is glimpsed from the vast universe as a "pale blue dot", in Carl Sagan's words. However, "the others", those to whom we called relatives, family or friends have gone along with nearby each story of life, in this infinite universe manifeste within us, in this journey called existence. To them, who are just oneself in another skin, they are to whom simply I give my sincere thanks for being the architects of each one of the letters, equations and results in this humble and honest interpretation of this broad universe.

First, I would to express my gratitude to God and my parents, for being the squires of my existence with their guidance, advices and for showing me that the freedom of being myself in every challenge, not only in academy, is the key to keep the horizon so far, though with the capacity of seeing it always close. I render thanks to God for them, to Magdala and Mario for being my parents, who accepted my choice of having them as family, alongside my siblings: Marta, James, Emma, Yuri, my lovely sister Marcela and my nephews and nieces. For their love and unconditional devotion, Thank you very much!.

On the other hand, I want to thank infinitely to my adviser and friend Angela Camacho. I remember thousands of times that I was not conformed at all and indifferent to everything, and your response was as mother's every time, patiently and a lot of love

in an ambient that for many reasons sometimes it turns cold. Angela: long life to you and thanks for giving so much to your country, to physics, to the University, to women scientist of the world and in special to your students. You are a fundamental part of this process.

To my dearest friends, who with their love, and despite infinite mistakes they have borne me, they deserve this starry sky that always welcome us in endless discussions, long "parrandas" and countless stories of life, poetry and science, searching a better road, a fairer world. Thanks for making of this road something sincere, a road worth to live. To Cesar Herreño, Nicolás Ávilan, Juan Carlos Arias, Julian Jimenez, Camilo Moscoso, Javier Cano, Manuel Torres, simply thanks a lot and hope to see you the rest of my life, because you have been great when I have been small in skimpy and fateful times, in Fito's words, "En tiempos donde siempre estamos solos". Thanks for being always there and giving me a lot of my life, for being great masters and being the best friends anyone can have.

To the "Pecho y Biceps": Larry Castrillon, Jorge Sánchez (muscle), JuanPa Mallarino, Alejandro Ferrero and Alejandro Mahecha, thanks for joining the last year full of stories and for always being ready to lift me up every time I was down. I will never be able to repay all you have done for me. To my first fellows in my first year of Ph.D: Felipe Mendez, Felipe Gonzalez, Nathaly Marín, Oscar Acevedo, Juan Carlos Pasto, Giovany Ruiz y Jefferson Florez, thanks for making of Uniandes my second home. To my plenitys: César Rock and Amanda, Alvarito, Dayana, Luisa Caviedes, Chema and in special to John Mora and Carolina Jimenez. Thanks for your sincerity, love, rational and irrational discussions about life, rock, women and in special for giving me a great sarcastic and definitive laugh where it was required. Thanks always for the music and giving me a home.

A special place is for Edwin Herrera: I only want to say that God give me the opportunity to know not only a friend, but a brother. Thank you for be my confidant, my best friend and for all that great light and even dark moments that we joined in this life." Gracias Parcero".

Acknowledgement to those friends who appear out of nowhere, when everything seemed to be lost. Thanks friends BAOBAB and people from “Accesa Centro de Liderazgo”, in special to Andrea Cortés, Andrea Camacho, Yamile Casallas, Helen Gorder, to my coach and great “santafereño” Holman Borda. Thanks for the gift of love and for learn me to “trust” and for playing the game “Ganar Ganar”. A heartfelt “4” for everyone. To my friends from Quimbaya: my soul friends from the Banda Municipal, specially my brother Kurt and Báquiro (baby!). Dorita and Maria Antonia: you have a part of my heart. Thanks to Aleja Salazar, Sandra Velez and Orlando Rojas. Also my foster parents in Armenia Sandra Vera and Julian Ramirez: “un dios les pague” for this last months in Quindío writing my thesis. Also special thanks to Alejandra and Santi Granada for letting me use their great “café de altura” as an office.

Agradecimientos especiales a Jhuliana Rojas por ser parte de mi vida en momentos de mucha felicidad y amor. Gracias a tus hijas Sarita y Paulita. Gracias por poyarme en todo momento y por creer en mi.

I want to thank to my family, in special my grandparents Octavio and Franquelina, uncle Arturo and Blanquita, uncle Gilberto (Mono) and my cousin Lina Riveros, uncle Diego and very deeply to my aunt Mary and her husband Germán and my cousin Dianita (primeins) for their support and make me at home when I did not have one. Thanks for making of Tofi the first dog, at least in the family, to be part in a doctoral thesis. To Claudina Matinez and Eduardo Muñoz: You have a special part of my heart, as well as Nico, Natalia and my dear cousin Mona (Monica Melissa). No words can express my deep feelings and love I have for you, and how beautiful it is to write these lines knowing you are part of my life as two squires, despite of my imperfections as human being. Thanks to my uncle Benji and my aunt Patty in Madrid: You give me the best moments and turism in Spain.

Thanks to professor Camilo Espejo and Hanz Ramirez. You were very kind to share with me codes, methods, bibliography and very valuable help in several academic and spiritual discussions. Likewise to Universidad de los Andes, the Facultad de Ciencias for financial support through all my “Proyectos Semillas”. To the directors of the Department of Physics during my PhD program, Carlos Avila and Gabriel Tellez and all the administrative staff: Johana, William Paiba, Julieta Rodriguez and Luis Anibal. Special thanks to Rubén Esteban for introducing me in the QCM calculations and Codruta Marinica for

sharing me codes, information and very productive conversations in Donosti and Paris. To the people of Centro de Física de Materiales and the Donostia International Physics Center in the Basque Country, thanks fot financial and academic support. I made there the major part of this work. Thanks for facilitate my stay during three visits in less than two years.

To my kindly friends in "la bella Easo": my dear "ser de luz" Manuel Blanco, thanks for be the link with my other friends there and invite me to be a part of the "'cuadrilla". Thanks to Christian Fernández (Cheito), Camilo Cortés, Lina Gutierrez, Johana Brito, David Amico, Wissem (el Túnez), Ammen Poyli, Holanda Gomez and Sarita Quin for making my stay one of the most wonderful experiences in my life. Very good memories to Salomé Valencia and Karen Alonso, thanks for your lovely friendship, help and for visit me. To Nena (Miryam Helena López), Nana, Jorge Hugo Ossa, Nicolás Esquivel, Jorge Molina and Andrés Pitarra in Paris. Merci beaucoup!

Before concluding, I would like to express my gratitude to all of colombian people who pay honestly their taxes. You make possible to people like me to accomplish science education, in a country where unfortunately, science is not funded like army and fight against war. Thanks to COLCIENCIAS for supporting this doctoral program. I can assure you that the money was invested in the best hands.

Last but not least important, I would like to dedicate these last lines to two of the most important people I have ever known in my history as a physicist. Lehenik eta behin, Javier Aizpuruari, zeinak bere adeitasun, konfiantza eta ardurarekin posible egin baitzuen nire egonaldia Nanofotonikako taldean, Donostiako Materialen Fisikarako Zentroan. Mila esker ezagutzen ez zenuen norbaitengan konfiantza izatearren eta beti ongi etorria den eskua luzatzearren; fisikari buruzko eztabaidengatik eta nire kezka eta galderentzat beti tarte bat aurkitzearren; munduan nanoplasmonika eta nanozientzia gara daitezen laguntzearren, nigan konfiantza izatearren, betidanik parte izan nahi nuen mundu bat ezagutaraztearren, eta beste behin ere karrera miresgarri honetan sinesteko aukera oparitzearren. Mila esker, bihotzez.

Finally, I want not only say thanks, but praising the great human spirit of Andrei Borisov, to whom I met in Donosti during my first visit to CFM and ISMO and from whom I

got the best image of an universal man, from a human being who transcends language, cultural and social frontiers in honor of knowledge and reason. From you, dear Andrei, I hope I have not learnt everything yet, I hope to keep your support, long discussions on science, Europe and about the world. Thanks for being my (non-official) adviser and for making me fell in love with physics and especially because I will never forget your words of encouragement in moments of great despair: "I can tell you is that is what you have to keep on going, and one day the life will be full of colors once again. And with little chance you might decide that somebody was right above forcing you to go-through what you are going now. Well, in any case, we have to believe that anything happens that our life will drive onto a better road. You have so many friends. This should help". Now, Andrei, the world is full of colors. You were completly right one more time. Thank you.

Mario Zapata Herrera,

Quimbaya, Colombia.
Bogotá, Colombia.
Donostia-San Sebastián, Spain. December 2015

Abstract

One of the most promising and most active nowadays research field in nanoscience, is the field of *Nano-Plasmonics*, which describes the light interaction with nanostructured metallic systems. The optical response of these nanostructures is determined by a collective resonance of conduction electrons which depends on geometrical and compositional factors as well as on the frequency and polarisation properties of the incident light. For large systems of tens of nanometers in size and above, this response is well understood, and can be confidently described by classical Maxwell equations. At the same time, for plasmonic nanoparticles of some nm size and below, or for plasmonic nanostructures characterised by narrow subnanometric gaps between nanoparticles, the quantum effects due to the non-local screening and tunneling emerge. These quantum effects are not captured by standard classical descriptions which is then a real challenge for the theory. Indeed, (i) Nowadays technology allows controllable engineering of such structures which asks for theoretical predictions; (ii) Quantum effects can strongly affect the plasmonic resonances of a hybrid nanostructure as has been demonstrated for e.g. small metallic clusters, plasmonic dimers and core-shell nanoparticles. Thus, effective electron tunneling across these gaps alters both the far-field optical response and the near-field confinement and enhancement. While generally, quantum descriptions using full quantum mechanical calculations like Time Dependent Density Functional Theory (TDDFT) are needed to account for quantum effects in subnanometric gaps, recently developed so-called Quantum Corrected Model (QCM) [1, 2] allows to incorporate electron tunneling within the framework of classical Maxwell equations. In this approach, the gap is filled with an effective medium characterized by a tunneling conductance. The advantage of this methodology is that it allows to tackle large (realistic) plasmonic systems with millions of atoms which is at present out of reach for the quantum descriptions.

In this thesis we have theoretically studied the optical response of several canonical systems with narrow gaps: nanoparticle pairs (dimers), and core-shell systems (known in literature as nanomatryoshkas), in the subnanometric regime (systems below 10 nm). As a first approach, we have used classical electromagnetics treatment allowing a link with previous studies and characterisation of the plasmonic modes and near and far fields. We have explored the physics of the plasmon coupling and near field enhancements in plasmonic cavities upon reduction of the gap size, where classical theory predicts extremely strong effects because of the attractive Coulomb interaction between plasmon induced charges across the junction [3]. For the vanishing width of the junction this interaction diverges leading to the discontinuities in classical theory [4]. This is precisely the regime where quantum effects like tunneling are of paramount importance as they neutralise the screening charges and allow continuous transition from the capacitive to inductive coupling at zero gap size (continuous metal in the junction).

In a joint experimental and theoretical study (in a work performed in collaboration with an experimental group[1]), we have investigated the plasmon coupling in gold nanomatryoshkas with different core-shell separations. In agreement with experimental data the effects of the hybridization between the core and the shell plasmons become significant for the gap widths below 15 nm. When the gap width decreases to below 1 nm, the near- and far-fields can no longer be described by classical approaches but require the inclusion of quantum mechanical effects such as electron transport through the self-assembled molecular monolayer present in the junction. Surface-Enhanced Raman Scattering measurements indicate strong effects because of the charge transfer across the molecular junction. In this respect, we found out that quantum modeling provides an estimate for the AC conductance of molecules in the junction. The insights acquired from this part of the work, pave the way for the development of novel quantum plasmonic devices and substrates for Surface-Enhanced Raman Scattering (SERS) [5].

In the combined effort with research groups from Spain [2] and France [3], we have proposed a mechanism for fast and active control of the optical response of metallic nanostructures, based on exploiting the quantum regime of subnanometric plasmonic gaps. We

[1] Jian Ye Group. School of Biomedical Engineering and Med-X Research Institute, Shanghai Jiao Tong University.

[2] Javier Aizpurua, Nanophotonics Group. Materials Physics Center and Donostia International Physics Center. Donostia-San Sebastian-Spain.

[3] Andrei. G. Borisov. Institut des Sciences Moléculaires d'Orsay, Université Paris Sud, Paris-France.

demonstrated that by applying a DC bias across a narrow gap in core-shell nanostructures (cylindrical nanomatryoshkas) a substantial change of the tunneling conductivity across the junction can be induced at optical frequencies. In turns this modifies in a reversible manner the plasmonic resonances of the core shell systems. We demonstrate the feasibility of the concept of active control using time dependent density functional theory calculations. Thus, along with two-dimensional structures, metal nanoparticle plasmonics can benefit from the reversibility, fast response times, and versatility of an active control strategy based on applied bias. The proposed electrical manipulation of light using quantum plasmonics, establishes a new platform for many practical applications in optoelectronics [6].

Finally, using time dependent density functional theory (TDDFT) we performed the full quantum calculation of the optical response, stability, and electron loss for charged spherical clusters. We have obtained that, because the system stays neutral in the bulk, and the extra-charge is localized at the surface of the cluster, the dipolar plasmon mode displays only small frequency shift linked with change of the electron spill-out from the nanoparticle boundaries [7]. We have also shown that even small ($\sim 10\,\%$ relative to the total number of electrons in the system) negative charge raises Fermi level of the cluster above the vacuum level and renders the system unstable. The extra charge of the cluster decays with characteristic time constants that can be fully understood using an analytical study based on the WKB method, similar to the studies of the alpha-decay. Our results on the charged clusters allow to critically reinterpreting many of the experimental data obtained with electrochemistry, where the shift of the plasmon resonances has been attributed to the charging effects. Based on our results, we tentatively propose an alternative explanation based on the change of the dielectric environment in immediate vicinity of the cluster.

Contents

Chapter 1

Introduction

One of the greatest advances in the description of the physical properties of materials in the last century concerned an understanding of the properties of matter in the so-called low dimensional systems. The interaction of light and matter has allowed probing the deepest secrets of the physical nature of our universe, by analyzing the exchange of energy and momentum between photons and the electrons of the materials. Furthermore, this interaction has helped to develop many technological applications that have contributed to the spectacular technological development in the twentieth and twenty-first centuries. In this context, the control and manipulation of light has been limited by diffraction, which provides an intrinsic limit to the spatial location below the wavelength. It is only recently that the advances in nanofabrication techniques made it possible to design and built nanostructured materials allowing to manipulate light at the scales below the wavelength [8–10]. We present in this chapter the main generalities of a field of *plasmonics* aimed at the fundamental and applied studies of the light interaction with nanostructures supporting collective electronic excitations, plasmons.

1.1. Plasmonics

Some nanomaterials have the ability to localize light below the diffraction limit due to their electronic excitations. Specifically, metals exhibit a coherent collective excitation of the conduction electrons, commonly called *plasmon*. When metals are structured in the form of nanoparticles, these plasmons are localized in the dimensions of the nanoparticle, resulting in a distribution of the associated optical field, which beats the diffraction

FIGURE 1.1: Lycurgus cup. A dichroic glass cup with a mythological scene. Late Rome, 4th century AD. This extraordinary cup is the only complete example of a very special type of glass, known as dichroic, which changes color when held up to the light. The opaque green cup (left) turns to a glowing translucent red (right) when light is shone through it. The glass contains tiny amounts of colloidal gold and silver, which give it these unusual optical properties. The reason for this dichroism comes from plasmonic effects. (Image and text: British Museum webpage http://www.britishmuseum.org/)

limit, and allows to locate and manipulate light in dimensions well below the wavelength[1]. The nanolocalization of light attracts a fundamental interest, and moreover it holds a great promise of numerous practical applications, which explains the outstanding development of the field of plasmonics over last years.

Historically speaking, plasmon phenomena have been used by humanity since design of the colors of the stained glass windows in medieval cathedrals, or even older, since roman 4th century AD with beautiful example given by the Lycurgus cup (see Fig. 1.1). However, the understanding of the underlying physics came latter with works of Gustav Mie [11], who derived in the beginning of the twentieth century an analytical solutions to the Maxwell equations in matter, describing the scattering and absorption of light by spherical particles. The quantum description has been provided in works of Rufus Ritchie [12] in the mid-twentieth century, who studied collective excitations of the conduction electrons in a free electron metal using a hydrodynamical model (HDM). This kind of excitations have been an important part of the study of the optical response of

[1] In this work, we only refer to localized surface plasmons in metallic nanoparticles. There is another kind of plasmon resonances refered to surface propagating plasmon excitations, which are not subject of this thesis.

matter under the incidence of electromagnetic waves [13]. Nowadays, research in plasmonics is aimed at the technological applications, mainly on exploiting the enhancement of the optical fields [14–16] in the metal nanoparticles (or near field enhancement) vicinity. Thus, significant developments are achieved in the field of sensor technology [17, 18], nanoantennas for single molecule detection [19], medical research [20], optical information transfer [21], single photon generation [22], control and generation of nonlinear effects [23], photochemistry [24], heat generation and injection of hot electrons [25], that facilitate among others, chemical reactions. The technological progress makes it possible to produce the characteristic geometries of plasmonic systems such that the quantum effects start to be important. Because of the tunneling and non-local screening the classical electromagnetic theory based on the solution of Maxwell equations with local dielectric description of the media cannot be applied. Quantum treatment and modeling are needed in this case, which stimulated efforts in full quantum calculations (like TDDFT), or in simplified effective models (like QCM) [1, 2, 26, 27] in order to calculate the optical response of metallic nanoparticles [28].

1.1.1. The dielectric function

Within the classical approach, the plasmon phenomena are addressed with the solution of electrodynamical Maxwell's equations. The materials are characterised by the dielectric function ε. The sharp material boundaries are typically assumed, and the spatial dispersion of the material response is neglected so that only the frequency-dependence of the dielectric function is accounted for $\varepsilon = \varepsilon(\omega)$.

The displacement vector $\vec{D}(\vec{r}, t)$ and the electric field $E(\vec{r}, t)$ of an isotropic, linear and homogeneous material are related in the reciprocal space $(\vec{k}, \omega)$ by a constitutive equation, including the dielectric function $\varepsilon(\omega)$, which is given by

$$\vec{D}(\vec{k}, \omega) = \varepsilon(\omega)\vec{E}(\vec{k}, \omega), \tag{1.1}$$

where the local dielectric function of the metal $\varepsilon(\omega)$ can be obtained either from empirical data or theoretically approximated with e.g. the well-known *Drude Model* (DM). In this model, one considers the conduction electrons as a free electron gas with a density n of charges per unit volume moving on a background of positive ion cores. The electrons are non-interacting within this model and all the information about realistic band structure

is contained in the electron effective mass m_e [13]. Starting with a classical equation of motion for an electron in a plasma under the influence of an external electric field $\vec{E}(t) = \vec{E_0}e^{-i\omega t}$, and assuming a harmonic response, the dielectric function of a metal can be obtained in the following form

$$\varepsilon(\omega) = \varepsilon_\infty - \frac{\omega_p^2}{\omega^2 + i\gamma\omega}. \tag{1.2}$$

In Eq.(1.2) ϵ_∞ represents the dielectric screening due to the interband transitions ($\epsilon_\infty = 1$ for vacuum).

$$\omega_p = \sqrt{\frac{ne^2}{\varepsilon_0 m}} \tag{1.3}$$

is the bulk plasma frequency defined in terms of the electron density n, the electron charge e, the electron effective mass m and the free space electric permittivity ε_0. Finally, γ is the excitation damping rate, which is a phenomenological quantity that accounts many of the posible electron interactions and allows us to do classic or quantum approaches. Eq.(1.2) gives a good description of dielectrical properties of metals in bulk and in large nanoparticles. In small metal nanoparticles with a very high surface to volume ratio, surface scattering of conduction electrons leads to the increased plasmon damping rate. The surface contribution can be accounted for in descriptions of the plasmon response of small nanoparticles modifying the damping term in Eq.(1.2) $\gamma \to \gamma(R)$ [29], where R is the mean nanoparticle radius, and

$$\gamma(R) = \gamma_{Bulk} + \frac{Av_F}{R}. \tag{1.4}$$

Here v_F is the metal Fermi velocity and A is a geometrical parameter.

Using Eq.(1.2) (taking $\varepsilon_\infty = 1$), we can separate the dielectric functon into the real $\varepsilon_1(\omega)$ and imaginary $\varepsilon_2(\omega)$ parts.

$$\varepsilon_1(\omega) = 1 - \frac{\omega_p^2\tau^2}{1 + \omega^2\tau^2} \tag{1.5}$$

and

$$\varepsilon_2(\omega) = \frac{\omega_p^2\tau}{\omega(1 + \omega^2\tau^2)}. \tag{1.6}$$

The parameter $\tau = 1/\gamma$ corresponds to the relaxation time of the free electron gas τ, given by the inverse of the collision frequency γ from Eq.(1.4). By means of the dielectric function defined in Eq.(1.2), is possible to obtain the refractive index η (related with the polarization), and the extinction coefficient κ of a system (related with the optical absorption) through the equations

$$\begin{aligned} \eta^2 &= \frac{\varepsilon_1}{2} + \frac{1}{2}\sqrt{\varepsilon_1^2 + \varepsilon_2^2}, \\ \kappa &= \frac{\varepsilon_2}{2\eta}. \end{aligned} \tag{1.7}$$

From these expressions, the main optical features of the macroscopic matter can be derived, and constitute the starting point as input parameters for most of the standard numerical calculations. In Fig. 1.2, we show the real and imaginary parts of the dielectric function for noble metals comparing experimental data (Johnson and Christy [30] and SOPRA database [31]) and from the theoretical Drude model. We can obtain a dielectric function using a Drude model depending of a nanoparticle radius as suggest Eq.(1.4). We present in Fig. 1.2, the case for $R = 1$ nm. We will address the nanoparticle size effects in the effective dielectric function below in this manuscript. Obviously the Drude model does a good job in describing the dielectric properties of the noble metals for the frequencies below the onset of the interband transitions involving the d-band electrons.

1.1.2. Plasmon resonances and nanoparticles

In systems like nanoparticles, the plasmon resonance has a surface localized nature, known commonly as Localized Surface Plasmon Resonance (LSPR), in which the whole electron gas oscillates with respect to the fixed lattice of positive ions in a resonant motion that depends both on geometrical and compositional parameters. A representation of this effect is shown in Fig. 1.3. The effect of the LSPR in a small sphere or radius R, can be explained from its frequency-dependent polarizability $\alpha(\omega)$. In the electrostatic limit it is given by [13]

$$\alpha(\omega) = 4\pi R^3 \frac{\varepsilon(\omega) - \varepsilon_d}{\varepsilon(\omega) + 2\varepsilon_d}. \tag{1.8}$$

where ε_d represents the dielectric constant of the surrounding medium. The resonant condition occurs at localised dipole plasmon frequency ω_{DP} when $\mathrm{Re}[\varepsilon(\omega_{\mathrm{DP}})] = -2\varepsilon_d$. At LSPR, the nanoparticle acts as an oscillating dipole with a strong absorption and

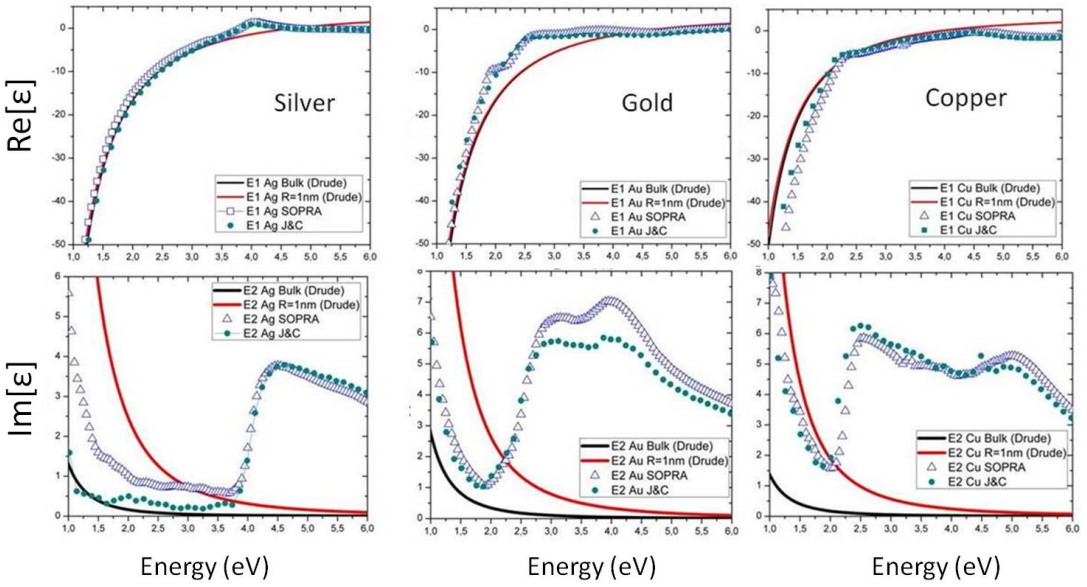

FIGURE 1.2: Real (upper figures) and imaginary (lower figures) parts of the dielectric function of noble metals (silver, gold and copper) showing the Drude Model and experimental data base from SOPRA database (triangles) [31] and the well known data from Johnson and Christy (green points) [30]. The theoretical Drude model for bulk and nanoparticles ($R = 1$nm and $A = 0.25$) corresponds to continuous lines (black and red respectively).

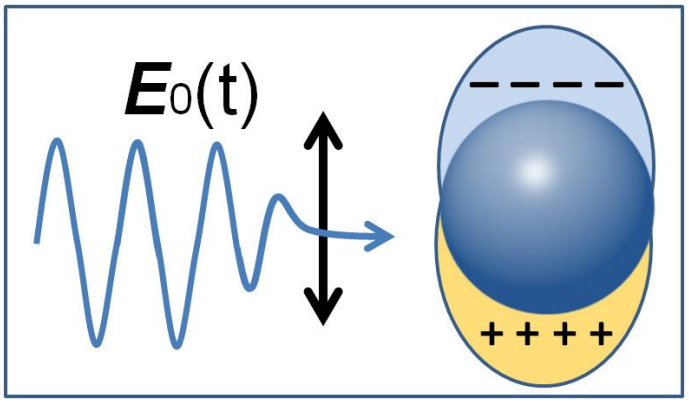

FIGURE 1.3: Schematic illustration of a localized surface plasmon. In resonance, the whole electron gas can oscillate respect to the fixed lattice of positive ions known as Localized Surface Plasmon Resonance (LSPR).

scattering features. Scattering of light can be defined as the redirection of electromagnetic waves when they meet with an obstacle. The total extinction cross-section is the amount of energy removed from the incident field due to absorption and scattering. By energy balance, the extinction cross-section σ_{ext} is a superposition of the scattering σ_{sca}

and absorption cross-sections σ_{abs}:

$$\sigma_{ext} = \sigma_{abs} + \sigma_{sca}. \tag{1.9}$$

When the obstacle is a spherical nanoparticle of radius R, the scattering σ_{sca} and absorption σ_{abs} cross-sections can be expressed in terms of the resonant polarization α, given in the electrostatic limit by [32]

$$\begin{aligned} \sigma_{scat} &= \frac{k_d^4}{6\pi}|\alpha|^2 \quad = \frac{8\pi}{3} k_d^4 R^6 \left| \frac{\varepsilon - \varepsilon_d}{\varepsilon + 2\varepsilon_d} \right|^2, \\ \sigma_{abs} &= k_d \, \mathrm{Im}[\alpha] = 4\pi k_d R^3 \mathrm{Im}\left[\frac{\varepsilon - \varepsilon_d}{\varepsilon + 2\varepsilon_d} \right], \end{aligned} \tag{1.10}$$

where $k_d = \omega\sqrt{\varepsilon_d}/c$ is the wave number of the incoming light in the embedding dielectric medium, and c is the speed of light in vacuum. Obviously the scattering and absorption cross-section are resonantly enhanced at $\omega = \omega_{\mathrm{DP}}$. The effect of the plasmon resonance is notable not only in the far field response (scattering, extinction and absorption cross section), but in the near-field response. The electric field is enhanced in the vicinity of the nanoparticle. In brief, these are the main features of LSPR which can be retrieved in a rigorous retarded solutions of the electrodynamic Maxwell equations. In the left panel of Fig. 1.4 we show the optical response of a silver sphere of radius 20 nm obtained from the solution of Maxwell's equations with appropriate boundary conditions [33]. The scattering and absorption cross-section are shown in the left panel of the figure, and the field enhancement at resonance (λ =360 nm) is shown in the right panel of the same figure. We define the near Field Enhancement Factor (FEF or EF) as the norm of the ratio between the scattered near field of the spherical nanoparticle $\vec{E}$ and an incident z-polarized electric field $\vec{E}_0$

$$\mathrm{EF} = \frac{|\vec{E}|}{|\vec{E}_0|}. \tag{1.11}$$

The resulting induced fields, are those of the dipolar electric resonance and show the expected dipolar field distribution, where there is a strong local field enhancement near the particle.

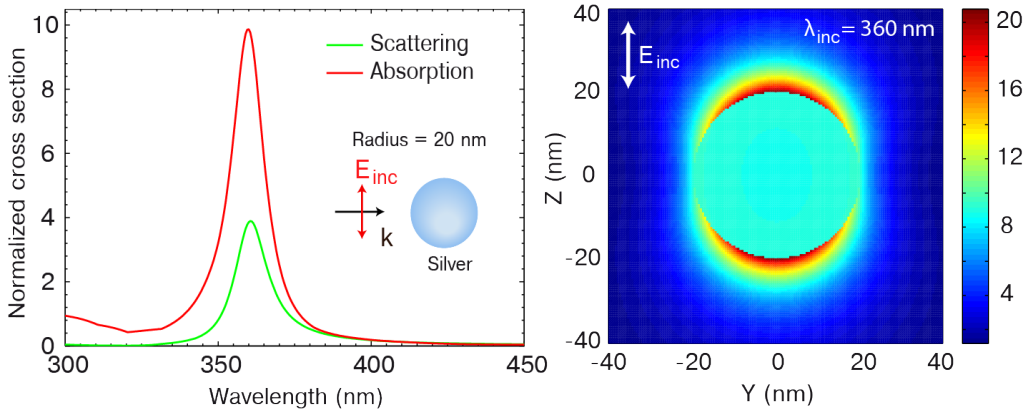

FIGURE 1.4: Optical response of a silver nanosphere with $R = 20$ nm. Left: Scattering and absorption cross sections of the particle normalized to the surface area of the sphere. Right: amplitude of the electric near-field enhancement around the nanoparticle at the dipolar resonance ($\lambda = 360$ nm). Image taken from reference [33]. Reprinted with kind permission of the authors.

1.1.3. Near Field Enhacement Factor

The near field enhancement at plasmon resonance can be illustrated with solution of Maxwell equations in matter, formulated for the scattered electric field $\vec{E}$ as [34]

$$\nabla \times \mu_r \left(\nabla \times \vec{E} \right) - k_0^2 \left(\epsilon_r - \frac{i\sigma}{\omega \epsilon_0} \right) \vec{E} = 0, \tag{1.12}$$

where μ_r is the relative permeability (taken as $= 1$ for metallic systems), ε_r the complex relative permittivity, σ is the nanoparticle conductivity related with $\varepsilon(\omega)$ through

$$\varepsilon(\omega) - 1 = i \frac{4\pi\sigma}{\omega} \tag{1.13}$$

and $k_0 = \omega\sqrt{\varepsilon_0 \mu_0} = \frac{\omega}{c}$, with c, ε_0 and μ_0 the corresponding values of light velocity, the permeability and permittivity in vacuum, respectively.

To solve the problem of light-nanoparticle interaction given by Eq.(1.12), we use the frequency dependent Drude dielectric function $\varepsilon_r(\omega)$ as an input. The vector Maxwell equations (in our case, only for the electromagnetic field) are then solved numerically, by means of, for example, a standard numerical Finite Elements Method (FEM) as included in packages like COMSOL Multiphysics [34].

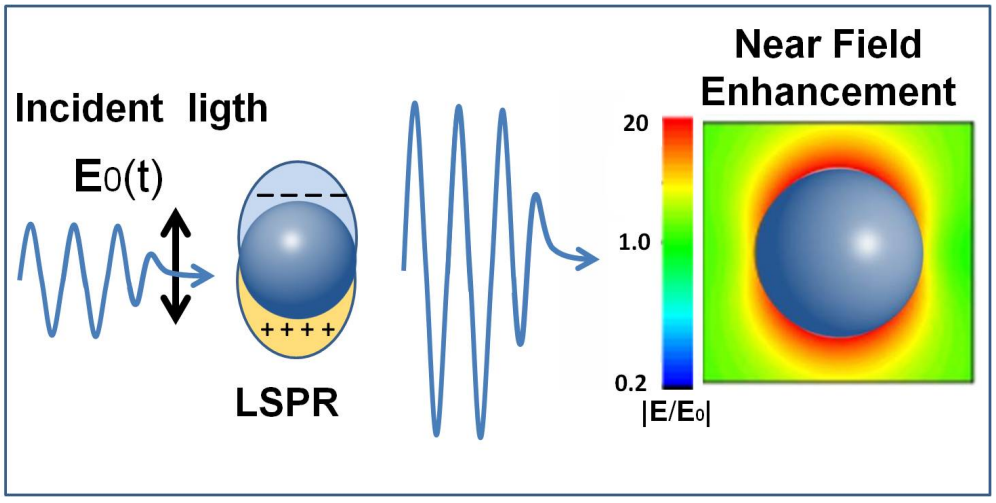

FIGURE 1.5: Sketch of the enhancement field factor calculation. An incident electromagnetic wave generates a strong near (local) field in the nanoparticle's vecinity. The EFF is definded by Eq.(1.11)

A schematic picture of the system is shown in Fig. 1.5, where an incident electromagnetic field over a nanoparticle system is shown together with a map of the field enhancement. The dielectric function of silver is obtained via Eq.(1.7) using the empirical data for the frequency ω- dependent optical constants η and κ as provided by Johnson and Christy [30].

1.1.4. Nanoparticle dimers and coupling

One of the most dramatic effects of metal nanoparticles, is their ability to exhibit extraordinary large enhancement of the near field, when they are placed in close proximity. It is well-known that the plasmon resonances of metallic systems of nanoparticles provide at optical frequencies, fields responsible for an electromagnetic contribution to Surface-Enhanced Raman Scattering (SERS) [19]. When metallic nanoparticles are used as SERS substrates, variations in SERS enhancement (often by many orders of magnitude) have been observed. This variation has been attributed to localized plasmons formations at the gaps between nanoparticles. Here, the interaction of the induced charges at opposite sides of the junction gives rise to the strong red-shift of the plasmon modes with decreasing width of the gap and large field enhancements that enable SERS detection at or near single molecule sensitivity.

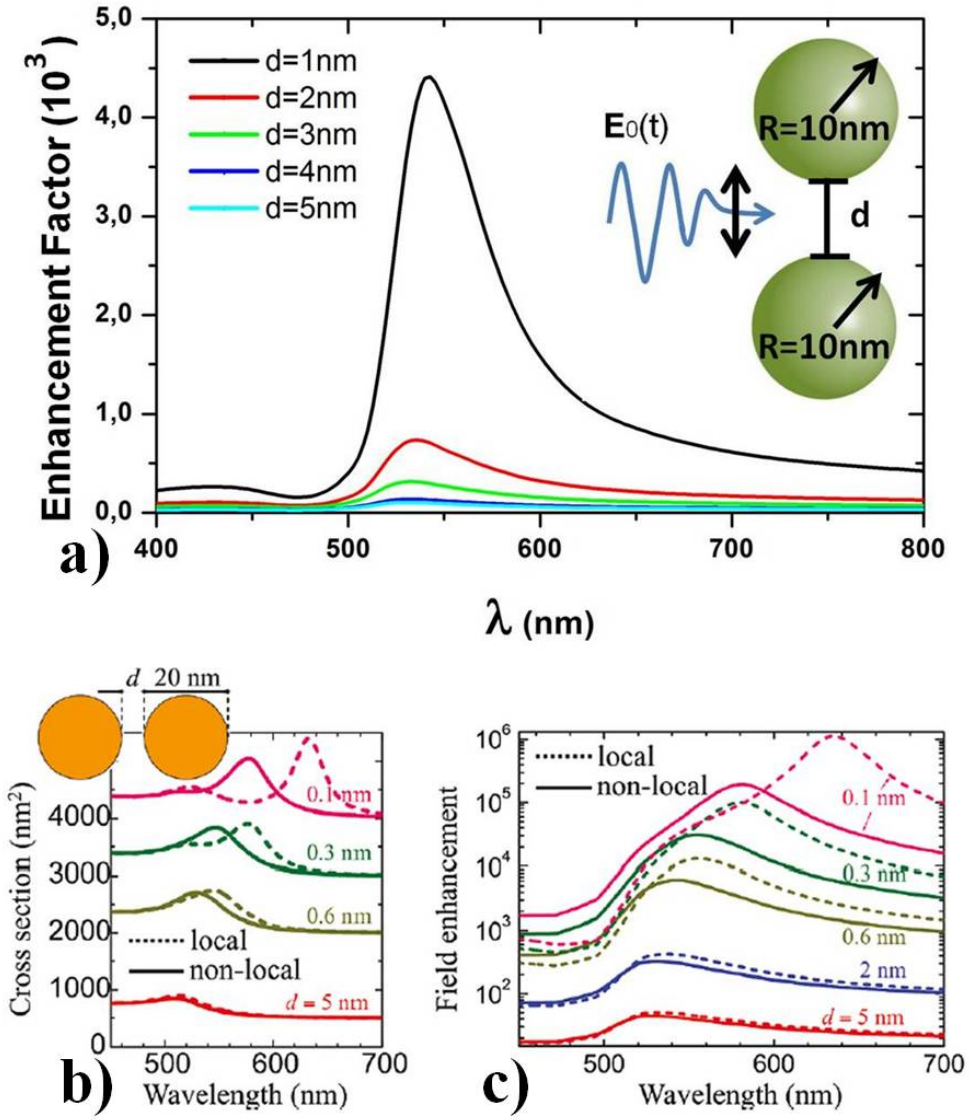

FIGURE 1.6: a) Enhancement electric field factor for a dimer composed from two gold nanospheres with $R = 10$ nm. The field enhancement is measured in the geometrical middle of the structure and the light is linearly polarized along the symmetry axis that contains the centers of the nanospheres. b) and c) present the extinction spectra and electric field intensity (respectively) calculated for gold dimers $R = 20$ nm both with (solid curves) and without (dashed curves) consideration of nonlocal effects. Different gap distances d are considered, as labeled. In this image, b) and c) are taken from [16], Copyright 2008, American Chemical Society.

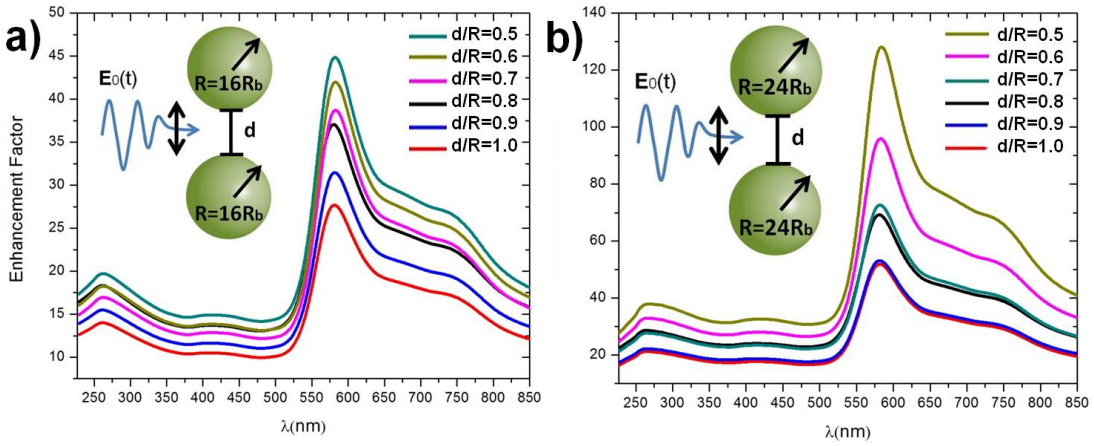

FIGURE 1.7: EF using classical electromagnetic theory in gold dimers of $R = 16R_b$ (left) and $R = 24R_b$ (rigth), where $R_b = 0.0529$ nm is the Bohr radius. The field enhancement is measured in the geometrical middle of the structure and the light is linearly polarized along the symmetry axis that contains the canters of the nanospheres. Classical theory gives a continuous increase of the electric field between particles as the distance d decreases in opposition to quantum effects in very narrow gaps, where effects like tunneling must be considered.

At resonance, as we said, very strong field enhancements are obtained. The way to obtain these high EF, requires to solve the full vector Maxwell equations using analytical or numerical methods. We present in Fig. 1.6.a, the effect of the size of the plasmonic gap d (defined in the inset) on the field enhancement in the middle of the cavity formed by a dimer of identical gold nanospheres of radii R=10 nm. Results are obtained from the Finite Element Method (FEM) solution of classical Maxwell equations, and are displayed as function of the wavelength of the incoming plane wave radiation. The studied sizes of the gap between nanoparticles range from d=1 nm to d=5 nm, where the quantum effects are expected to be weak so that the classical electromagnetic theory can be used. Observe a monotonous growth of the field enhancement at plasmon peak as the separation d between nanoparticles decreases. Nanoparticle dimers may serve as a simple prototype model system for the study of the important physical factors underlying the electromagnetic field enhancements [35]. From a classical point of view, this behavior is understood due to the interference of the fields produced from the single particle's resonances, and as an edge effect in the cavity formed by the particles [36]. These intense and highly localized fields are known in literature as "hot spots" and appear not only in spherical dimers, but in systems with more than two particles and not necessarily of spherical geometry. Upon reduction of d the field enhancement can reach several orders of magnitude as shown in Fig. 1.6.b and 1.6.c. Figures 1.6.b and

1.6.c show the extinction spectra and the EF in gold dimers of $R = 20$ nm with narrower gaps taken from [16]. The authors of this work have also considered the nonlocal effects that can reduce plasmon couplings at fixed d and thus blue-shift the resonance peak in the visible spectrum as compared to the results obtained with local dielectric function of the metal. The resonance peaks in the absorption or extinction cross section are due to the excitation of the bounding plasmon mode of the dimer and are associated with resonance field enhancement in the gap. Observe the pronounced red shift of the resonances with decreasing d which is much stronger in the local classical theory because of the divergent (at $d \to 0$) coupling between plasmon modes localised at individual nanoparticles. The coupling of the resonant modes can be analytically described using the plasmon hybridization (PH) model explained in great detail in Refs.[37, 38]. In Fig. 1.7, we show the EF obtained in this Thesis work from the classical electromagnetic theory as implemented in FEM for small gold dimers of $R = 16R_b$ and $R = 24R_b$ (where $R_b = 0.0529$ nm is the Bohr radius). Similar to the data reported in Fig. 1.6, reduction of the size of plasmonic gap results in stronger field enhancement in the junction.

Classical electromagnetic theory may be insufficient to calculate the field enhancement factor in sub nanometer (very narrow) gaps between particles. The tunneling phenomena strongly affects the optical response when the gap size is near to the touching limit (below ~ 0.5 nm in sodium dimers) [1, 39]. For the gap size $d \geq 0.5$ nm, the field enhancement increases with decreasing d, as is shown in Ref. [38, 39] (See Fig. 1.8.c and Fig. 1.8.c). Below this separation distance, the field enhancement decreases as a consequence of the increasing tunneling current which neutralizes the induced charges at the opposite sides [38] of the gap. For d approaching zero (touching limit) the field enhancement is quenched which corresponds to the continuous metal formed in the junction even prior the direct geometrical contact between metallic surfaces [38, 39].

In Fig. 1.8 we show the electric field enhancement dependence on the gap width d and spatial profiles of the near fields obtained in Ref. [38] for small free-electron metal dimers. Results of the classical electromagnetic calculations are compared with full quantum time dependent density functional (TDDFT) calculations. In this pioneering work it has been demonstrated that the classical divergence of the near fields for vanishing gap is removed because of the tunneling effects.

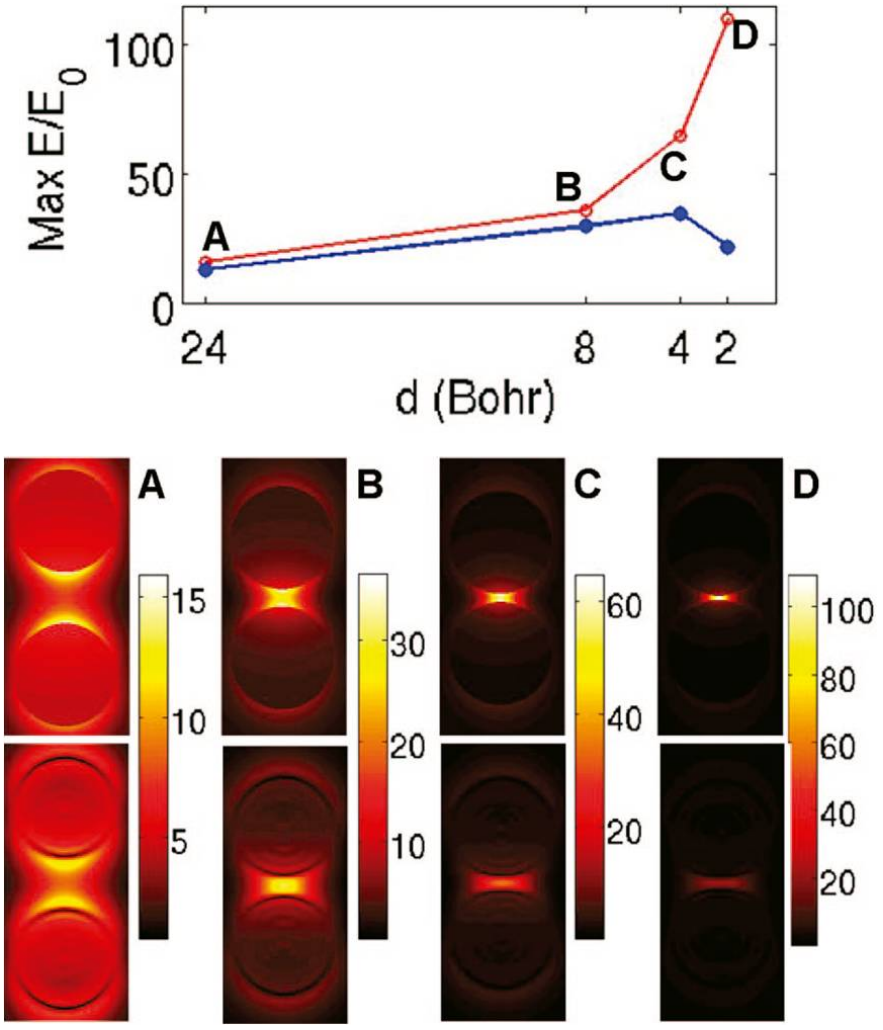

FIGURE 1.8: The upper panel shows a comparison of the maximum electromagnetic field enhancements calculated using electromagnetic calculations (red) and TDLDA (blue) for $R = 24R_b$ dimers of separations $d = 24$ (A), 8 (B), 4 (C), and 2 R_b (D). The lower panels compare the field distributions calculated using classical model (top panels) and TDLDA (bottom panels). Image taken from [38], Copyright 2009, American Chemical Society.

1.2. Quantum Plasmonics

While the optical response of the systems of tens and hundreds of nanometers is well understood, thanks to the solution of the Maxwell equations in the classical electrodynamics framework, the engineering of nanostructures with characteristic scales at nanometers range and below, brings quantum effects at the focus of current research in plasmonics.

When electromagnetic radiation interacts with a metal junction with a width comparable to the characteristic size of the electron density spill out from metal surfaces, the issues of the actual position of the screening charges and of the possible electron tunneling gains the importance.

In the classical theory the induced charges are located at the geometrical surfaces of the metals, while quantum calculations position of these charges are of some Å inside or outside the metal surface depending on the metal. Thus, the "actual" size of the gap defined by the separation between screening charges is different from the geometrical size of the gap. This effect is particularly important for the range of gap widths 1 Å $\leq d \leq$ 10 Å, and it is linked with non-local dynamical screening at surfaces, phenomenon, which also controls the shift of the frequency of the plasmon modes of individual nanobjects as function of their size. The non-local screening can be partially taken care off within the framework of the classical Maxwell equations using the model non-local dielectric functions. The so-called Hydrodynamic approach is one of the most popular nowadays because of its physical transparency and numerical efficiency [40].

For even narrower gaps (below 1 nm), the electron tunneling is the dominating quantum effect which strongly affects the plasmon modes of hybrid nanostructures. Both far-and near-fields can be altered as illustrated with Fig. 1.8. As we will show in this thesis, the electron tunneling effect has a great importance as a principle of action in optoelectronics. To date, the description of this intimately quantum effect has been possible in a few nanometer scale nanostructures, in which the full quantum treatments such as TDDFT are feasible. These canonical systems comprise nanoparticle pairs (dimers), and core-shell systems (known in literature as nanomatryoshkas), where the quantum leap of the electrons is controlled by the distance between the metal surfaces of the nanoparticles forming the cavity (see Fig. 1.9). The quantum effects on LSPR have motivated the plasmonics community to critically reexamine the description of the optical response of small isolated nano-particles and plasmonic nanostructures with narrow gaps by revisiting the existing models from both classical and quantum points of view. In Figure 1.10, we show several structures presenting quantum effects. Such structures are the main systems studied in this thesis. In this kind of systems, where the quantum effects as tunneling are explicit, the calculations of the optical response represents a real challenge. Indeed, quantum treatments beyond classical electrodynamics are required, but these are computationally inaccessible nowadays for the plasmonic systems of actual interest

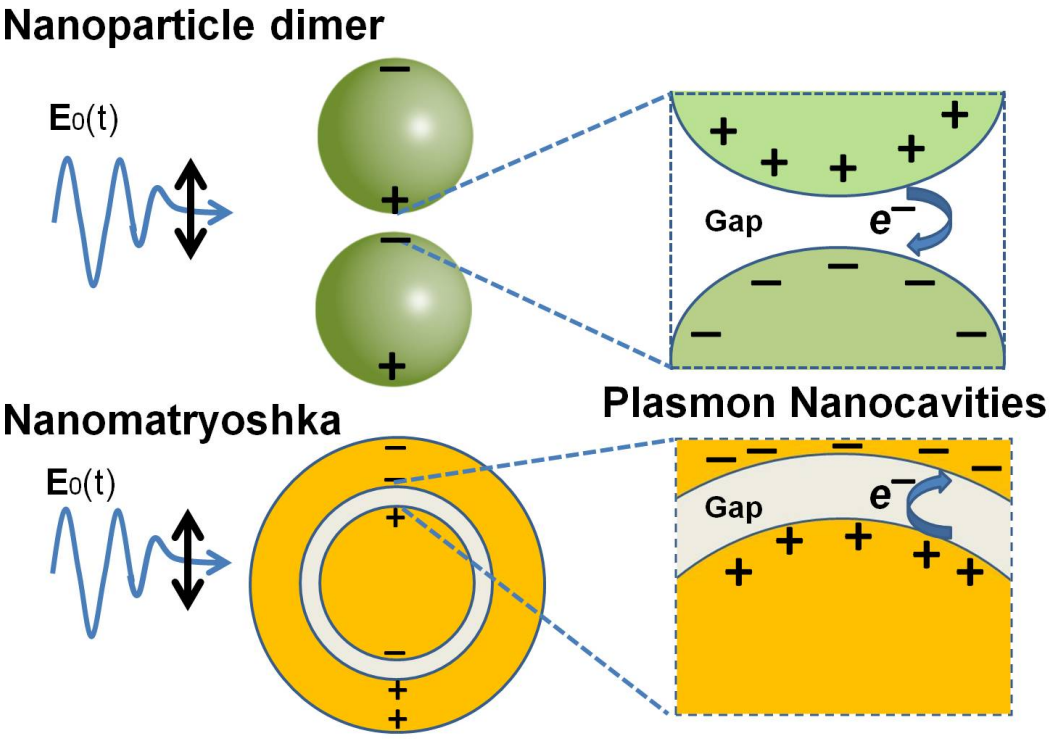

FIGURE 1.9: Nano-optics in plasmon cavities. Sketch of the interaction of linearly polarized light with a cavity made by a plasmonic nanoparticle dimer and a nanomatryoshka. The interaction between the electric charges induced at the surfaces of the nanostructures (in the gap region) increase the coupling between plasmon modes localised at individual nanoparticles and enhances the electric field in the gap. In subnanometric cavities, the interaction between plasmonic fields and conduction electrons leads to a variety of physical processes that require quantum mechanical calculations. These processes may be exploited in optoelectronic applications, as we present in the present document.

that comprise millions of electrons. As a consequence, the ongoing theoretical effort is devoted to the study of the main quantum effects in metallic nanostructures described at full atomistic *ab initio* level or using free-electron models. Essentially, the size of the nanostructure is small enough so that the full quantum calculations mainly based on TDDFT can be performed. The knowledge acquired in these studies is then used in elaboration of the (semi-classical) approaches allowing to include the quantum effects within the framework of the Maxwell equations so that the realistic structures can be addressed with (i) account for quantum effects, and (ii) using efficient numerical solvers developed in classical electrodynamics [1, 2, 38, 39, 41–43]. Such theories, dealing with quantum nature of electrons responding to the classical electromagnetic wave become a part of a more general field research, called *quantum plasmonics*, that studies the implications for plasmonics of the particle-wave duality of both: photons and electrons.

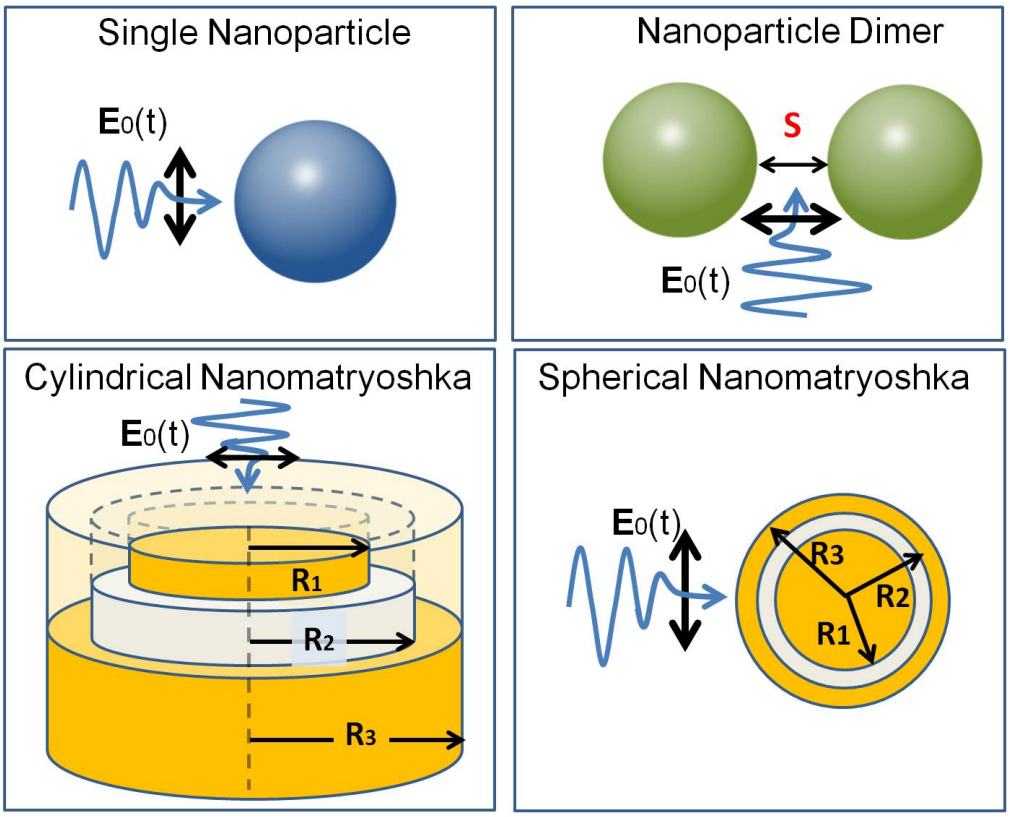

FIGURE 1.10: Different geometrical configurations of nanostructures studied in this thesis. We studied the interaction of light with individual nanoparticles, nanoparticle dimers, and core shell systems that are known as nanomatryoshkas.

1.2.1. Active Quantum Plasmonics

Up to now, we have outlined the main phenomena determining the plasmon modes of the metallic nanostructures with narrow gaps. Currently the plasmon response is tuned mainly during the nanostructure manufacturing by means of designing and engineering the nanoparticles material, size, shape, and the refraction index of the dielectric surrounding [29]. However, it would be highly desirable to dispose fast, adaptive and reversible procedures to control the plasmon response. Recent experimental developments suggest several possibilities for such *active* control, for example by using flexible substrates [44, 45], liquid crystal environments [46, 47], electrically induced heating [48, 49], optical modulation using arrays of quantum dots [50], or excitation of free carriers [51, 52]. This last option is the only one that provides access to electronic time scales (ps), however, it requires relatively high power lasers. In this context, flexibility and simplicity of the electrical modulation of the optical response with applied

bias as achieved in 2D materials, such as graphene [53] appears extremely attractive.

Two-dimensional materials allow electrical control of their plasmon response in the terahertz to infra-red frequency range via electron injection with applied bias. This is possible thanks to the overall low concentration of free charge carriers in these materials. Metal nanoparticles have high density of conduction electrons that allow a plasmon resonances in the optical range. But precisely because of this high density of conduction electrons the control strategies based on the electron/hole injection are not efficient in this case. However, as we will show in this thesis, quantum effects in narrow plasmonic gaps offer a new possibility of the active control of plasmon response. In a joint effort with theoretical groups from France[2], Spain[3], and United States[4], a concept that involves electrical control by an applied bias of the plasmon resonances of the canonical metal-insulator-metal plasmonic structure characterized by a very narrow junction is proposed. When the electron tunneling through the junction is possible, a DC bias applied across the junction allows modifying the tunneling barrier and thus the conductivity of the junction. The latter in turn affects the plasmon modes of the system. In Fig. 1.11 we show a sketch of the proposal, which will be explained in Chapter 5 Recently, Savage *et. al.* [54] have demonstrated how the quantum tunneling through the narrow gap between plasmonic nanoparticles (in a dimer geometry) strongly modifies the response of the system to the external light. In Ref. [54] the conductivity of the junction has been varied by changing its width. In analogy with scanning tunneling microscopy, we propose to reach the sought change of the conductvity via an applied DC bias. This is precisely the *active* control mechanism that we will explore and promote in a practical way in this thesis.

1.3. Summary

The present thesis is focused on the study of how the quantum effects change the plasmon properties of sub-nanometric systems. In particular, we address the systems characterised by the narrow gaps between metal nanostructures where the optical response is strongly affected by, and can be controlled with electron tunneling effects. Using

[2]Andrei. G. Borisov and Dana-Codruta Marinica. Institut des Sciences Moléculaires d'Orsay, Université Paris Sud, Paris-France

[3]Javier Aizpurua and Andrei K. Kazansky, Nanophotonics Group. Materials Physics Center and Donostia International Physics Center. Donostia-San Sebastian-Spain

[4]Peter Nordlander. Rice University, Houston-USA

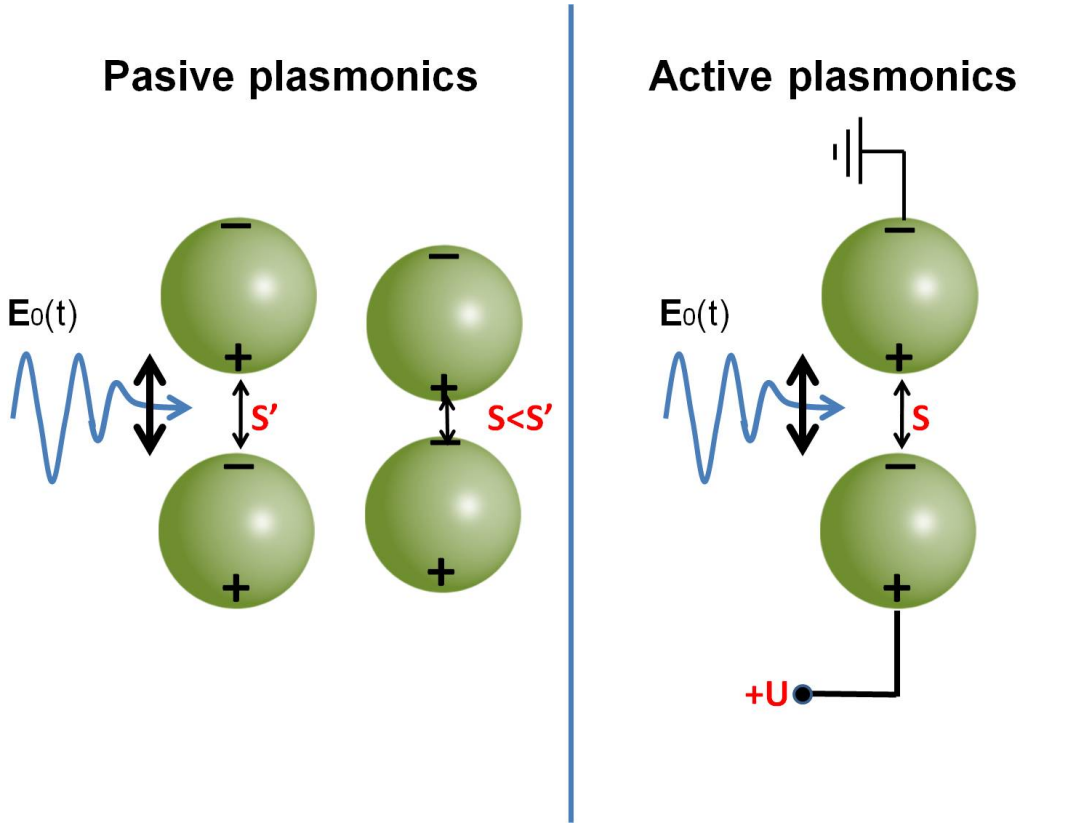

FIGURE 1.11: Schematics of the mechanism underlying the proposed bias-control strategy for active plasmonics.

several approaches, from classical electrodynamics and analytical quantum mechanics towards more sophisticate models like quantum corrected model, and full quantum TDDFT, allows us to cover different topics of current interest in the field. Our research is outlined in this thesis manuscript which is organised as following:

- Starting with the present chapter (Chapter 1) we have shown some generalities, state of the art and the main topics in the field of (quantum) plasmonics.
- In second chapter (Chapter 2), we present the study of the quantum size effects in the optical response of individual metallic nanoparticles of spherical geometry, and using different types of confinement potential. Firstly, we present the improvement of the classical models used up to now. We use electronic states in the confinement potential to derive the dielectric function and apply this dielectric function to study optical response of the corresponding metal nanoparticle. Thus, the limits of the different regimes can be defined. In particular, we show that particle sizes smaller

than 10 nm are of special interest due to their natural quantum features that make them an interesting subject to understand the limit of pure classical phenomena.

- In the third (Chapter 3) and fourth (Chapter 4) chapters, we extend different previous studies on spherical nanoparticles (or clusters) and cylindrical nanowire dimers, where the tunneling current occurs in extremely localized gap regions. We perform the quantum mechanical time dependent density functional theory calculations of the plasmonic response of cylindrical core-shell nanoparticles (nanomatryoshkas). We show that the full quantum results can be recovered in the classical calculations using the Quantum Corrected Model (QCM). Additionally, using the QCM we retrieve the quantum results for the absorption cross section in spherical nanomatryoshkas as obtained earlier [3]. Thus, our results establish the applicability of the QCM for a wide range of geometries that hold tunneling gaps[4]. We present the Quantum Corrected Model (QCM) as an alternative for describing the electron tunneling in very small gaps in hybrid nanosystems like the so called metallic nanomatryoshkas (NM).

- In Chapter 5, we propose a mechanism for fast and active control of the optical response of metallic nanostructures based on exploiting the quantum regime in subnanometric plasmonic gaps. The sough active control is reached by applying an external DC bias across a narrow gap in core shell nanostructures (cylindrical nanomatryoshkas). We demonstrate the feasibility of the concept of active control using the TDDFT calculations of the optical response of this kind of structures in presence of an applied DC bias. We show that the optical response of a metallic cavity can indeed be electrically controlled thanks to the bias induced modification of the tunneling barrier separating metallic surfaces across the gap.

- Finally, in Chapter 6, we use a TDDFT to perform a full quantum calculation of the optical response, and electron loss for charged spherical clusters. We have obtained that, because the system stays neutral in the bulk, and the extra-charge is localized at the surface of the cluster, the dipolar plasmon mode displays only small frequency shift linked with change of the electron spill-out from the nanoparticle boundaries. In the case of the negatively charged clusters, even small (relative to the total number of electrons in the system) negative charge raises Fermi level of the cluster above the vacuum level and renders the system unstable. The extra charge of the cluster decays with characteristic time constants that can be fully understood using an analytical study based on the WKB method, similar to the studies of the alpha-decay. Our results on charged clusters allow critical reinterpretation of the

experimental data obtained with electrochemistry, where the shift of the plasmon resonances have been attributed to the charging effects. Based on our results, we tentatively propose that the change of the dielectric environment in immediate vicinity of the cluster is the origin of the shift of the plasmon resonance.

- We will close the thesis with some general conclusions and summary of the main original results in Chapter 7.

Chapter 2

Confinement potential effects on the Localized Surface Plasmon Resonance of metallic small nanoparticles

In this chapter, we analyze the importance of a description of the electronic transitions in small nanoparticles through the optical response to small changes of size in systems whose dimensions are in the subnanometric scale. We present the calculations of the optical response of that kind of systems by using the exact eigen-energies and wave functions for nanospheres with diameters smaller than 10 nm, to obtain the dielectric function under different conditions of confinement. The main aim is to use the so obtained dielectric function to calculate the absorption spectra of one electron confined in a sphere in two cases: i) an infinite spherical confinement and ii) a finite spherical confinement, in which, the value of the wells depth is calculated after adjusting the number of atoms that composed each sphere, so that the energies and dipole matrix elements give a more accurate information of the optical response. Moreover, we extend the calculation of this dielectric function for obtaining the optical constants needed to find the plasmon frequency, through a numerical finite element method (FEM) solving the Maxwell's equations, in order to obtain the enhancement of the near electric field. We show an interesting behavior for particles sizes less than 10 nm, finding that the variation induced in the eigen-energies, through slight size changes in the particle, provides significant variations in the optical response of these nanoparticles. This effect, can be

observed in the optical absorption spectra and in the localized surface plasmon energies as confirmed in recent observation of plasmonic phenomena at the subnanometer to atomic scale [55].

2.1. Introduction

The localized surface plasmons (LSP) in nanoparticles are subject of analysis because they enable strong optical absorption and scattering in subwavelength structures. These properties depend on the nanoparticles material, size, shape, and the refraction index of the surrounding material [29]. Each one of these parameters is worth of being studied in order to understand the optical behavior at the nano-scale. Most of the calculations assume the Mie model [11] because it shows good agreement with experiments in nanoparticles up to 10nm size using optical constants of Johnson and Christy [30]. For smaller particles, this model achieves poor agreement, and in particular, when dealing with particles in the size-range of $1 - 10$nm, the surface becomes more and more important compared to the bulk response and thus influences heavily the collective modes localized at the surface region. On the other hand, the quantum effects should be significant due to the electrons could be able to spill out of the particle under finite confinement, and new interesting effects appear for these systems that are in the subnanometric sizes. Plasmon oscillations and electron spill out could balance tuning the optical response of the particles, as proposed recently Monreal *et al*, [56] where they examine electron spill out effects, which can induce red or blue shifts of the surface plasmon energy, that can be comparable to or even stronger than the quantum size. However, their model remains classical in spite of introducing a semiconductor like gap at the Fermi level. However, for subnanometric sizes a quantum description needs to be considered. Following this idea, we use as a starting point the question of quantization, showing an exact calculation of the dielectric function, compared with other approaches and with accurate experiments, in order to examine the optical properties of systems in the limit of subnanometric size scale. In fact, we focus this chapter on the quantum description of optical response of ultra-small spherical nanoparticles, whose diameters are less than 10 nm. We describe the dielectric function of these systems starting from the assumption that one electron confined in the nanoparticle only can have discretized energies and we make carefully calculations of the allowed electron energies and the corresponding wave-functions for infinite and finite confinement cases as function of the particle size (diameter). In both situations we use the analytical complete eigen-functions to

obtain the dielectric function, which give us confidence in the description of the optical response. We test our results of the dielectric function through optical absorption and enhancement field factor, which allow us to compare with recent experimental results [55]. Starting from an infinite spherical confinement with asymptotic values for energies and wave functions (Model A) and exact calculation of both energies and wave functions (Model B), we examine the effect of the exact values on the dielectric function for ultra-small particles. These results are also compared with finite spherical wells confinement, whose depth is obtained from the number of atoms in each particle (Model C).

In his chapter, we describe the optical absorption of one particle confined in an spherical well, where we can compare our results with experiments, and discuss the differences in absorption coming only from quantum confinement, when the electrons have to stay within the particle, and when they have a probability of being outside depending on the particle size. We also show a reproducible behavior of the plasmon energy depending on confinement, and discuss our main results comparing them with experiments and theoretical models based on the spill out effect.

2.2. The dielectric function

When the size of a nanoparticle becomes smaller than 10 nm, the continuous electronic band of a nanoparticle breaks up into observable discrete states. Such effects have been observed in experiments with metallic nano-particles, [26, 55] showing a notably difference between the results obtained in the $10 - 100$ nm regime and the 'quantum regime' (particles below 10 nm of radius).

As a first approximation, to describe the optical response of an electron gas in a metal nanoparticle, Genzel and Martin [26] showed a simplified quantum model where the free electron gas is confined in an infinite cubic potential well (see Appendix. A), where the dielectric function of a single metal nanoparticle, under the influence of an electromagnetic wave with frequency ω and z-polarization, is given by

$$\varepsilon(\omega) = \varepsilon_\infty + \frac{\omega_p^2}{N} \sum_{i,f} \frac{s_{if}(F_i - F_f)}{\omega_{if}^2 - \omega^2 - i\omega\gamma_{if}}, \tag{2.1}$$

with the terms ε_∞, s_{if}, ω_{if} and γ_{if} are respectively, the interband contribution of core electrons, the oscillator strength, the frequencies and the damping for the dipole transition from an initial state i to another final state f; and F_i and F_f are the values of the Fermi-Dirac distribution function for the initial and final states. The oscillator strength s_{if} corresponds to the dipolar form in the z-direction in terms of the initial $|i\rangle$ and final $|f\rangle$ states

$$s_{if} = \frac{2m^*\omega_{if}}{\hbar}|\langle f|z|i\rangle|^2. \tag{2.2}$$

where the parameter $m^* = m_e/N$ is given in terms of the mass of electron m_e and the total number of confined atoms N. Using different types of confinements, we calculate the eigen functions and energies, within the A, B and C models described before [57].

2.2.1. Free electron gas in a spherical infinite well confinement: Exact solution

We consider an infinite spherical potential well to solve the Schrödinger equation for one electron, with the appropriate boundary conditions finding a set of wave functions of the form [58]

$$\psi(r,\theta,\phi) = \frac{1}{|j_{l+1}(\alpha_{nl})|}\sqrt{\frac{2}{R^3}}j_l\left(\frac{\alpha_{nl}}{R}r\right)Y_l^m(\theta,\phi), \tag{2.3}$$

where j_l represents the spherical Bessel functions, Y_l^m the standard spherical harmonics, α_{nl} is the n-th zero of j_l and R the radius of a spherical particle. The eigen-energies $E_{n,l}$ of this problem in a quantized form associated to the l-th spherical Bessel function are given by

$$E_{n,l} = \frac{\hbar^2\alpha_{ln}^2}{2m^*R^2}. \tag{2.4}$$

The oscillator strenght in Eq.(2.2) can be calculated, taking $z = r\cos\theta$ in the expression

$$\begin{aligned}|\langle f|z|i\rangle| = &\int_0^{2\pi}\int_0^{\pi}\int_0^{R} drd\theta d\phi r^3\sin\theta\cos\theta \\ &\times \Psi^*_{n_f,l_f,m_f}(r,\theta,\phi)\Psi_{n_i,l_i,m_i}(r,\theta,\phi),\end{aligned} \tag{2.5}$$

where the angular integral has the form

$$\begin{aligned} I_{ang} =& \sqrt{\frac{(l_i + m_i + 1)(l_i - m_i + 1)}{(2l_i + 1)(2l_i + 3)}}\delta_{\Delta l,+1} \\ &+ \sqrt{\frac{(l_i + m_i)(l_i - m_i)}{(2l_i + 1)(2l_i - 1)}}\delta_{\Delta l,-1} \end{aligned} \tag{2.6}$$

and, the radial term,

$$I_{rad} = \frac{1}{|j_{l_f+1}(\alpha_{n_f l_f})|}\frac{1}{|j_{l_i+1}(\alpha_{n_i l_i})|}\left(\frac{2}{R^3}\right) \times \int_0^R dr j_{l_f}\left(\frac{\alpha_{n_f l_f}}{R}r\right) r^3 j_{l_i}\left(\frac{\alpha_{n_i l_i}}{R}r\right). \tag{2.7}$$

Then, the integral to calculate is simply

$$|\langle f|z|i\rangle| = I_{ang} \times I_{rad} \tag{2.8}$$

which is different from zero only for values $\Delta l = l_f - l_i = \pm 1$. This description corresponds to our labeled Model B.

2.2.2. Free electron gas in a spherical infinite well confinement: Approximate solution

One way to obtain a simplified solution of the problem is to use the approximation [55]

$$\begin{aligned} E_{n,l} &= \frac{\hbar^2\pi^2}{8MR^2}(2n + l + 2)^2 \\ &= \frac{\hbar^2}{2MR^2}\left[\pi\left(n + \frac{l}{2} + 1\right)\right]^2, \end{aligned} \tag{2.9}$$

for the eigen-energies, and the asymptotic form for the wavefunctions [58],

$$j_l(x) \approx \frac{1}{x}\cos\left[x - \frac{\pi}{2}(l + 1)\right], \tag{2.10}$$

valid only for $x \gg l^2/2 + l$.

Eq.(2.4) (Model B) and Eq.(2.9) (Model A) give us different values for nanoparticles, for example with $R = 1$nm. We can observe a good agreement only for $l = 0$, and a significant overestimation for $l > 0$. Besides this, in Fig. 2.1 we show $j_l(kr) = j_l(\alpha_{ln}r/R)$ and its asymptotic approximation given by Eq.(2.10) versus r/R and $n = 1$. As we can

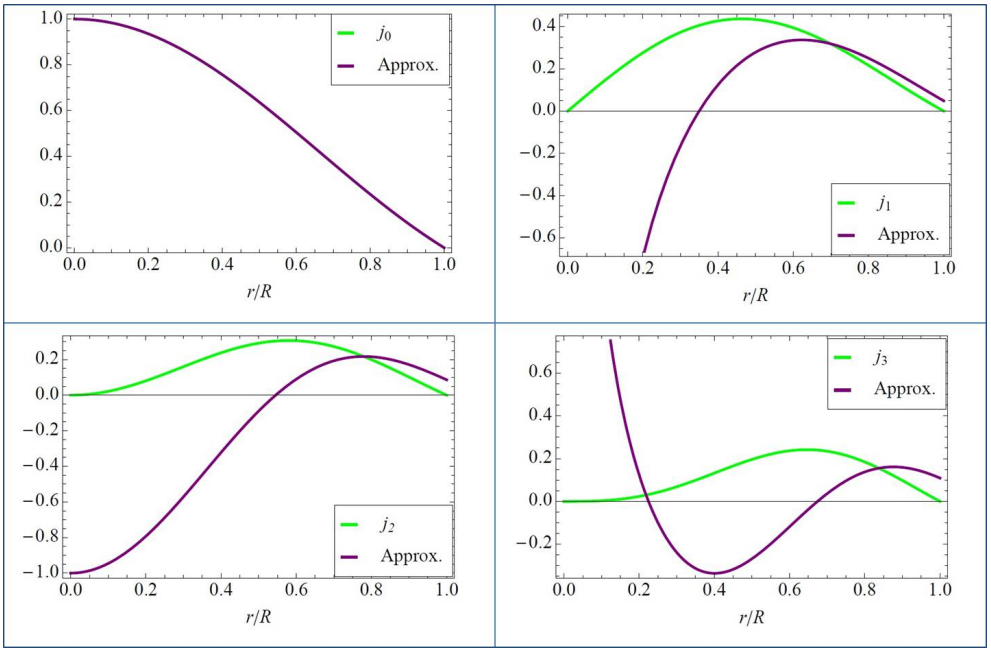

FIGURE 2.1: Comparison between j_l and its asymptotic approximation (2.10) versus r/R for different l's and $n = 1$.

see, the approximate and the exact Bessel functions are identical for $l = 0$, but they differ remarkably for the $l = 1, 2$, and 3 quantum numbers. Therefore, we conclude that the use of exact wave functions (Model A) are absolutely needed to give an accurate description of the optical response in these systems.

2.2.3. Quantum finite confinement

Going a step further, we consider a finite spherical confinement, which is related with the number of atoms contained in a spherical nanoparticle. We fit a relation derived of *ab initio* calculations made by He *et. al.* [59], by taking the number of particles as function of its radius R. Based on this relation, then we calculate the last occupied electronic state following the Pauli exclusion principle. This energy value is defined as the Fermi level and varies with the nanoparticle radius. To establish the depth of the well, we consider the work function $W(R)$ for small metallic nanoparticles following Ref. [60], which is defined as the energy required to remove one electron from the nanoparticle, which is given by

$$W(R) = 4.37 + \frac{5.4}{R(\mathring{A})}, \tag{2.11}$$

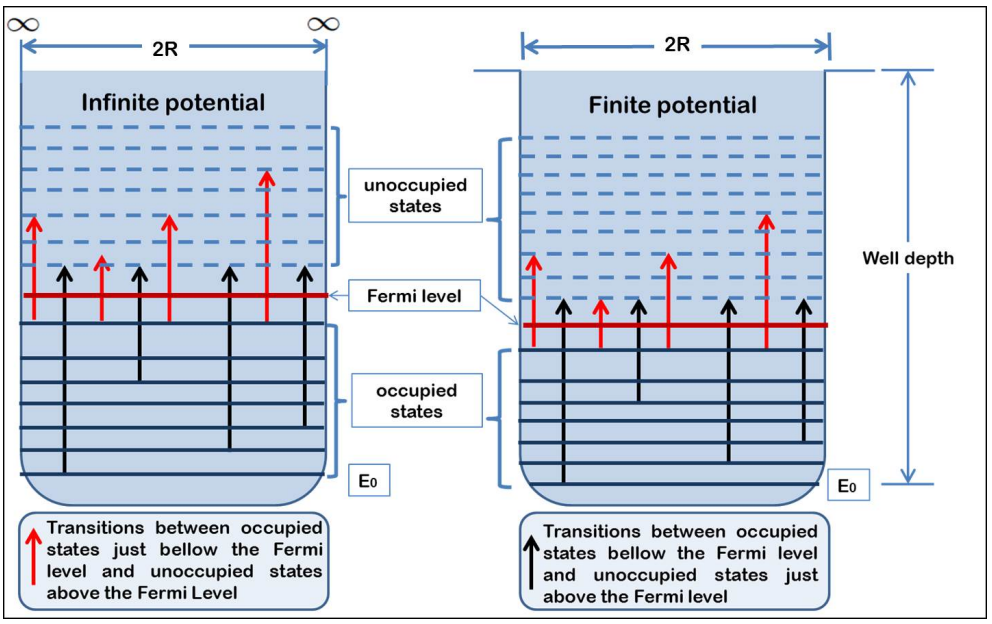

FIGURE 2.2: Schematic diagram illustrating quantum infinite potential and quantum finite potential, to evaluate the dipolar contributions in the dielectric function. Here we show some transitions when the energy levels are quantized.

where the 4.37 value is the average work function for bulk Ag (in eV) and $5.4 = \frac{3}{8}e^2$ is a parameter that accounts for the difference in the work function for a conducting plane and a sphere [60]. Considering this value, we define the depth well D_W as the sum of the Fermi energy level E_F and $W(R)$ for each nanoparticle radius, which reads as

$$D_W(R) = -(E_F(R) + W(R)). \tag{2.12}$$

Using this result, we solve the Schrödinger equation numerically, calculating the eigenvalues for each nanoparticle. In order to obtain the corresponding dielectric function, we need the oscillator strength for the allowed transitions using the wave functions of infinite confinement, which are needed to obtain the dielectric function as can be seen in Eq.(2.2). We choose transitions between occupied states just below the Fermi level and unoccupied states above the Fermi level, and transitions between the unoccupied state just above the Fermi level and occupied states below the Fermi level, in a wide range $(0 - 6\text{eV})$, following the selection rule $\Delta l = \pm 1$, which gives us a complete information of the allowed electronic transitions in our systems. We show in Fig. 2.2, a schematic diagram that illustrates this assumptions for quantum B and C Models.

2.2.4. Confinement effects on the optical response

Now, we calculate the dielectric function based on Eq.(2.1), and present the imaginary part of the dielectric function for several nanoparticle sizes in Fig. 2.3. The continuous black lines, corresponding to the Model A, show besides the main peak, several possible transition with smaller intensity, while the dashed lines, Model B, reduces significantly the number of transitions in the region of interest, as an effect of the oscillator strenght. On the other hand, the energy position of the main peaks is always blue-shifted with respect of Model B for each radius.

With the aim of examining the trend of the peaks of energy in the imaginary part of the dielectric function as a function of radius and to compare the results of the three models we present Fig. 2.4. While model A predicts a monotone blue-shift as the particle radius decreases, whose value reaches almost 2 eV for $R = 1$ nm, Models B and C, show a maximal blue-shift about 1 eV. However, the shifts between consecutive diameters oscillate.

2.3. Absorption spectra

In this section, we compare the absorption peaks following the three approaches described above. To calculate the absorption spectra, we use the expression

$$\sigma_{ext}(\omega) = \frac{9 f \omega \varepsilon_m^{3/2} \mathrm{Im}[\varepsilon(\omega)]}{c(\mathrm{Re}[\varepsilon(\omega)] + 2\varepsilon_m)^2 + (\mathrm{Im}[\varepsilon(\omega)])^2}, \tag{2.13}$$

where f is a fraction of volume of the sphere in the media, ε_m corresponds to the dielectric constant of the surrounding media and c the light speed [61]. For particles of radius 5nm there is no appreciable difference between the three calculations (see Fig. 2.5), showing all of them a peak at 3.3 eV, while for smaller particles we obtain both red and blue shifts that are coming from the confinement type. Looking from the top to the bottom of Fig. 2.5, the particle radius decreases and Model A (at the left), show a rather smooth blue-shift while Models B and C (center and right), present red and blue shifts alterning as function of the nanoparticle radius. We observe oscillations of the maximal absorption for nanoparticles smaller than 10nm ($R = 5$nm). The high dispersion of the experimental EELS measurements [55] in this region also shows big

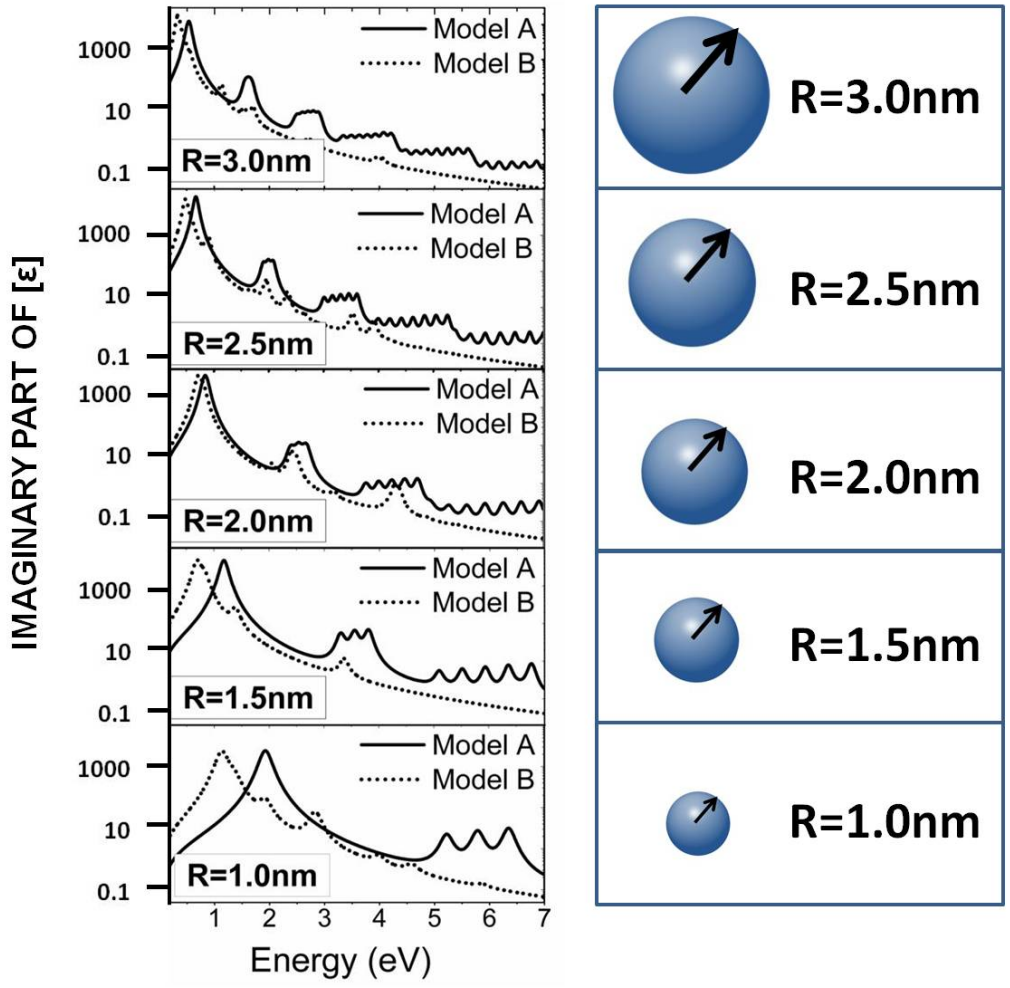

FIGURE 2.3: Imaginary part of the dielectric function for a silver nanoparticle as function of radius based on Model A (continuous lines) and Model B (dashed lines).

oscillations for particles smaller than 10 nm of diameter. Our predictions are located below the region of experimental error, which can be corrected through the ε_∞ parameter. The three approximations are in good agreement to each other and to the experiment, showing changes of red and blue shifts at the same particle sizes.

With the aim of testing our three models of dielectric function related to the localized surface plasmon resonance in silver ultra small nanoparticles, we present in the next section the enhancement field factor.

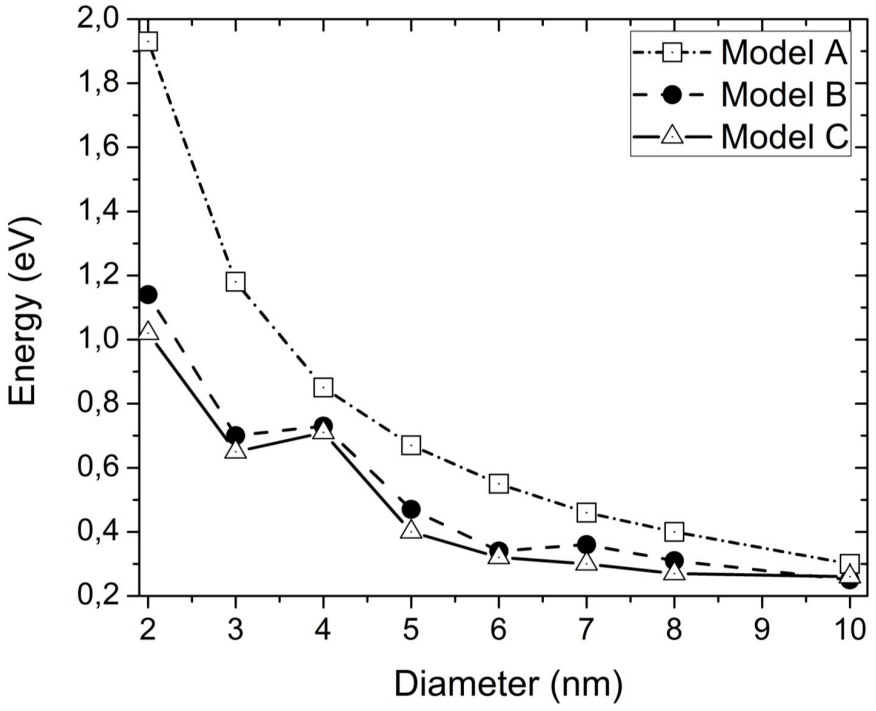

FIGURE 2.4: Main peak in the imaginary part of the dielectric function for each model used. Squares represent the Model A, black points Model B and triangles Model C.

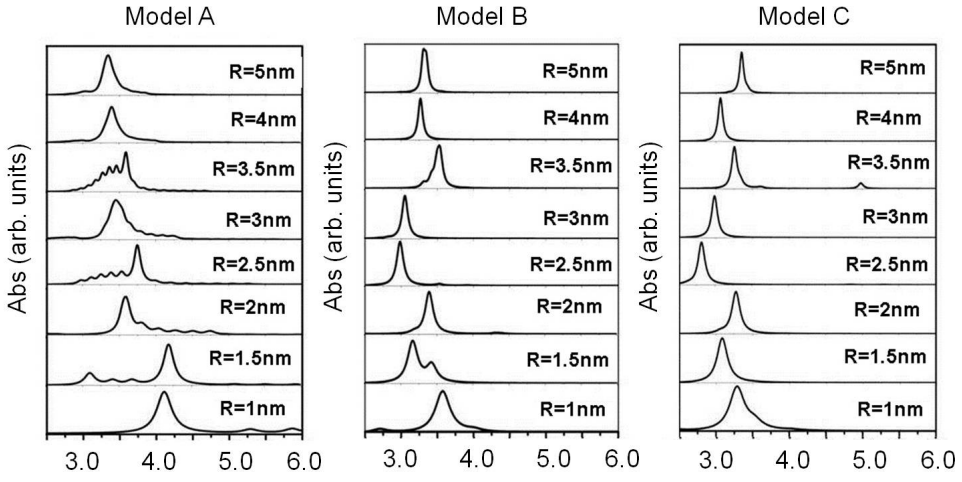

FIGURE 2.5: Absorption spectra for several particle radius, using Model A (left), Model B (center) and Model C (right).

2.4. Enhancement of the near field

We calculate expressions for the dielectric function depending on the incident electromagnetic wave frequency $\varepsilon_r(\omega)$ as input parameters, which are calculated for each particle size and confinement potential, by solving the vector Maxwell equations numerically, by means of a standard finite elements method (FEM) using the COMSOL Multiphysics package [34], as we defined in the last chapter.

The obtained resonances give the frequencies of the surface local plasmon, and we observe that we obtain values located at the same energies as the absorption peaks, which follow the same behavior as discussed earlier.

If we look at the field factor for each particle radius in Fig. 2.6 from bottom to top, we observe a red and blue shifts for all particle radius as a whole, depending on the used model. Comparing Model A with Model B, the change is due to the dipole matrix elements (oscillator strength), while the differences between Model A and Model C are due to transition energies. Both effects show lower plasmon energies than the approximate Model A, maintaining the same parameters in the three models. However, they show an increase in the enhancement field factor of about 4 times (compared with model A). The behavior of the plasmon frequency within each model, shows oscillations, that means red and blue shifts alternating. Finally we present in Fig. 2.7, another feature that is interesting comparing with EELS experiment, which is the energy width of the region where the oscillations are detected. In Model A, the width achieves more than 1.5 eV, while for model B and C is only of 1 eV. On the other side, the experimental measurements show values ranging from 0.8 eV, with maximal error bars for 5 and 3 nm diameters, where small changes in the particle size can give strong shifts, which depend on the sensitivity to the well depth. It means to the eigen energies and corresponding oscillator strengths. As the particle decreases from 10 nm, the enhancement field factor decreases, indicating a weaker near field because the number of electrons that can resonate are getting less and less. However, for this range of nanoparticles the ratio surface/volume increases considerably, giving rise to strong dependence on the energy differences and oscillator strength between them.

In Fig. 2.7, we show the localized surface plasmon resonance frequency, obtained by the maximum of enhancement field factor for each particle size and we observe that for particles smaller than 10 nm our three models provide the same behavior, showing

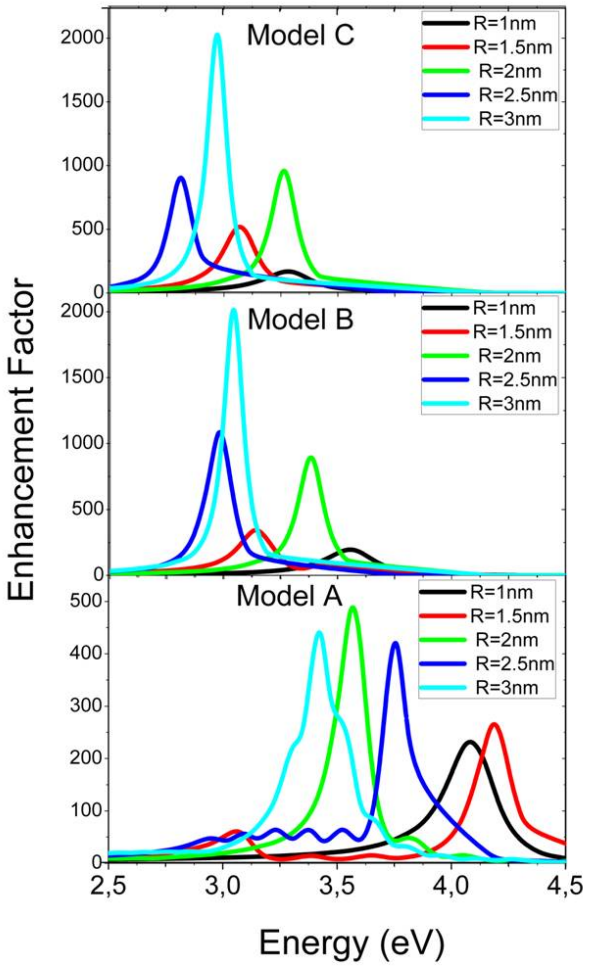

FIGURE 2.6: Enhancement Field Factor for a silver nanoparticle as function of radius based on quantum approximate model (model A) [55], infinite exact model (model B) and finite confinement (model C) of one electron in a spherical particle.

alternating red and blue shifts as the particles size decreases. In the inset we present the experimental EELS reported for the plasmon frequency in the same sizes range obtained by Scholl *et al* [55], in which we can observe error bars of about one half electron volts in the energy plasmon spectrum for nanoparticles about 5nm and 3nm. However, our three models give plasmon energy values for several particle sizes, showing in this spectrum, a kind of oscillations, as the particle size decreases. The confinement effect is only important for very small nanoparticles, as expected. In a recent paper [56] is discussed the screening effect on the surface plasmon compared to quantum size effect for ultra small nanoparticles, less than 10nm. They show a monotone behavior, as

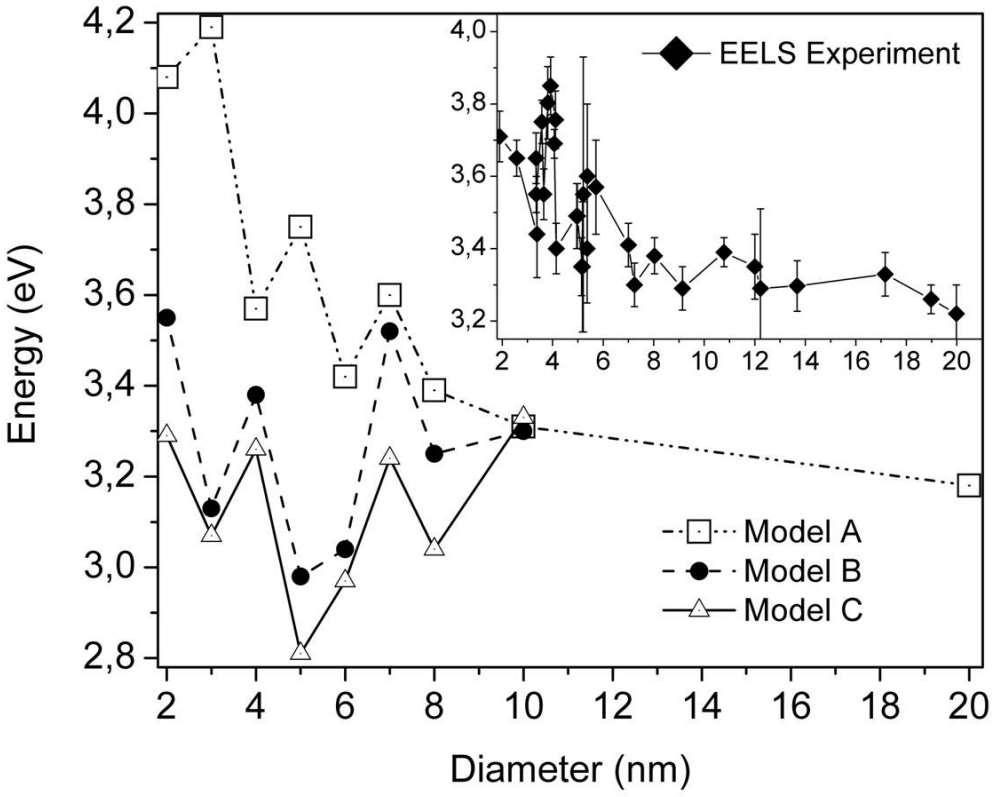

FIGURE 2.7: Plasmon energy as a function of the spherical nanoparticles diameter. Squares, dots and triangles show the results when Model A, B and C are used. The inset present the experimental EELS results obtained by Scholl *et. al.* in [55].

result of a balance between size effect (blue shift) and spill out effect (red shift) based on pure classical calculation. However, when comparing with EELS experiments, the big error bars in the region of interest screen detailed optical response in this region. Our claim is that there are clear oscillations within the error bars that can be understood as confinements effects due to the energy differences and their allowed transitions, which are extremely sensitive to small changes in the nanoparticle size. Therefore, we conclude that a more sophisticate model that can account for a collective description of the optical response is needed.

2.5. Summary

We have examined using different analytical and numerical approaches, the optical response of ultra-small metal nanoparticles, varying their sizes from 10 to 2 nm diameter in steps of 0.5 nm in order to observe the sensitivity to small particle size changes. The reason for the oscillations in optical response is that very small changes in the energy spectrum induce significant and uncontrollable changes in the allowed electronic transitions. We also compare two types of confinement, using two sets of wave functions and we conclude that red shifts in the plasmon energies are mainly due to the oscillator strengths, while the eigen-energies for finite and infinite confinement taken from the exact zeros of the Bessel functions (Models B and C) do not strongly influence the plasmon energies. But both of them differ considerably from the calculation based on asymptotic values (Model A).

We have shown that exact quantum calculations, based on optical response of one electron confined in a sphere, open a way to understand the optical properties of ultra-small nanoparticles, which is to be completed with many body effects that surely appear in this region of particle sizes that limits the nanoscale and enters in the atomic scale. In the region beyond nanometric scale, we could find optical response of nanoparticles strongly dependent on the change of the size due the changes of the allowed electronic transitions, within the discrete energy levels that should be taken into account carefully to understand the plasmon behavior in ultra small nanoparticles that are composed of hundreds of atoms.

Other effects that should be taken into account to understand the optical response of ultra-small nanoparticles, undoubtedly require microscopic accurate description such *ab initio* calculations, in order to improve the models presented in this chapter. We need a more empirical effective theory that allows us to describe the phenomena observed experimentally paying the price of a less detailed description of the effects of local response in the optical quantum subnanometric regime. The models presented in this chapter, can be consider as a first appoximative models, and have not the formalism of self-consistent calculations, typically used in this kind of systems. Nevertheless, is a good starting point to understand more suitable and complex calculations, as we will show in the next chapter.

Chapter 3

Quantum effects in the optical response of core-shell nanostructures

Quantum effects as nonlocal screening and electron tunneling can strongly affect the plasmonic response of hybrid nanostructures. Number of recent works demonstrated on the example of several systems that these quantum mechanical effects can be taken into account semi-quantitatively within a classical framework of Maxwell equations. Thus, the so-called Quantum Corrected Model (QCM) allows to account for electron tunneling in narrow gaps between metal nanoparticles. In this chapter, we extend previous studies on spherical clusters and cylindrical nanowire dimers where tunneling and hybridization effects occur in extremely localized regions near the touching point. We perform quantum mechanical TDDFT calculations of the plasmon response of the axially symmetric cylindrical core-shell nanoparticles known as nanomatryoshkas (NM), where the tunneling region extends over entire core-shell gap. We benefit from this axially symmetric situation to address relatively large (for full quantum simulations) systems of up to 12 nm in diameter. We have obtained that for core-shell separations below 0.5 nm, the standard classical calculations fail to describe the plasmonic response of the cylindrical nanomatryoshkas, while the QCM can reproduce quantum results. Using the QCM, we also retrieve the quantum results for the optical response of spherical nanomatryoshkas (as previously calculated by V. Kulkarni *et. al.* [3]). The comparison between the model and the full quantum calculations establishes the applicability of the QCM for a wider

range of geometries that hold tunneling gaps.[1]

3.1. Introduction

Modern nanotechnology allows for fabrication of metallic nanoparticles and nanoparticle assemblies of different geometry, structure, and composition [8, 54, 55, 62–71]. This extraordinary opportunity, in turn, opens a possibility to engineer the plasmonic modes of these artificial nanostructures and thus the way they interact with light [72–76]. In this context much of the interest has been devoted to the nanostructures that form narrow plasmonic gaps between their constituent metallic surfaces [73]. The strong interaction of the plasmon-induced charge densities across the gap results in the manifold enhancement of the confined fields and in the hybridization of the plasmonic modes of the individual nanoparticles [77–79]. The field enhancement and the geometrical tunability provided by plasmon resonances find many practical applications including sensing [8, 80–83], plasmon rulers [62, 73, 84–88], and non linear optics [23, 68, 69, 89–94], among others. So far, the classical electrodynamics framework based on the local description of the metal dielectric function appeared adequate to describe optical properties of strongly coupled plasmonic nanoparticles separated by narrow gaps. However, recent experimental [54, 55, 64, 69, 95–97] and theoretical [1, 38, 39, 41–43, 54, 98–100] studies have demonstrated the importance of quantum mechanical effects when particle-to-particle separations are reduced below the nanometer. In this case, the non-local screening and electron tunneling across the gap can reduce (and even quench) the field enhancement, and alter the optical response of the system. Because of the tunneling a conductive contact between the nanoparticles can be established prior to the direct geometrical overlap. As a consequence, the extinction resonances arising from the hybridization of the plasmonic modes of the individual nanoparticles disappear from the spectrum. At the same time, a set of charge transfer plasmon modes emerge as a consequence of the electron flow between the nanoparticles [98, 101–105]

[1] The graphs and the text including in this chapter, correspond mainly to the work published in Optics Express referenced in [4]. BEM codes were devoloped by Javier Aizpurua from the Theory of Nanophotonics Group in the Materials Physics Center CFM, Donostia-San Sebastian, Spain and Donostia International Physics Center (DIPC). We adapted them for our purposes with the valuable help of Rubén Esteban from the same affiliation. TDDFT codes used in this chapter, where shared by Andrei Borisov from Institut des Sciences Molèculaires d'Orsay (ISMO), Universite Paris Sud, France, and adapted for our purposes.

The use of nonlocal dielectric functions [41, 106–109] captures part of the quantum behavior of such systems introducing a smooth variation of the screening electron density profile at the interface between materials in contrast to the classical theories which admit infinitely sharp spatial variations of the screening charge densities. This solves the problem of the divergence of the electric fields in the junction and of the energy shifts of the plasmon resonances with decreasing junction width, as obtained in local classical theories [110]. The latest developments of the non-local hydrodynamic descriptions allow to introduce the realistic electron density profile at the surface so that full quantum results can be retrieved for individual nanoparticles [111] albeit at the price of growing the numerical complexity. However, to account for tunneling across narrow interparticle junctions requires a special treatment that goes beyond classical local or non-local hydrodynamic approaches. Quantum tunneling thus imposes a real challenge to any theoretical description. Indeed, the simplest strategy to tackle the effect of tunneling would consist in performing full quantum calculations of the plasmonic response, as recently reported, within an atomistic ab initio or free electron description of the metal nanoparticles [1, 38, 39, 41–43, 54, 99]. However, because of numerical constraints, quantum calculations can only address systems which are much smaller than those of practical interest in plasmonics. A possible solution to this constraint consists in model local dielectric functions that account for the quantum tunneling, in a way similar to the derivation of the macroscopic permittivity of a system from the microscopic quantum polarizabilities of the constituent atoms or molecules [112]. This is achieved with the Quantum Corrected Model (QCM) [1, 2] that treats the junction between the nanoparticles as an effective medium mimicking quantum tunneling within the classical local dielectric theory. So far, the QCM has been shown to correctly reproduce the full quantum results in plasmonic dimer structures with a localized contact region supporting the tunneling current [42, 54, 95, 97, 100].

In this chapter, we study a system formed by a cylindrical metallic core and a cylindrical metallic shell, separated by an extended tunneling contact region between the core and shell metal surfaces, so-called cylindrical nanomatryoshka (CNM). These kind of hybrid nanostructures present a large tunability in their plasmonic response which considerably explains their practical and fundamental interest. Provided current fabrication techniques NM-like structures of small size can be produced with very narrow gaps between the core and the shell [70, 71]. Several studies addressed optical properties of NMs within classical electromagnetic theory framework which appeared sufficient in explaining the available experimental data [113–121]. It is only recently that the full

quantum results have been reported for the spherical NM [3] showing the importance of tunneling between the core and the shell.

In this chapter we address yet unexplored case of quantum regime in cylindrical NM, with particular emphasis at the comparison between the full quantum TDDFT results and results obtained using the QCM within the framework of classical Maxwell equations. We study in great detail the evolution of the plasmonic resonances of the cylindrical NM upon variation of the size of the gap between the core and the shell. We focus on the quantum effects in this system where the standard classical calculations fail to describe the plasmonic response of the cylindrical NM for core-shell separations below 0.5 nm, while the QCM can reproduce well the quantum results. We also demonstrate that the QCM reproduces the quantum results obtained previously for the spherical NM [3], offering an efficient way to address tunneling effects in core-shell nanoparticles. Thus, together with previous studies of plasmonic dimer structures with tunneling regions localized around the contact point, our results for NMs demonstrate the validity of the QCM for broad range of geometries of the tunneling regions. Indeed, in the present case the tunneling current flows transversally through the entire core-shell gap.

3.2. System and computational aspects

In Fig. 3.1, we show the sketch of the cylindrical and spherical core-shell nanostructures. We have taken the name for these structures from the real russian dolls (or matryoshkas), which gives an accurate name for this hybrid nanostructures. To define the systems, we firstly start with the case of cylindrical NM where the infinite metallic cylindrical core and metallic cylindrical shell are coaxial with the geometry set by the radius of the core R_1, the internal radius of the shell R_2, and the external radius of the shell, R_3. Following this notation, we will adopt the set (R_1, R_2, R_3) to characterize the NM structure [3]. We consider the case where an incident light is polarized perpendicular to the symmetry axis of the system. To focus the discussion on the role of the tunneling effect in the plasmonic response, and to facilitate the comparison with earlier published work on spherical nanomatryoshkas, without loss of generality the region between the core and the shell is chosen to be vacuum. The results presented here, are obtained for a fixed $R_2 = 90\ a_0$ (48 Å), and $R_3 = 115\ a_0$ (61 Å), while the radius of the core R_1 is varied (here a_0=0.53 Å stands for the Bohr radius). The range of considered R_1 corresponds to the progressive reduction of the width of the vacuum gap between the core and the shell $S = R_2 - R_1$ from 20 Å down to the touching geometry ($S = 0$). This

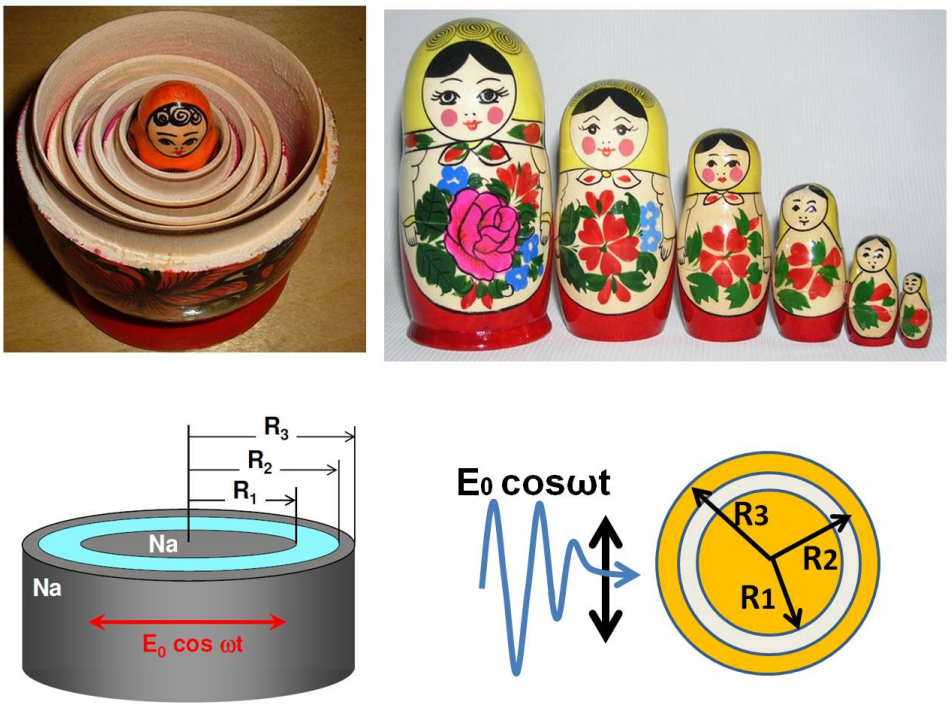

FIGURE 3.1: Sketch of the geometry of the nanomatrioshka. Upper: Real nanomatryoshkas or russian dolls, which inspires the names of the structures that we study in this thesis. Lower: cylindrical (left) and spherical (right) nanomatryoshkas. In the case of the cylindrical NM, the coaxial cylindrical core and cylindrical shell are infinite along the symmetry axis of the system. The core has the radius R_1; the internal radius of the shell is R_2 and the external radius of the shell is R_3 for both systems. The core and the shell are separated by a vacuum gap. The incident field with amplitude E_0, and angular frequency ω is polarized perpendicular to the symmetry axis of the NM.

allows an analysis of the emergence of the tunneling across the gap, and of its role in the evolution of the NM plasmonic modes into those of the uniform cylindrical nanowire.

In our quantum calculations the metallic core and the shell are described within the cylindrical jellium model (JM) (see for example ref. [42, 100]). The valence electrons are bound by the uniform positive background charge representing the ionic cores. This background charge density is given by $n_0 = \left(4\pi\, r_s^3/3\right)^{-1}$, where r_s is the Wigner-Seitz radius. R_1 defines the position of the boundary of the positive background charge, the jellium edge, of the core. R_2, and R_3 define inner and outer jellium edges of the shell respectively. Despite its simplicity, the JM correctly captures the collective plasmonic behavior of the conduction electrons, and it has demonstrated a good predictive power in the description of quantum effects in nanoparticle dimers, as follows from the comparison with experiments [54, 55], and with advanced full atomistic ab initio calculations

[122]. We use the Wigner-Seitz radius r_s equal to 4 a_0 (2.12 Å) corresponding to Na metal. In this case the JM performs particularly well in the description of the optical pulse interaction with nanosized objects [123–126]. For noble metals, such as silver and gold, the contribution of the localized d-electrons to the screening [127, 128] imposes introduction of the polarizable background [38] which would complicate the interpretation of the results, and obscure the comparison with the classical Drude and QCM model calculations. The qualitative conclusions in this chapter are robust and independent of the particular choice of the density parameter.

3.2.1. Optical response in the TDDFT framework

The quantum calculations of the absorption cross-section are based on the Kohn-Sham (KS) scheme of the density functional theory (DFT) [129]. We use the adiabatic local density approximation with the exchange-correlation functional of Gunnarson and Lundqvist [130]. A detailed description of the numerical technique can be found in Ref. [39] and in Ref. [100]. First, the ground state electron density and Kohn-Sham orbitals are obtained in standard static DFT calculations. Using the axial symmetry allows to address the system with up to 290 electrons per 1 Å length. The structures are characterized by an overall work function of 2.9 eV, where the exact value depends on the nanostructure geometry defined by the (R_1, R_2, R_3) set. At a second stage, the ω-dependent absorption cross-section per unit length, $\sigma_{abs}(\omega)$, is calculated from the electron density dynamics induced by an impulsive perturbation, within the time-dependent density functional theory (TDDFT) approach as

$$\sigma_{abs}(\omega) = \frac{4\pi\omega}{c}\mathrm{Im}[\alpha(\omega)], \tag{3.1}$$

where $\alpha(\omega)$ is the dipolar polarizability per unit length of the system. Because of the small transverse size of the system, retardation effects are neglected for the present choice of the polarization of the incident electromagnetic wave. Consistent with TDDFT, the classical electromagnetic calculations of the absorption cross section have been performed within the quasi-static approximation [120, 121] using the local classical and the QCM approaches.

The dielectric function of the metal is described within the Drude model (see Eq.(1.2)) described in Chapter 1. We use the parameters $\omega_p = 5.68$ eV and $\gamma = 0.218$ eV as

obtained from the fit of the classical results to the TDDFT calculations for the isolated cylindrical nanowire with radius $R = 115\ a_0$ (6.1 nm). Such nanowire corresponds to the system with a fully closed gap between the core and the shell. The value of $\omega_p = 5.68$ eV is lower than the nominal plasma frequency for the bulk Na given by $\sqrt{4\pi n_0/m} = 5.89$ eV, with m_e, the electron mass, reflecting the red shift of the dipolar plasmon from the classical Mie value given, for the metallic cylinder, by $\sqrt{2\pi n_0/m}$. This red shift is the finite size effect resulting from the spill out of electron density outside metal boundaries, as has been throughly studied in the context of surface physics [123, 128, 131–135].

3.2.2. The quantum corrected model in core-shell nanomatryoshkas

In order to analytically explain the tunneling effects in the extended small gaps of the cylindrical nanomatryoshkas, we use the well known Quantun Corrected Model (QCM), widely explained in [1, 2] for plasmonic dimers. Effects like quantum tunelling are not explained using classical electrodynamics and fails to describe the coupling across subnanometer gaps, where quantum effects become important. QCM approach, models the junction between adjacent nanoparticles by means of a local dielectric response that includes electron tunnelling and tunnelling resistivity at the gap and describes the electron tunneling between the core and the shell by filling the core-shell gap with an effective dielectric medium described by a Drude model that depends on the gap separation distance S, similar to that in Eq. 1.2, as:

$$\varepsilon_{\text{eff}}(S,\omega) = \varepsilon_\infty - \frac{\omega_p^2}{\omega(\omega + i\gamma_{\text{eff}}(S))}. \tag{3.2}$$

The effective damping γ_{eff} models the transition from a resistive to a conductive nature of the junction as a function of the gap separation S. Consistently with the dependence of the electron tunneling probability on the size of the gap, γ_{eff} is given by

$$\gamma_{\text{eff}} = \gamma_0\ \exp\left[S/\Delta\right]. \tag{3.3}$$

For the tunneling contact between Na metal surfaces we use $\varepsilon_\infty = 1$ in Eq. 3.2 and in Eq.(3.3) we use $\gamma_0 = 0.218$ eV and $\Delta = 0.75$ Å, which are taken from references [1, 2], and are related to quantum-mechanical calculations of the electron transmission probability through the potential barrier separating the two metals. For sufficiently large

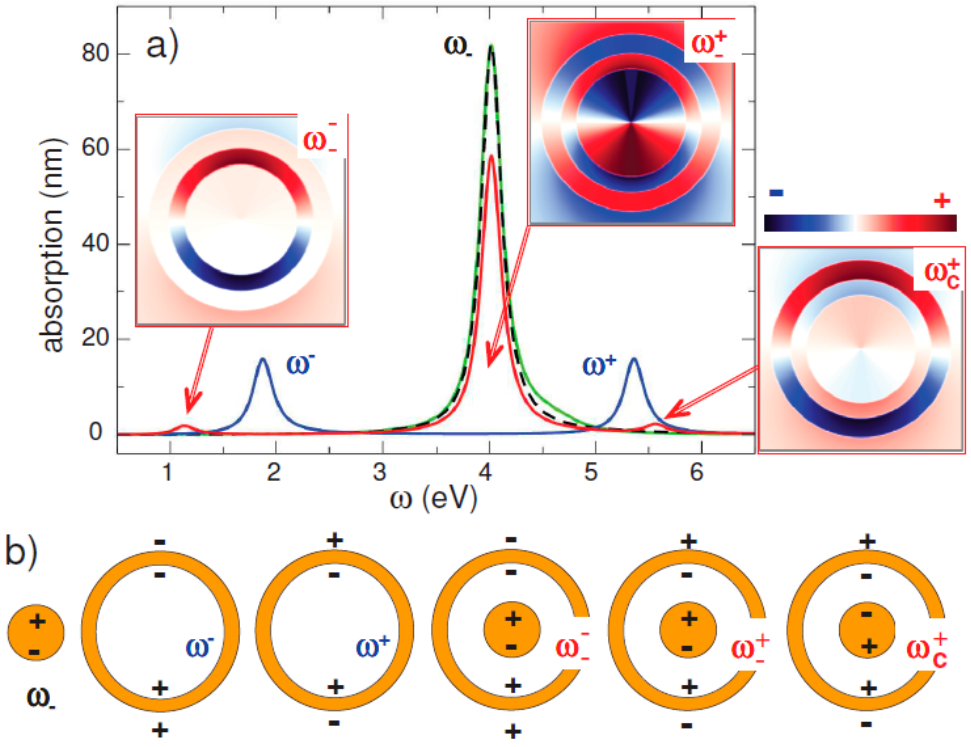

FIGURE 3.2: (a) Absorption cross section per unit length. The green line shows the TDDFT result for an individual nanowire with radius $R = 61$ Å. The rest of the results are obtained using classical electromagnetic theory within a nonretarded approximation. Black dashed line: individual nanowire with radius $R = 61$ Å. Blue line: cylindrical shell with internal radius $R_2 = 47.7$ Å, and external radius $R_3 = 61$ Å. Red line: cylindrical $(37.1, 47.7, 61)$ Å nanomatrioshka. Insets show the direction of the radial electric fields associated to the ω_-^-, ω_-^+, and ω_c^+ modes of the core-shell structure. The arrows indicate the corresponding absorption resonances. (b) Schematic charge distribution for the different plasmonic modes identified in a).

separation distances $S \to \infty$, the effective damping $\gamma_{\text{eff}} \to \infty$, and the QCM becomes exactly equivalent to the local classical approach. In this situation, no tunneling is possible and the vacuum gap limit is retrieved with $\varepsilon_{\text{eff}}(S, \omega) = 1$. For $S \to 0$ the junction becomes metallic with permittivity equivalent to that of the bulk metal so that the NM responds as a homogeneous metallic cylinder.

3.3. Plasmon modes of a nanomatryoshka

To characterize the optical response of the cylindrical NM with particular emphasis on the assignment of the plasmonic modes, we base our discussion on the classical quasistatic results which provide a good reference for the full quantum calculations of the NM with

large gap, and thus no tunneling. The nonretarded approximation is well justified in case provided small relevant dimensions of the structure. The classical results have also the advantage of featuring well defined many-body plasmonic modes, not affected by the interaction with single-particle electron-hole pair excitations which are typical for the quantum TDDFT calculations in systems of small size like this [41, 125, 126]. In Fig. 3.2(a) we show the absorption cross section per unit length of an individual cylindrical nanowire with external radius $R = 61$ Å (black dashed line). This would correspond to the limiting case of a NM with zero width of the gap $S = 0$. Our calculations also show the results for a cylindrical shell with internal radius $R_2 = 47.7$ Å, and external radius $R_3 = 61$ Å, (blue line), and finally, the case of a cylindrical NM with the same shell as in the previous case, and a core of radius $R_1 = 37$ Å, i.e. a cylindrical $(37, 47.7, 61)$ Å NM (red line). In units of Bohr radius the dimensions of the system are (70,90,115) a_0[2]. For the individual nanowire, the TDDFT data (green line) is presented along with classical results (dashed black line) allowing to access the quality of the classical Drude modeling of the optical response in this case.

The absorption cross section of the individual cylindrical nanowire representative for the core of the NM is dominated by the single plasmon resonance at surface plasmon frequency $\omega_- = \omega_p/\sqrt{2}$, where ω_p is the bulk plasma frequency in the Drude model of dielectric function given by Eq. 1.2. As already pointed out, because of the nonlocal screening and the small radius of the nanowire, in our TDDFT calculations $\omega_- = 4.02$ eV is red shifted with respect to the corresponding surface plasmon frequency of the Na metal, 4.16 eV [41, 123, 128, 131–135]. The distribution of the plasmon-induced charges of this mode is schematically shown in Fig. 3.2(b). The optical absorption of the cylindrical shell is characterized by a low frequency bonding resonance ω^-, and a high frequency antibonding resonance ω^+ [125, 126] with plasmon charges separated, respectively, over the entire shell or across each shell boundary as shown in Fig. 4.1(b). In the NM, the ω_- dipole mode of the core nanowire hybridizes with ω^- and ω^+ dipole modes of the nanoshell giving rise to the ω_-^-, ω_-^+, and ω_c^+ resonances. The lowest energy bonding hybridized resonance ω_-^- at 1.1 eV is formed by the bonding shell mode ω^- with an admixture of the core ω_- resonance. The most prominent ω_-^+ absorption resonance of the nanomatrioshka at 4 eV is formed primarily by the symmetric coupling of the ω^- core mode with the ω^+ shell resonance. Finally, the antisymmetric coupling of the ω_- core mode with the ω^+ shell resonance forms the anti-bonding resonance of the NM,

[2] In practice, atomic units are the natural choice for quantum studies, and while in most of the cases we give dimensions in Å for convenience of a broad audience, our TDDFT calculations use atomic units.

ω_c^+ (here we use the terminology from Ref. [3] by Kulkarni *et al.*). As follows from Fig. 3.2(b), the charge distribution of the ω_-^+ mode corresponds to the parallel core and shell dipoles so that this mode strongly interacts with incident electromagnetic wave. The ω_-^- and ω_c^+ modes are characterized by the antiparallel core and shell dipoles, therefore the corresponding absorption resonances are weak in this case.

3.3.1. Near field distribution

In the insets of Fig. 3.2(a) we present the near-field distribution of the plasmon resonances of the NM. Owing to the opposite sign of the plasmon induced charges at the surface of the core and inner surfaces of the shell, the lowest energy bonding hybridized mode ω_-^- is characterized by a strong field enhancement inside the core-shell gap. On the other hand, because the core and shell dipoles are antiparallel, the fields are weak outside the structure. Similar to ω_-^- , and because of the induced charge configuration, for the ω_-^+ resonance the fields in the gap are also strongly enhanced. For this mode the core and shell dipoles are aligned. This leads to strong induced fields outside the structure consistent with the most intense peak in the absorption cross section at ω_-^+. The core character of the ω_-^+ resonance clearly appears in the structure of the corresponding induced fields showing a bright core region. The ω_c^+ mode is characterized by the opposite sign of the core and shell dipoles and by the same sign of plasmon-induced charges across the gap. The fields are thus low in the gap, core and vacuum regions. Strong plasmon-induced fields are only calculated inside the shell consistent with the shell character of this plasmon mode. It should be noted that the character of the modes and their near field distribution is analogous to that of a spherical NM [3, 114–119]. The resonance energies are however different because of the different dimensionality of the problem. Indeed, for a Drude metal, the quasistatic cylindrical core plasmon is at $\omega_- = \omega_p/\sqrt{2}$, while the spherical core plasmon is at $\omega_- = \omega_p/\sqrt{3}$.

From a qualitative analysis of the induced charge distributions and near fields of the modes, it is possible to presume that quantum effects might be relevant when the gap separation between the core and the shell in the NM decreases. This situation can occur by means of an increase of the core radius R_1. Analogous to the spherical NM case [3], because of electron tunneling between the core and the shell, the gap becomes conductive for small S (narrow gaps). In the touching limit ($S \to 0$), a situation analogue to that

of the continuous metallic cylinder can be reached even prior to the direct geometrical contact at $R_1 = R_2$. In such a situation, the modes ω_-^- and ω_c^+ would disappear and the mode ω_-^+ would evolve into that of the metallic cylinder with a radius given by the external radius of the shell $R_3 = 61$ Å. Since ω_-^- and ω_-^+ resonances are characterized by a distribution of opposite charges across the gap, the effect of tunneling in these modes can be expected to be stronger than for the ω_c^+ resonance. The above discussion is fully confirmed by the quantum TDDFT results presented in the next section.

3.4. Quantum tunneling across the gap.

In the left column of Fig. 3.3, we show the waterfall plots of the absorption cross section of the NM per unit length. The results are shown as function of the frequency ω of the incident radiation polarized perpendicular to the symmetry axis of the system. The calculations were performed over a wide frequency range, and for various gap sizes, from well separated core and shell, down to the situation of conductive contact at $S = 0$. Different panels of the figure correspond to the results obtained within classical calculations using the Drude model of the metal permittivity (top), within the full quantum TDDFT (center), and with the quantum corrected model (QCM) (bottom). The system geometry is defined by $(R_1, 47.7, 61)$ Å, where the core radius has been varied within the limits 26.5 Å$\leq R_1 \leq$ 47.7 Å, allowing to vary the size of the vacuum gap according to $S = 47.7 - R_1$ Å.

The gross features of the results are similar for the classical, quantum and QCM descriptions of the system. These results resemble those reported in the literature for similar core-shell systems [3, 113–119]. With an increasing value of the core radius, R_1 (decreasing S), the interaction between the induced charges across the gap increases, and the pair of hybridized plasmons with shell character display red-shift (ω_-^-) and a blue-shift (ω_c^+), respectively. Because of the mutual compensation between the core and the shell dipoles for these modes [see Fig. 3.2(b)] their spectral features progressively loose their intensity in the absorption spectrum. For $R_1 \to R_2$, the ω_-^- and ω_c^+ resonances can be hardly distinguished in the spectrum. The differences between the quantum and the classical calculations, particularly for the ω_-^- mode, cannot be observed in the left-hand side spectra of Fig. 3.3, since their scale is set by the main peak in the absorption cross section (the core resonance ω_-^+). For a vanishing gap, this prominent resonance evolves into the dipolar resonance of the full metallic cylinder with radius $R_3 = 61$ Å. It is

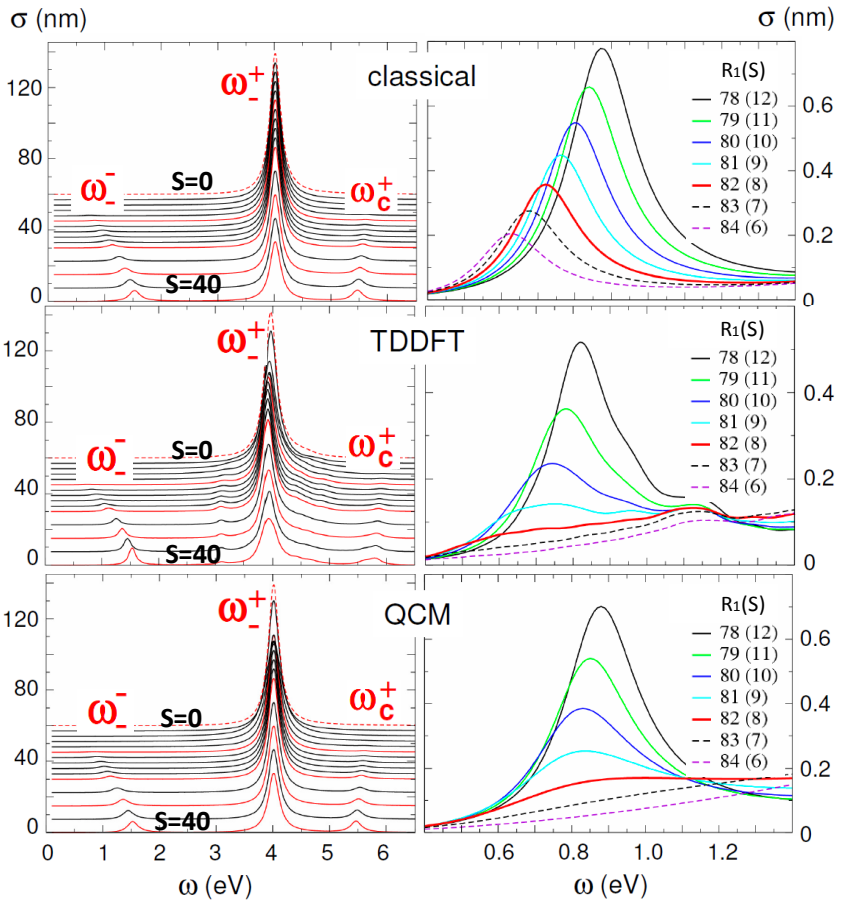

FIGURE 3.3: Waterfall plot of the absorption cross section per unit length, σ of a cylindrical nanomatryoshka defined by $(R_1, 47.7, 61)$ Å or equivalently $(R_1/0.53, 90, 115)\ a_0$, where the Bohr radius $a_0 = 0.53\ \mathring{A}$ calculated using classical electromagnetic theory (top), TDDFT (center) and the Quantum Corrected Model (QCM) (bottom). Results are given as a function of the frequency ω of the incident radiation for different core radii R_1. The left panels show the results within a large ω range showing all the resonances described in Fig. 3.2. R_1 varies within the limits $50a_0 \leq R_1 \leq 90a_0$ $(26.5\mathring{A} \leq R_1 \leq 47.7\mathring{A})$ corresponding to gap separation distances, S, from 40 a_0 down to 0, as indicated from bottom to up on the spectra. For clarity, a vertical shift is introduced to each absorption spectrum. The curves are displayed in red every 10 $a_0 \approx 5.3\mathring{A}$ of R_1-change. The lowest absorption spectrum in each panel corresponds to $R_1 = 50\ a_0$ $(S = 40\ a_0)$, and the red dashed curve on top $(S = 0)$ is used as a reference for the absorption spectrum of the solid metallic cylinder with external radius $R = 115\ a_0$ $(61\mathring{A}\ )$. The plasmonic modes responsible for the peaks in the absorption cross-section are labeled in each panel. ω_-^- stands for the bonding hybridized resonance, ω_-^+ for the hybridized resonance with a dominantly core character, and ω_c^+ for the antibonding resonance of the nanomatryoshka. The right panels focus on results for core radii R_1 in the range of 78 $a_0 \leq R_1 \leq 84\ a_0$ $(41.3\mathring{A} \leq R_1 \leq 44.5\mathring{A})$ at the frequency range of the ω_-^- plasmon of $0.4\ eV \leq \omega \leq 1.4\ eV$. These are the conditions where the effect of the resonant electron transfer on the bonding hybridized plasmon ω_-^- is most prominent. The correspondence between the color used for the absorption spectra and the value of the core radius R_1 is given at the upper right panel of the figure. R_1 is indicated in units of a_0 and the number in parenthesis gives the corresponding size of the gap, S, between the core surface and the inner surface of the outer shell.

worth mentioning that for small R_1 (large S), the TDDFT results for the core ω_-^+ plasmon show a small ($\sim$ 0.2 eV) red shift because of the electron spill-out effect and the nonlocal screening [123, 128, 131–135]. Along with (slight redshift), for small R_1 the ω_-^+ resonance features an additional broadening because of the increased Landau damping. It is also possible to notice some additional structures in the TDDFT absorption cross-section due to the presence of electron-hole pair excitations [41, 125, 126]. The left-lower panel of Fig. 3.2 shows that the QCM reproduces well the details of the spectra. For example, it captures the abrupt change of the main absorption peak at small gap separation distances (spectra on the top), similarly to that present in the TDDFT calculations, whereas the classical calculations show a smoother evolution. This abrupt change at $S \approx 1$ Å is linked with the lowering of the potential barrier separating the core and the shell below the Fermi level. Under these conditions, electrons flow through the gap quasi-freely forming a continuous metallic connection.

As we discussed above, the effect of electron tunneling is expected to be the strongest for the ω_-^- resonance, since it is characterized by induced plasmon charges of opposite sign across the gap. On one hand these opposite charges induce strong field in the junction and thus (i) increase the coupling between the core and the shell plasmons; as well as (ii) increase the tunneling current. On the other hand, this tunneling current, when large enough, neutralises the charges across the gap. To reveal the role of quantum tunneling in the NM gap, in the right panels of Fig. 3.3 we zoom into the spectral range of frequencies of the ω_-^- resonance, showing the evolution of this lowest energy mode as the gap becomes smaller. We compare results obtained with Classical Drude (top), TDDFT (center), and QCM (bottom) approaches for values of core radius R_1 in the range of 78 $a_0 \leq R_1 \leq$ 84 a_0 (41.3 $\mathring{A} \leq R_1 \leq$ 44.5 $\mathring{A}$) corresponding to gap sizes in the range of 6 $a_0 \leq S \leq$ 12 a_0 (3.2 $\mathring{A} \leq S \leq$ 6.4 $\mathring{A}$). As found in previous calculations of the plasmonic dimer structures [1, 38, 39, 41, 42, 122], tunneling effects progressively appear for narrow gaps. In the classical calculations, the ω_-^- resonance is always present albeit being attenuated and red-shifted with increasing R_1 (decreasing width of the gap S). The quantum TDDFT results show a qualitatively distinct behavior. For the smallest value of the core radius $R_1 = 78\ a_0$ considered in Fig. 3.3, the ω_-^- absorption resonance calculated with TDDFT agrees well with classical result. However, the resonance is fully quenched for $R_1 = 82\ a_0$. For this very narrow gap of $S = 8\ a_0$, electron tunneling across the gap neutralizes the induced plasmonic charges of opposite sign at the facing surfaces of the core and the shell. This leads to the disappearance of this bonding hybridized plasmon. In contrast, in the classical calculations this gap mode is always present for

any $S \neq 0$.

In the lower panels of Fig. 3.3, we can observe that the TDDFT results are well reproduced by the QCM calculations, including progressive broadening and final quenching of the ω_{-}^{-} resonance for narrowing gaps due to the increasing resistive tunneling losses. Since classical electrodynamic theory does not account for tunneling, it fails to reproduce the full quenching of the gap plasmon prior to the direct geometrical contact between the core and the shell. The failure of the classical theory and success of the QCM in reproducing the TDDFT results can be clearly appreciated, for instance by comparing the spectra in red line on the three right hand side panels of Fig. 3.3. Finally, the high energy antibonding mode ω_{c}^{+} is not so affected by quantum tunneling due to the symmetric distribution of charges at both sides of the gap (see Fig. 3.2). Classical and TDDFT calculations give practically the same results in this case for all separation distances (including the narrowest ones), therefore the QCM does not bring any essential improvement for this mode.

3.4.1. The near field enhancement

In Fig. 3.4 we show the field enhancement factor FEF for the field in the middle of the gap, as obtained with the classical Drude, QCM and full quantum TDDFT approaches. The FEF is defined as $\frac{|\vec{E}|}{|\vec{E_0}|}$, where $\vec{E}$ is the electric field measured inside the gap at position $R = (R_1 + R_2)/2$ along the axis defined by the electric field vector of the incident plane wave $\vec{E_0}$. The FEF has been calculated for the incident electromagnetic wave, resonant with the energy of the hybridized ω_{-}^{-} mode and with the ω_{-}^{+}. For a size of the gap S, bellow 6 Å (core radius above 78 a_0) the quantum TDDFT results show distinct differences with respect to the classical predictions (area marked with a shaded background in Fig. 3.4). The onset of the electron tunneling between the core and the shell comes along with the disappearance of the ω_{-}^{-} resonance, and thus with a pronounced decrease of the FEF. Eventually FEF for small gap sizes where the limit of the homogeneous metallic cylinder is reached prior to direct physical contact between the core and the shell at $R_1 = R_2$. The QCM correctly reproduces the results of the quantum TDDFT, including a decrease of the field enhancement at the ω_{-}^{+} resonance for intermediate tunneling distances. Indeed, the resistive tunneling losses lead to a

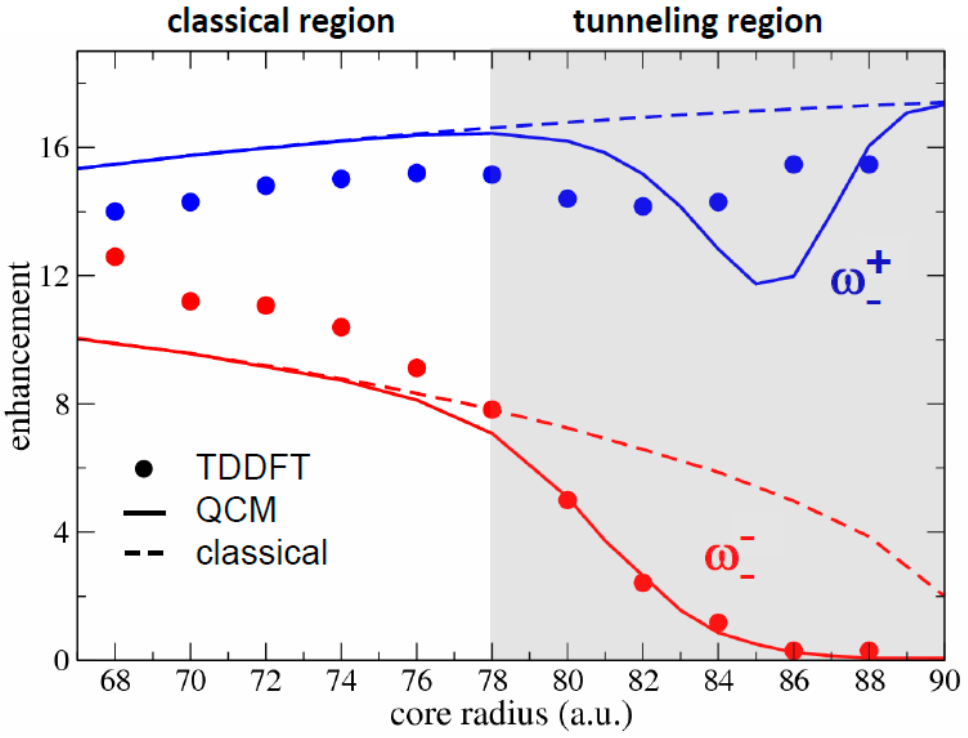

FIGURE 3.4: Field Enhancement Factor FEF calculated in the middle of the gap between the core and the shell (at $R = (R_1 + R_2)/2$) following the axis defined by the polarization of the incident field. Dots represent the TDDFT results, dashed lines represent results obtained using classical Drude calculations, and solid lines represent the QCM results. Red color is used for the data at the frequency of the lowest energy bonding hybridized resonance ω_-^-, and blue color for the data at the frequency of the main absorption peak labeled as the ω_-^+ resonance. The shaded background separates the region where tunneling occurs from the classical region.

certain broadening of the plasmon peak which results in a moderate decrease of the corresponding field enhancement. For vanishing separation, $S \to 0$, the junction becomes conductive and FEF tends to the characteristic value of a homogeneous metallic cylinder of radius R_3.

The ability of QCM to describe the quantum results has been reported in previous calculations for spherical and cylindrical dimer structures with gaps characterized by narrow contact regions which allow for the presence of tunneling current. In these systems the progressive disappearance of the bonding dipole plasmon mode and the appearance of

the charge transfer plasmon mode prior to direct contact between the nanoparticles has been addressed within the quantum TDDFT calculations. These features are correctly reproduced with the QCM, while classical theories fail to address the spectral behavior, even qualitatively. Already at finite junction sizes the particles forming the dimer are conductively connected showing the characteristic charge transfer plasmon modes [78, 101–103, 105, 136]. In our calculations we observe the same physics, with the core and the shell of the nanomatryoshka being conductively connected prior to the direct contact between their surfaces, and thus effectively forming the uniform metallic cylinder. However, differently to plasmonic dimer structures, the tunneling current in the case of a cylindrical NM flows over the whole extended gap region, a substantial dimensional difference that makes the NM an appropriate system to test quantum effects in plasmonics.

3.4.2. Plasmon modes of a spherical gold nanomatryoshka

The quantum effects described here for the cylindrical core-shell NM structure are similar to those found by Kulkarni *et al.* in their TDDFT study of the spherical gold NM [3]. Therefore, we also analyze the performance of the QCM model in this spherical case. We use the QCM to calculate the absorption cross section of a gold NM within the non-retarded quasistatic approximation. This choice is justified considering the size of the studied system (external radius below 8 nm), and it is consistent with non-retarded calculation of the potentials employed in the TDDFT study. For the sake of comparison, we use the Drude-like model for the dielectric permittivity of gold as developed in Ref. [3] based on their quantum calculations of the optical absorption:

$$\varepsilon(\omega) = \varepsilon_\infty - \frac{\omega_p^2}{\omega(\omega + i\gamma)}, \tag{3.4}$$

with $\varepsilon_\infty = 8$, $\omega_p = 9.07$ eV, and $\gamma = 0.27$ eV. Within the QCM model, the effective dielectric medium in the gap, ε_{eff} is defined by the frequency, and separation dependent dielectric constant

$$\varepsilon_{\text{eff}}(S,\omega) = \varepsilon_\infty - \frac{\omega_p^2}{\omega(\omega + i\gamma_{\text{eff}}(S))}. \tag{3.5}$$

where $\gamma_{\text{eff}}(S)$ for gold is given by Eq. 3.3 with $\Delta = 0.4$ Å [1, 2].

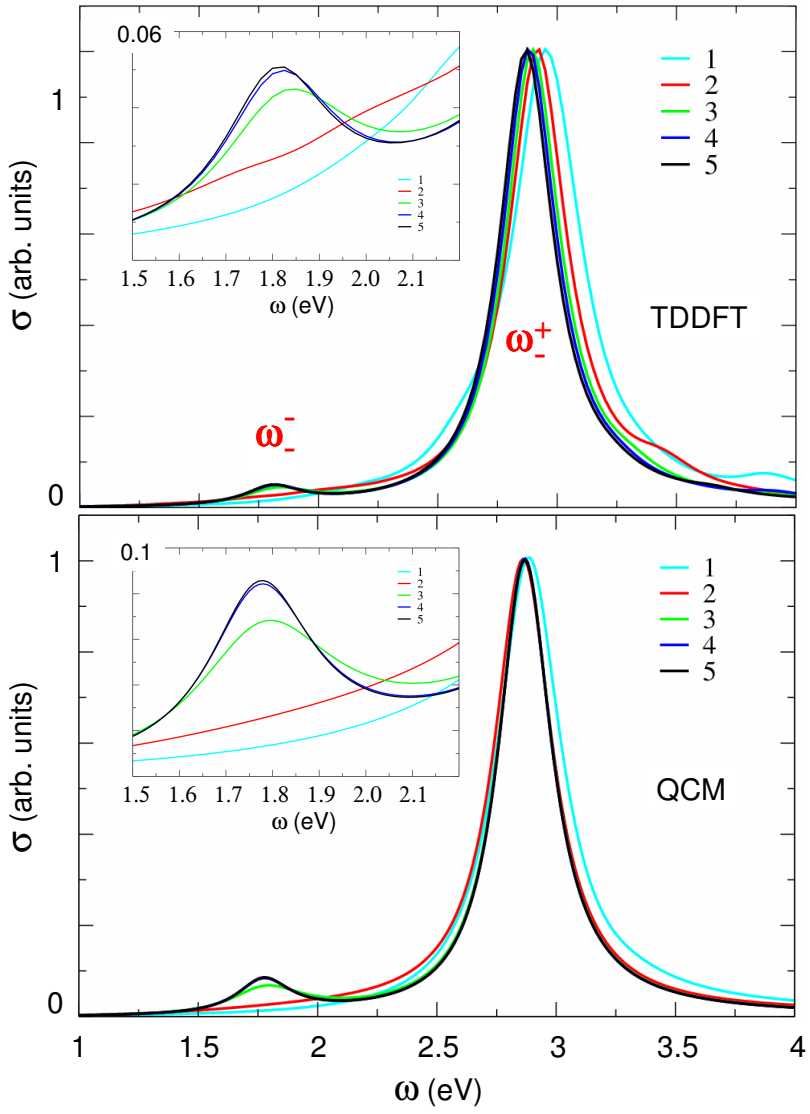

FIGURE 3.5: Absorption cross section, σ_{abs}, for a spherical gold nanomatryoshka as a function of frequency ω. The results are normalized to the absorption maximum. Different NMs are considered whose dimensions are defined by $\lambda \times (R_1 = 8.5, R_2 = 9.5, R_3 = 15.9)$ Å where the values of λ ranges from 1 to 5, as displayed in the inset. R_1 is the core radius. R_2, and R_3 stand respectively for the internal and external radius of the shell. Upper panel: quantum results from TDDFT calculations from Ref. [3] by Kulkarni *et al.* Lower panel: current results based on the QCM. The bonding hybridized resonance ω_-^-, and the main absorption peak of the core resonance ω_-^+ are indicated in the upper panel. The graphs in the insets show the respective zoom in of the low-energy bonding hybridized resonance.

Fig. 3.5 presents the frequency dependent optical absorption cross section, for five spherical NM geometries ($\lambda \times (8.5, 9.5, 15.9)$ Å). These correspond to the scaling of a basic NM structure given by (8.5,9.5,15.9) Å, with a scale parameter $\lambda = 1, 2, 3, 4, 5$. This scaling [3] is implemented to rely on the scale invariance of the plasmon resonances within the non-retarded limit of the classical electrodynamics. The absorption cross section should be identical for scalable systems with scale factor λ^3. Thus, any departure from the universal behavior can be associated with a signature of a quantum effect. The upper panel of Fig. 3.5 reproduces the quantum results of Kulkarni *et al.* and the lower panel of Fig. 3.5 shows the absorption spectra obtained within our QCM calculation. For large gap sizes (4 Å and 5 Å), tunneling across the gap is not efficient and the results show the universal behavior pointed out above. When the gap size is reduced to 3 Å, the electron tunneling through the gap increases enough to lead to a visible attenuation of the ω_-^- resonance. Finally, similar to the cylindrical NM case, when the gap size is reduced below 2 Å (4 a_0), the tunneling current across the gap becomes large so that the lowest energy bonding hybridized resonance is quenched. This change of the absorption spectra exceeds the capabilities of the classical theory to treat such extreme gaps, as pointed out in [3] by Kulkarni *et al.* However the TDDFT results are well reproduced with the QCM, confirming the good performance of the latter in description of the optical properties of a spherical geometry with an extended tunneling contact.

3.5. Summary

In conclusion, the work in this chapter, shows the applicability of the quantum corrected model to the description of the optical properties and plasmonic modes in the systems which show an extended tunneling contact region between metallic surfaces. This conclusion stems from the thorough comparison of the optical response calculated with the QCM and with full quantum TDDFT for the case of a cylindrical nanomatryoshka, where the metallic core and metallic shell are separated by a vacuum gap. We considered a metallic system made of Na because the free-electron character of the Na valence electrons allows for a jellium model description. Reasonably large-size system with well developed plasmonic modes can be addressed in this way at the fully quantum level. Moreover, in this case the material permittivity can be well described with the Drude model which eases the comparison between quantum, classical electromagnetic,

and QCM results.

We obtained that when the core-shell gap is reduced below 5 Å, the optical response is determined by the quantum tunneling of conduction electrons across the potential barrier separating the core and the shell. Our results agree with earlier calculations on plasmonic dimer structures. Specifically, when the width of the core-shell gap is reduced, the lowest energy bonding hybridized plasmon mode disappears and the field enhancement in the middle of the junction is quenched. The limit of the homogeneous metallic cylinder is reached prior to the direct contact between the core and the shell. The classical local Drude description fails to reproduce the observed effects since it does not account for tunneling. In contrast, the QCM results are found to be in good agreement with the full quantum calculations. For large gap sizes, electron tunneling is negligible and there is an overall agreement between TDDFT, classical Drude, and QCM calculations. Therefore, as a whole, the QCM performs very well over the entire range of core-shell gap sizes S studied here. We note however that the TDDFT results show some features that are not reproduced with classical models: the size dependent frequency shifts of the plasmonic modes due to the nonlocal screening, the size dependent broadening because of the Landau damping and, finally, additional spectral features because of electron-hole pair excitations.

We have also performed the QCM calculations of the optical response of the spherical gold NM, where results of earlier quantum calculations were available [3]. The spectral trends are similar to those found for the cylindrical sodium NM. The absorption spectra obtained with QCM and with quantum calculations are in very good agreement. This validates the applicability of the QCM to general systems characterized by extended tunneling contact regions between metallic surfaces. Together with the earlier studies in plasmonic dimers that showed narrow tunneling contacts, our results extend the range of applicability of the QCM. Elucidating the main physics in tunneling plasmonic gaps shows enormous potential with important consequences in the accurate description of far- and near-fields in extreme morphologies, as well as in the control of non-linear effects associated to ultranarrow gaps such as in rectification.

The results obtained in this chapter, prepare and validate theoretical tools to be used in description of the optical properties of more complex realistic systems systems with extended plasmonic gaps. These kind of structures comprise hundreds of thousands of

electrons, so that the TDDFT calculations are out of reach. The QCM appears then as a theory of choice allowing to calculate optical response with account for quantum effects. Comparison of the experimental and theoretical data for the spherical NMs with functionalized gaps is the subject of the next Chapter.

Chapter 4

Tunneling effects in spherical gold nanomatryoshkas

As we have shown in the previous chapter, quantum effects like electron tunneling across the small cavities in plasmonic systems play an important role in defining the optical response of structures with subnanometer gaps. These effects can strongly alter both their near- and far-field optical responses. In this chapter, we use the QCM to investigate plasmon coupling in spherical gold nanomatryoshkas with different core-shell separations and the core-shell gap functionalised with different dielectric materials such as SiO_2 and self-organized molecular layer(s) SAMs. We compare theoretical results with experimental data in order to elucidate the main physical mechanisms operating in these systems. Here, we show that when the width of the gap decreases below 1 nm, the near- and far-field properties can no longer be described by classical approaches but require the inclusion of quantum mechanical effects such as electron transport through the self-assembled monolayer junction. This is consistent with surface enhanced raman scattering (SERS) measurements indicating strong electron-transport across the molecular junction. The model presented here, provides an estimate for the AC conductances of molecules in the junction.[1]

[1]This chapter, including graphs and text contents, corresponds mainly to the work published in Nanoletters [5]. In this work, the experimental results were performed by L. Lin, M. Xiong, Z. Liu, S. Wang, H. Xu, H. Gu, and J. Ye from School of Biomedical Engineering and Med-X Research Institute, Shanghai Jiao Tong University.

4.1. Introduction

As we have already discussed in this Thesis, one of the most interesting properties of plasmon resonances is their associated near-field enhancement and confinement. The cavity mode formed in a narrow gap, is determined by the coupling of neighboring nanostructures and causes this confinement to be even more pronounced as well as more sensitive to its dielectric environment [137–139]. This phenomenon has been usually well explained by classical electromagnetic theory, which predicts strong electric field enhancements around such structural features. However, as we have shown in Chapter 3 for subnanometer gaps, the quantum mechanical effects may invalidate the classical description and lead to a reduction in the electric field enhancements [1, 54, 97, 140]. Different models have been then developed to account for electron tunneling between nanoparticles and the corresponding modification of the nature of gap plasmonic modes [38, 39, 65, 66, 141, 142].

Experimentally speaking, understanding of quantum plasmon effects has been hampered by the difficulty of experimental realization of nanostructures with precise control of gap widths in the subnanometer regime. To date, although various state-of-the-art techniques including high-resolution electron-beam lithography [3], electron-beam induced manipulation [54], dual AFM tip approaching [1], and dropcasting [140, 142], have been employed to fabricate nanoparticle dimer structures with subnanometer gaps, the fabrication of more complex system still remains challenging. A particularly promising narrow gap system in this respect is the nanosphere on a metal surface which allows the fabrication of large scale formation of a subnanometer gap reproducibly and uniformly by using a monolayer of self-assembled molecules in between [5].

Here, we apply the QCM validated for the NM structures in Chapter 3 to explain the experimental measurements of the optical response of the gold NMs composed by spherical metallic cores surrounded by a concentric metallic shells separated by a dielectric layer (see Fig. 4.1) [71, 143]. The core-shell gap can be tuned by controlling the thickness of the dielectric spacer. For the narrow gaps below 0.4 nm the structures are synthesized using SAMs as spacer layers. We show that the tunneling across the spacer layer significantly modifies the absorption cross section and the local electric field enhancements [144].

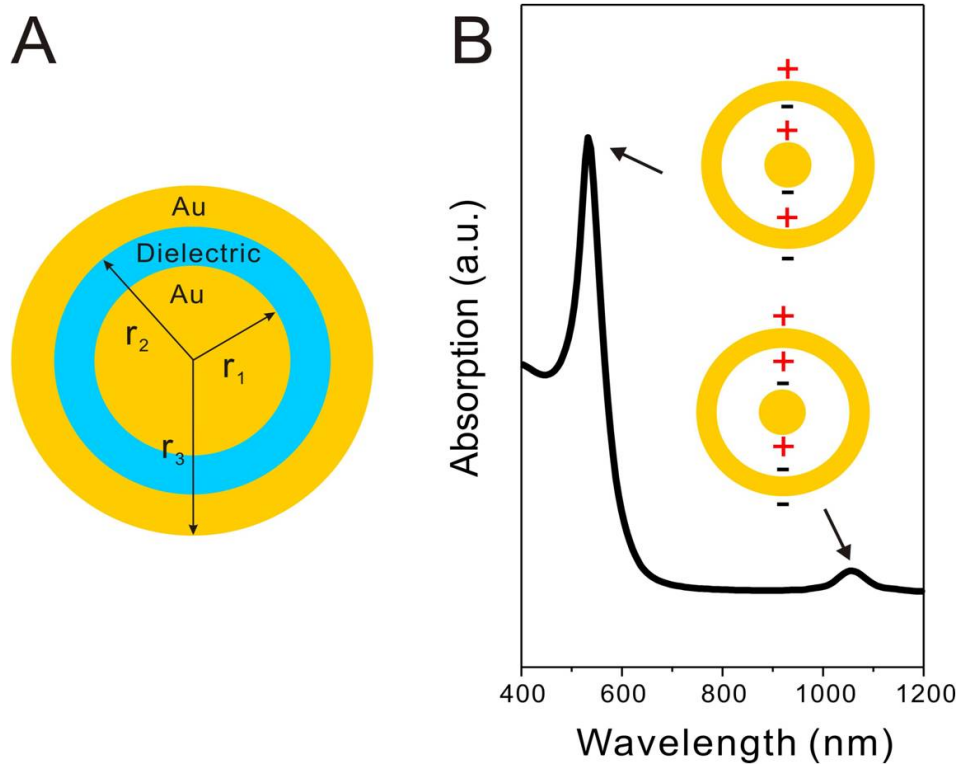

FIGURE 4.1: (A) Geometrical illustration of a gold spherical nanomatryoshka (NM). (B) Absorption cross-section calculated using classical electromagnetic theory for a NM $(r_1, r_2, r_3) = (12.5, 13.5, 30)$ nm, with a SiO_2 spacer layer. Insets represent the schematic surface charge distributions for the modes at 532 nm (left) and 1057 nm (right).

4.2. System and general considerations

We present in Fig. 4.1.A the geometry of an Au spherical NM defined by the set of structural parameters (r_1, r_2, r_3) representing the radius of the inner Au core (r_1) and the inner (r_2) and outer (r_3) radii of the Au shell. The dielectric spacer between the core and the shell consist either of a SiO_2 layer or a monolayer of 1,4-benzenedithiol (1,4-BDT) molecules. The larger gaps are realized by controlling the thickness of a SiO_2 layer inside the gaps, while the subnanometer gap is created using a self-assembled monolayer (SAM) of 1,4-BDT molecules. The mechanism followed to synthesize the gold NM's is described widely in Ref. [6].

Previous results have indicated that classical electromagnetic theory is appropriate for describing the optical response of NMs with gaps as small as 1 nm [71]. Fig. 4.1.B displays the absorption spectrum of a NM of geometry $(12.5, 13.5, 30)$ nm calculated

using classical electromagnetic theory. The calculations were performed using a standard implemented Boundary Element Method (BEM) code to solve the electromagnetic Maxwell equations[2]. The empirical dielectric functions of Au and SiO_2 were taken from Johnson and Christy [30]. The refractive index of 1,4-BDT molecules was assumed as 1.4 [137], and the whole simulation region is defined with a background index of 1.33 corresponding to water. The calculated absorption spectrum shows a strong resonance at 532 nm and a relatively weak resonance at 1057 nm, which can be explained within the framework of plasmon hybridization [145]. The resonance at 1057 nm corresponds to the excitation of the bonding hybridized plasmon of NM formed by the bonding dipolar plasmon mode of the shell with admixture of the dipolar plasmon mode of the core. The resonance at 532 nm can be assigned to a hybridized plasmon mode of the NM formed from the dipolar mode of the core and the antibonding mode of the shell. The insets of Figure 4.1.B illustrate the surface charge distributions of the two resonances. Computations based on the quantum mechanical modeling have predicted that the mode at 1057 nm is highly sensitive to quantum effects due to the high surface charge density and the right charge symmetry in the nanogap [143, 144].

4.3. Plasmon hybridization and quantum effects in NM of different sizes

In order to investigate the plasmon hybridization and the importance of quantum effects in the NMs, we studied gold NMs with three size ranges of the core-shell gap: (i) $\sim$ 100 nm, (ii) $\sim$ 10 nm and (iii) sub-1 nm. All structures were synthetized by the group of Jian Ye [6]. Fig. 4.2.A shows the schematic illustration of NMs with gaps in three size ranges. The width of the gap is taken as the main parameter influencing the plasmon coupling effects between the core and the shell. For example, a 100 nm gap size may only induce a weak plasmon coupling because the decay length of near-fields normal to the metal surface typically extends by only approx. 10 – 20 nm [146]. In contrast, a $\sim$ 10 nm gap size causes a strong coupling, hybridization, and near field enhancement. When the gap size reaches the sub-nanometer scale, electron tunneling between the core and the shell may occur and can influence both the near- and far-field optical properties,

[2]Developed by Javier Aizpurua from the Theory of Nanophotonics Group at Materials Physics Center, Donostia-San Sebastián, España and Javier García de Abajo from Nanophotonics Theory Group at Institut de Ciènces Fotòniques.

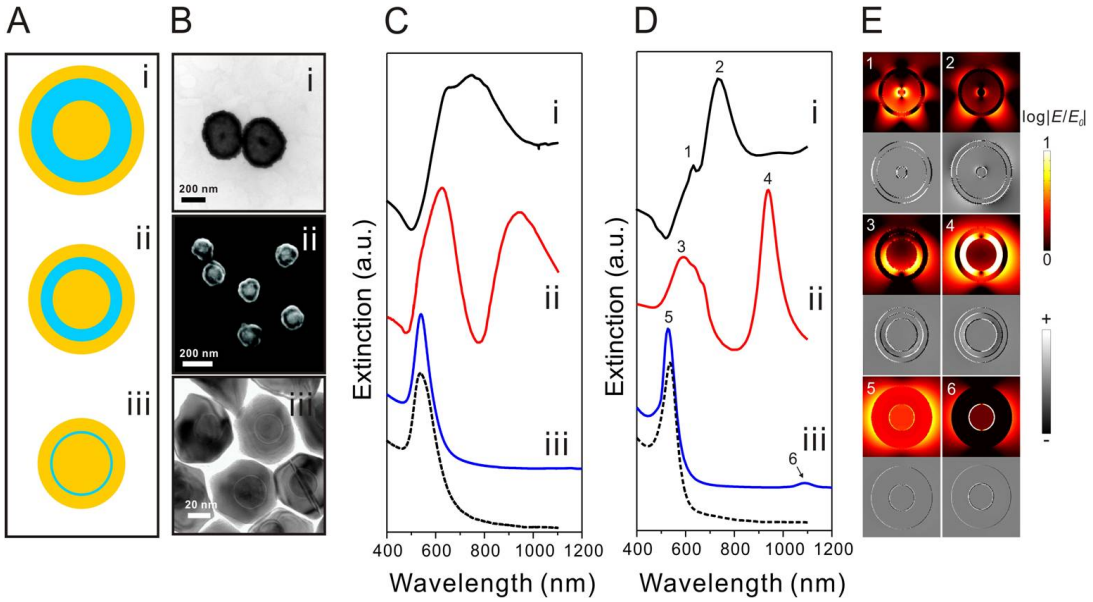

FIGURE 4.2: Optical properties of NMs of different geometries: (i) (25, 125, 150) nm with a gap size of 100 nm and with SiO_2 space layer; (ii) (40, 55, 68) nm with a gap size of 15 nm and with SiO_2 spacer layer; (iii) (10, 10.7, 25) nm with a gap size of 0.7 nm and with 1,4-BDT spacer layer. (A) Geometrical illustration, (B) TEM/SEM images, (C) experimentally measured extinction spectra, and (D) calculated extinction spectra using classical electromagnetic theory for the NMs (i-iii). Dashed lines in (C,D) show the experimentally measured and calculated extinction spectra of aqueous Au nanoparticles with a radius of 25 nm, respectively. (E) Simulated electric field intensity ($\log|E/E_0|$) distributions (top) and surface charge distributions (bottom) at resonance corresponding to the modes 1-6, using classical electromagnetic theory. The SEM image in (B) and the measured extinction spectrum in (C) for the NM (ii) were reproduced from ref [143] for comparison between the NMs with different gap sizes.

as we discussed in the Chapter 3.

TEM image of the NM in Fig. 4.2.B shows the presence of SiO_2 layer of thickness of $\sim$ 100 nm and of Au shell of thickness of 25 nm in average. The red-shift of 20 nm in the extinction spectrum also verifies the presence of the coating of SiO_2 layer on the Au cores. The measured extinction spectrum of the synthesized NMs (i, Figure 4.2C) shows two broad resonance peaks at 656 nm and 747 nm, respectively. The extinction spectrum calculated with BEM (i, Fig. 4.2D) agrees well with experimental results, indicating that the two peaks correspond to the hexapolar resonance of the outer Au shell for mode 1 and to a quadrupolar resonance for mode 2, as obtained from the calculated electric field distributions and surface charge profiles (top in Fig. 4.2.E). The strong coupling of the higher-order modes (mode 1 and 2) of the NMs to incident light is primarily attributed to phase-retardation effects due to the relatively large NM size [115]. The weak electric

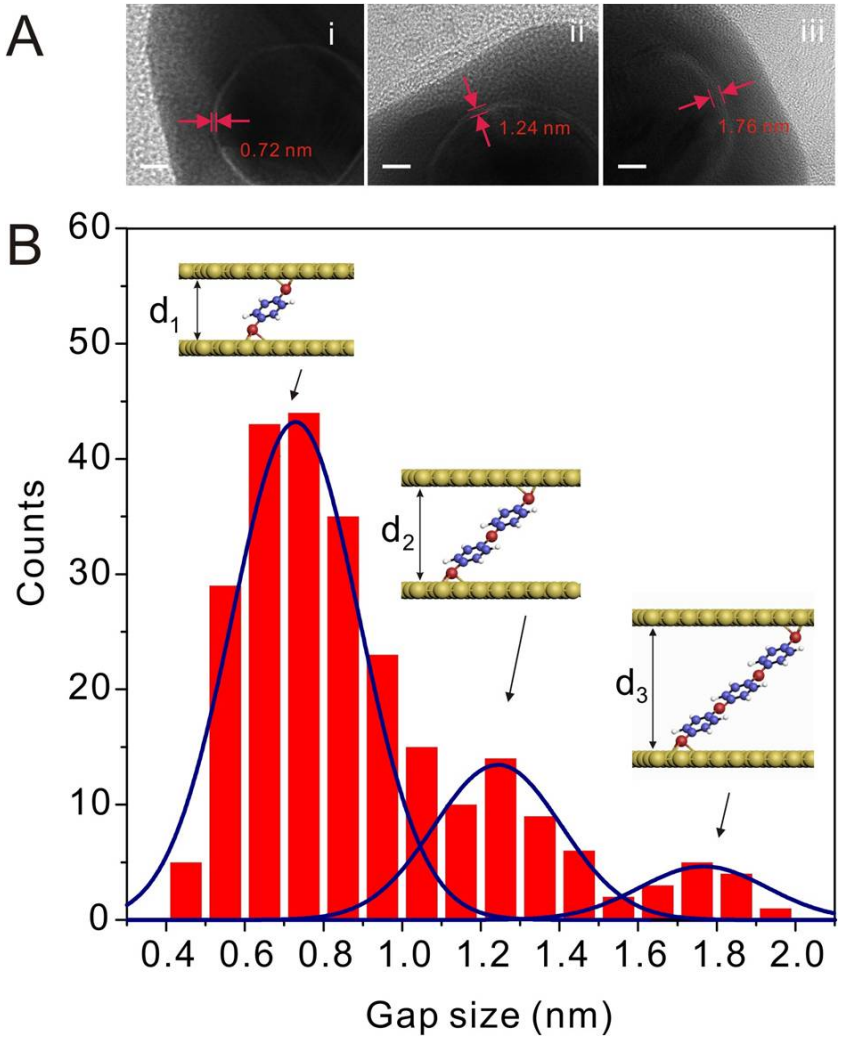

FIGURE 4.3: (A) High-resolution TEM images and (B) histogram of different gap sizes in NMs. All scale bars correspond to 5 nm. For panel B, the three gap-size peaks fitted by Gaussian model correspond to i-iii in panel A and are centered at (i) 0.72 nm; (ii) 1.24 nm; (iii) 1.76 nm. The insets in panel B illustrate the schematic hypothetical configurations of 1,4-BDT molecules inside the gaps.

field enhancements in the gap region imply a rather weak plasmon coupling between the core and the shell, and therefore the far-field optical spectrum of NMs (25, 125, 150) nm is here dominated by the scattering spectrum of the outer Au shell. However, the dipolar resonance mode (mode 1) of the Au cores is excited at 632 nm.

Experimental extinction spectrum of (40, 55, 68) nm nanomatryoshkas (gap size of 15 nm) from Ref. [119] (ii, Fig. 4.2.B) shows two intense and broad peaks at 622 nm and 943 nm (ii, 4.2C). The corresponding extinction spectrum calculated with BEM reproduces the experimental features well with two resonances at 592 nm and 940 nm, denoted

as mode 3 and 4 in Fig. 4.2.D. Mode 3 is the bonding mode resulting from the dipolar core and bonding shell modes, and mode 4 is the bonding mode arising from the core and the antibonding shell dipolar modes, as confirmed by the calculated surface charge distributions (Fig. 4.2.E). For mode 4, the pronounced electric field enhancements also suggest a significant coupling between the core and the shell plasmons optical response of NMs [147]. In addition, we note that the line width of the experimentally measured plasmon resonances is broader than those of the calculated ones, which is most likely due to the inhomogeneous effect from the polydispersed particle size of the synthesized NM's.

In order to obtain NMs with subnanometer gaps, a self-assembled monolayer of 1,4-BDT molecules was used as a spacer to uniformly and reproducibly control the core-shell separation [5]. A TEM image of NMs with a geometry of (10, 10.7, 25) nm is shown in Fig. 4.2.B (iii). The core-shell separation was calculated as 0.72 nm on average, based on the high-resolution TEM images of more than 60 nanoparticles (Fig. 4.3). Such NMs were synthesized in a layer-by-layer process, starting with the preparation of 20 nm diameter Au cores [30] (see [5] for details). Assuming that 1,4-BDT has a perpendicular orientation relative to the Au surfaces inside the gap, the gap width is given be the thickness of 1,4-BDT monolayer. Using the known bond lengths, bond angles, and the approximate distance between the sulfur atom and the ⟨111⟩ gold surface as calculated with density functional theory [148–150], the gap width can be estimated to be in the range of 0.8 nm to 1 nm for monolayer coverage. However, different gap sizes were also observed in high-resolution TEM images (Fig. 4.3A) and a series of gap sizes were carefully measured to make a histogram (Fig. 4.3B). The first peak is centered at a gap size of 0.72 nm, which likely corresponds to a slightly inclined 1,4-BDT configuration with an angle of approximately 25°-45° with the surface normal for low surface coverages. Such a tilt is in agreement previous estimates and calculations [140, 150, 151].

The second and third peaks in the histogram are centered at gap separations of 1.24 nm and 1.76 nm, which most likely corresponds to a dilayer and a trilayer of 1,4-BDT molecules, respectively (insets in 4.3.B) [150]. In addition to previous estimates by ellipsometry and calculations, TEM imaging of various gap sizes in NMs offers a direct observation of different thicknesses of 1,4-BDT molecular films on a Au surface. It has been noted that a 0.62 nm gap in NMs was reported previously and the authors had attributed the shrinkage of the 1,4-BDT monolayer to the compression of the molecules between the core and shell, proved by the up-shifts of the phenyl ring stretching mode

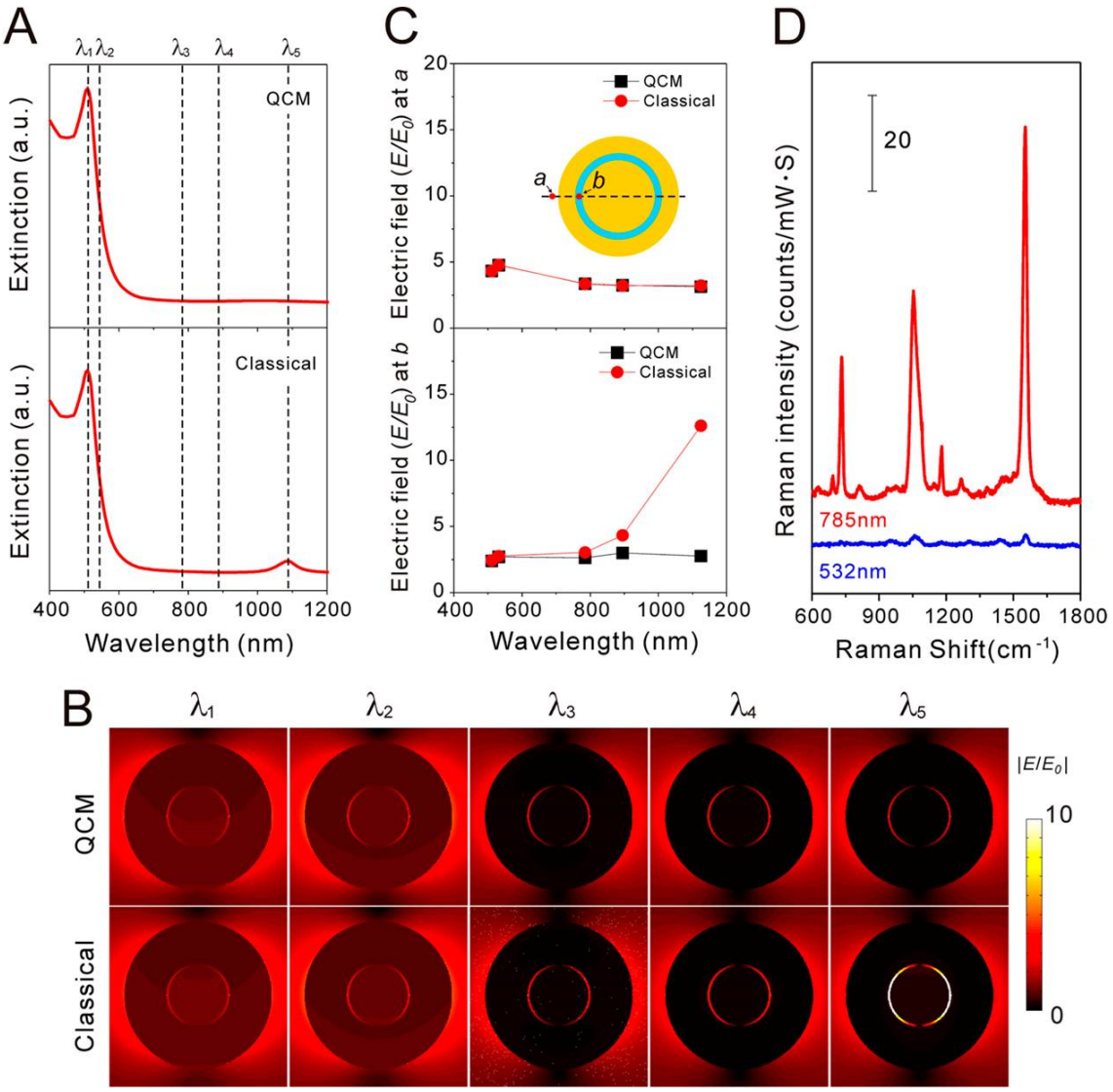

FIGURE 4.4: (A) Extinction spectra, (B) electric field distributions, and (C) electric field intensities at point a and b for a NM(10, 10.7, 25) nm calculated by QCM using conductive molecule junction (0.08 G_0 per molecule) and classical theory. Electric fields were calculated at the wavelengths of $\lambda_1 = 511$ nm, $\lambda_2 = 532$ nm, $\lambda_3 = 785$ nm, $\lambda_4 = 895$ nm, $\lambda_5 = 1100$ nm. Inset in panel C indicates the position of point a (0.1 nm apart from the outer surface of Au shell) and b (0.1 nm apart from the surface of Au core). (D) SERS spectra of NMs (10, 10.7, 25) nm with 1,4-BDT spacer layer excited by 532 nm and 785 nm laser.

and the CH bending mode in Raman spectra [143]. However, this blueshift of Raman bands was not observed in the measurement showed.

Due to their relatively small size, the extinction spectrum of such NMs is primarily dominated by the absorption cross-section as we show in Fig. 4.5. In this figure, the

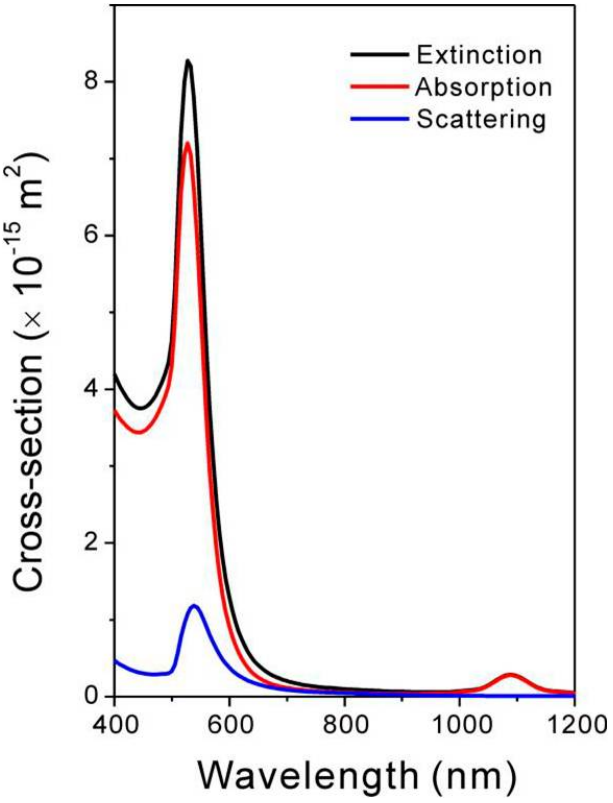

FIGURE 4.5: Absorption, scattering, and extinction cross section of a NM with a dimension of (12.5, 13.5, 30)nm.

extinction spectrum of a $(10, 10.7, 25)$ nm NM is obtained using classical electromagnetic theory (numerical BEM). The results show a noticeable resonance at 526 nm (mode 5) and a weak resonance at 1090 nm (mode 6) in Figure 4.2D, which seems to behave similarly to the plasmon hybridizations of mode 3 and 4, due to identical surface charge patterns and near-field enhancements (bottom in Fig. 4.2E). In contrast to the larger $(40, 55, 68)$ nm NM, the narrower gap leads to stronger plasmon hybridization and energy level splitting, inducing a spectral red-shift for the low energy mode and a blue-shift to the high energy mode. However, the experimental extinction spectrum (iii, Fig. 4.2.C) shows only one pronounced resonance at 539 nm, in direct contrast with the prediction by classical theory in Fig. 4.2.D (iii). Quantum mechanical modeling has predicted the disappearance of the lower energy mode (mode 6) as a direct manifestation of quantum tunneling gap below 0.4 nm [144]. However, the core shell-gap of the present system is too wide for quantum tunneling to occur between two gold surfaces. In fact, in the present system the tunneling is due to the self-assembled molecular monolayer in the plasmonic gap, where the 1,4-BDT molecules play the role of molecular wires bridging Au electrodes as has been extensively studied theoretically and experimentally in the

context of molecular electronics [151–161]. Recent studies have demonstrated that, indeed, the optical response of plasmonic systems can be affected by electron tunneling through molecular monolayers bridging narrow gaps between the particles [140, 162]. Similar to the metal-to-metal tunnel junction, the tunneling current through the molecular tunnel junction short circuits the junction, neutralizes the plasmon induced charges across the gap, and leads to the disappearance of the corresponding plasmonic mode from the optical spectra. To support this idea, we show the measured and calculated extinction spectra for homogeneous Au NP's with the same outer diameter as the NM (50 nm) (dashed lines in Fig. 4.2C, D). The measured spectrum of these solid particles agree almost perfectly with that of 1,4-BDT embedded NM's as if the gap would be absent, which points at the presence of tunneling in the $(10, 10.7, 25)$ nm NMs.

4.3.1. Quantum tunneling in NM and subnanometric molecular layers

To model the effect of quantum tunneling on the optical properties of the NM, we modified the QCM presented in the previous chapter in order to account for electron transport through the molecular layer. We model the 1,4-BDT SAM using a permittivity [162] given by:

$$\varepsilon_{SAM} = \varepsilon_\infty + i\frac{4\pi\sigma}{\omega}, \tag{4.1}$$

where $\varepsilon_\infty = 2$. Assuming a linear optical potential variation across the gap, the conductivity σ of the molecular layer is given by

$$\sigma = \frac{\alpha G_0 d}{\Sigma} \tag{4.2}$$

Here $G_0 = 7.748 \times 10^{-5} S$ is the quantum of conductance, d is the width of the gap, and $\Sigma = 0.22$ nm^2 is the typical surface area per molecule in a dense SAM [163]. The coefficient α gives the conductance of the single molecule G in units of G_0: $G = \alpha G_0$. Fig. 4.4.A shows the extinction spectra of a $(10, 10.7, 25)$ nm NM calculated using both QCM and the Boundary Element Method (BEM) [164]. In QCM calculations we use $\alpha = 0.08$, which is the lower limit of the conductance per molecule at which the plasmonic mode at $\sim$ 1100 nm disappears from the optical spectrum (see also Fig. 4.4). The results show excellent agreement between the QCM and measured spectrum with a strong dipolar mode around 520 nm but no sign of the longer wavelength hybridized mode which is present around 1100 nm in the classical approach.

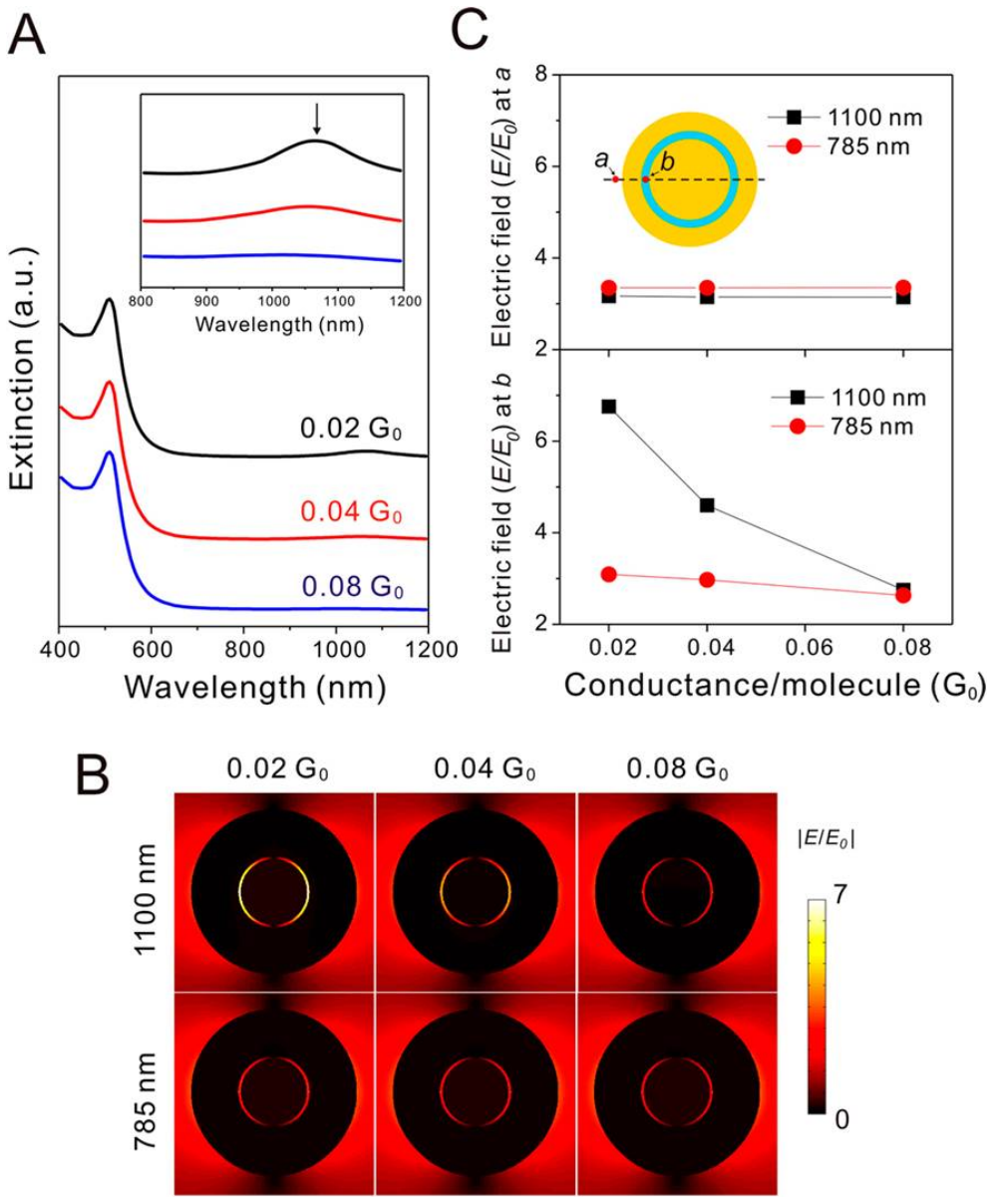

FIGURE 4.6: (A) Extinction spectra, (B) electric field distributions, and (C) electric field intensities at point a and b for a $(10, 10.7, 25)$ nm nanomatryushka calculated by QCM using conductive molecule junction with different conductances (G_0). Inset in panel A is a zoom-in around high wavelength region. Electric fields were calculated at the wavelengths of 785 nm and 1100 nm. Inset in panel C indicates the position of point a (0.1 nm apart from the outer surface of Au shell) and b (0.1 nm apart from the surface of Au core).

Several remarks are in order with respect to these results: (i) As we will also discuss in connection with Fig. 4.6, $G = 0.08G_0$, provides a lower estimate for the conductance of the 1,4-BDT SAM needed to quench the plasmon resonance at $\sim$ 1100 nm. Since $\sigma \sim \alpha/\Sigma$, less dense molecular layer than supposed here will require higher conductance per molecule to reach the same effect. (ii) The present value of the molecular conductance is within the range of the experimental and theoretical estimates for electron transport in individual 1,4-BDT molecules [151–161], particularly taking into account that the inclined configuration of SAM tends to increase the conductance values [158–161]. (iii) For the laser assisted transport in molecular junctions the ac conductance can be significantly higher that the dc conductance measured in break junctions, in particular when photon absorption opens new conductance channels through molecular orbitals [96, 165, 166].

Fig. 4.4.B shows the electric field distributions calculated by QCM and the classical approach for wavelengths of 511, 532, 785, 895 and 1100 nm. The classical approach predicts a large field enhancement in the interior gap for the 1100 nm mode while no such field enhancement is present in the QCM where the tunneling current short-circuits the gap. The distribution of electric field maps indicates that within the framework of classical theory and QCM, the near-field enhancement on the outer shell surface reaches the maximum at the hybridized dipolar resonance at short wavelength (532 nm). This qualitative information from near field maps is further analyzed in Fig. 4.4.C where we plot the electric field enhancement at the local points a and b (see the inset in Fig. 4.4.C). For example, at point a, both within the QCM or classical theory, the electric field enhancement maintains a value below 5 for all wavelengths with a maximum of 4.7 at 532 nm, which is very similar to the response of a solid spherical Au nanoparticle. For point b, classical theory predicts that the field enhancement increases when the wavelength becomes longer with a value below 5 at 511, 532, 785, and 895 nm and a maximal value of $\sim$13 at 1100 nm; while QCM shows constant field enhancements for all wavelengths with a maximal value below 3. Note the remarkably different near field behavior in plasmonic gap (for point b) at longer wavelength, where strong near field enhancement calculated with classical theory is not supported by QCM.

In Fig. 4.6.A, we show the extinction spectra the NM $(10, 10.7, 25)$ nm calculated by QCM as a function of junction conductance per 1,4-BDT molecule. As the conductance per molecule of the junction increases, the resonance at the longer wavelength gradually

decreases and finally vanishes for the largest conductance of $0.08G_0$, while the resonance at the visible range remains constant at around 520 nm. Thus, we estimate $0.08G_0$ as a lower limit for conductance per 1,4-BDT molecule needed to explain the measured spectra. Fig. 4.6.B and 4.6.C show the corresponding NM's electric field maps and the electric fields at the local points at the junction (point a) and outer shell surface (point b) at the wavelengths of 785 and 1100 nm with different junction conductances (see inset in Fig. 4.6.C). The results clearly indicate that the variation of junction conductance has much more dramatic impact on the near-field enhancement in the junction for the 1100 nm mode compared to the 785 nm mode: electric field enhancements decreases from $\sim$7 to $\sim$2.5 when the conductance increased from 0.02 to $0.08G_0$. In contrast, the variation of junction conductance has almost no influence on the near-field enhancement at the outer shell surface. With QCM modeling, the strong dependence between the junction conductance and (near and far- field) optical properties of the NM $(10, 10.7, 25)$ nm can be explained by the shortcircuiting of the gap. The modeling developed here also offers an approach to quantitatively estimate molecular conductance based on the far-field optical spectral measurement.

4.4. SERS measurement

Surface-Enhancement Raman Scattering (SERS) is a powerful probe of local field enhancements and charge transfer (CT) effects [55, 167]. In addition to the numerical calculations developed up to this point, we present SERS measurement on NM's, that were performed by the group of Jian Ye and presented jointly in [6], in order to complete the study of the near-field enhancement and electron transfer in the molecular junctions. Fig. 4.4.D shows the SERS spectra of $(10, 10.7, 25)$ nm NM's on a silicon substrate, where strong characteristic Raman bands of 1,4-BDT molecules at 729, 1055, 1551 cm^{-1} are observed when excited by 785 nm laser, and no significant bands are observed when excited by a 532 nm laser (the strong band at 900 – 1000 cm^{-1} in both spectra comes from the exterior silicon substrate). The dramatic difference between the Raman intensities of the interior 1,4-BDT molecules excited by 785 nm and 532 nm lasers can not be explained by the near-field enhancement effect since the QCM-calculated electric field intensities in the junction at 532 nm and 785 nm are almost identical and very weak (Fig. 4.4.C). We can assert that the electron transport associated with the charge transfer is the main enhancement mechanism that determines the SERS signal in the

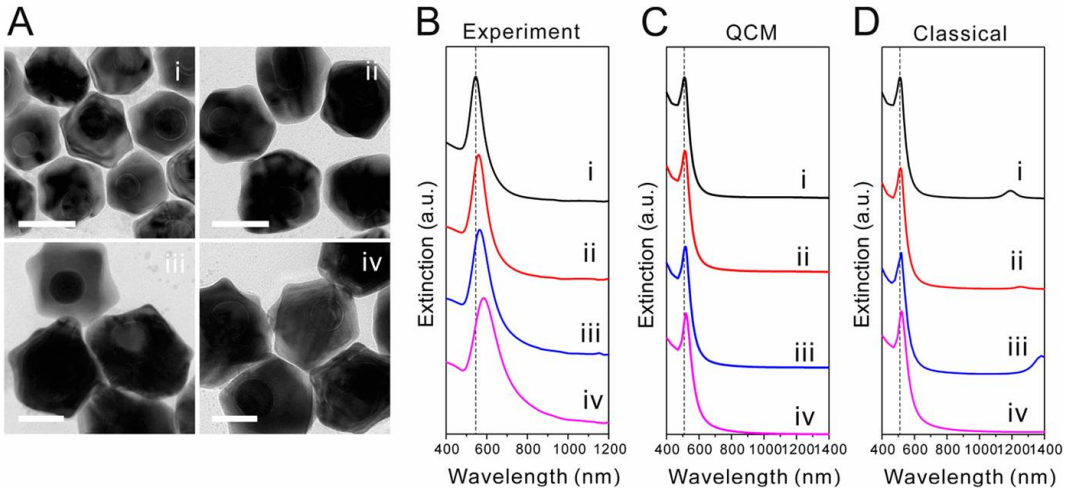

FIGURE 4.7: (A) TEM images, (B) experimentally measured and (C, D) calculated extinction spectra using (C) QCM and (D) classical electromagnetic theory for NMs (i-iv) with 1,4-BDT spacer layer and with different dimensions: (i) (12.5, 13.2, 31) nm; (ii) (14, 14.7, 37) nm; (iii) (18, 18.7, 41.5) nm; (iv) (21, 21.7, 50) nm.

$(10, 10.7, 25)$ nm NMs system, taking into account measurements and calculations made in 4-methylbenezenethiol (4-MBT) molecules, which have a very similar molecular structure to 1,4-BDT molecules [5] (not shown here).

We complete our discussion of the quenching of gap plasmons in 1,4-BDT embedded NM's, with a study of additional NM's of different geometries at subnanometric gaps (Fig. 4.7.A): (i) $(12.5, 13.2, 31)$ nm; (ii) $(14, 14.7, 37)$ nm; (iii) $(18, 18.7, 41.5)$ nm; (iv) $(21, 21.7, 50)$ nm. In each of these structures, the core-shell separation is 0.72 nm corresponding to the molecular length of 1,4-BDT. All measured extinction spectra of NMs (i – iv) display only one resonance peak at the visible regime (Fig. 4.7.B). The resonance peak red-shifts from 544 nm to 585 nm as the size of the particle is increased from 62 nm to 100 nm thus behaving as a homogeneous spherical Au NP. The QCM extinction spectra (Fig. 4.7.C) are in excellent agreement with the measured spectra. In contrast classical theory (Fig. 4.7.D) predicts additional longer wavelength modes. This agreement clearly supports our conclusion of strong electron tunneling effects through the subnanometric molecular junction of NMs.

4.5. Summary

In conclusion, using classical electromagnetic theory and QCM model approach we have theoretically investigated the optical response of Au nanomatryoshkas with core-shell gaps ranging from 100 nm to the subnanometer regime and compared theoretical results with experimental obtained on the systems. Our results confirm importance of the tunneling phenomena in subnanometric gaps. As the width of the gap is decreased, the hybridisation between core and shell plasmons increases. For subnanometer size gaps, the electron tunneling across molecular junctions between the core and the shell becomes important. It results in the charge transfer screening of the hybridized modes. Our theoretical QCM simulations successfully reproduce the measured far-field spectra and are further utilized for predicting the near-field enhancement in the molecular junction. Electron tunneling in molecular junctions also manifests itself in SERS measurement of the 1,4-BDT molecules present in the junction. The quantum properties exploited in this joint work can provide a totally new insight on the ongoing development of the strategies for optimal plasmonic SERS substrates with narrow junction gaps. The link between plasmon modes and tunneling trough SAMs in the plasmonic gap revealed here can provide a way to access the molecular conductance in the nanojunctions.

Chapter 5

Active Quantum Plasmonics

The ability of localized surface plasmons to squeeze light and engineer nanoscale electromagnetic fields through electron-photon coupling at dimensions below the wavelength, has turned plasmonics into a driving tool in a variety of technological applications, targeting novel and more efficient optoelectronic processes. In this context, the development of active control of plasmon excitations is a major fundamental and practical challenge. In this chapter, we propose a mechanism for fast and active control of the optical response of metallic nanostructures, based on exploiting quantum effects in subnanometric plasmonic cavities. By applying an external DC bias across a narrow gap (in a core-shell structure or in a plasmon dimer), a substantial change of the tunneling conductance across the junction can be induced at optical frequencies, modifying in a reversible manner the plasmonic resonances of the system. We demonstrate the feasibility of the concept with proof-of-principle calculations performed using the time dependent density functional theory (TDDFT). The results presented here, show that metal nanoparticle plasmonics can benefit from the reversibility, fast response time, and versatility of an active control strategy based on applied bias, establishing a platform for many practical applications in optoelectronics[1].

[1]This chapter, including graphs and contents, corresponds mainly to the work published in Science Advances [6]. In this team, D. C. Marinica has performed the TDDFT calculations for dimers and Mario Zapata for all the NM configurations, under supervision of Andrei Borisov. P. Nordlander, A. K. Kazansky, P. M. Echenique and J. Aizpurua contributed to succesfull discussion.

5.1. Introduction

Advances in nanofabrication techniques[168, 169] allow to engineer plasmonic response of the metal nanoparticles and nanoparticle assemblies and fully exploit strongly enhanced near fields and scattering resonances in far fields in such systems[15, 16]. Sensors[17, 168], nanoantennas allowing single molecule detection[18], medical research[20], information transfer[21], single photon generation[22], exaltation of non-linear effects[23], photochemistry[24], heat generation and hot electron injection[25], plasmon rulers[88] constitute an incomplete list of applied and fundamental research lines linked to light manipulation at subwavelength scales using plasmonic excitations. In this context the importance of an active control over plasmonic properties of a system can not be underestimated. While at present the plasmon response is mainly tuned during the fabrication procedure via shape and material engineering, or alternatively, by the choice of a particular dielectric environment[170, 171], it is highly desirable to have fast, progressive, and reversible procedures at hand to control this response. Recent experimental developments trace several possibilities for such active control that can be achieved, for instance, using flexible substrates [45, 172]; liquid crystal environment [46, 47]; tunable molecular layers [173, 174]; electrically induced thermal heating [49, 175]; all optical modulation using quantum dot arrays [50], or excitation of the free carriers [51, 52]. The latter allows to access typical electronic time scales of the order of fs (10^{-15}s), however this technique requires an incident laser of sufficient power to produce appreciable effects. In this context, electrical control of the plasmonic response via applied bias, as implemented at infrared and terahertz frequencies by graphene structures [53, 176, 177], appears extremely attractive[178] offering the possibility of control at short timescales, flexibility, and simplicity. However, practical realisations are limited to-date in to the THz or mid-IR regime because of the low doping concentrations that can be achieved electrically. The latter is also a bottleneck for applying the same strategy to the 3D bulk plasmonic metal nanostructures with high free-electron density and plasmon response at optical frequencies. So far, only solutions based on electrochemistry have been proposed in this case [179–181].

A number of recent experimental and theoretical studies on nanoparticle dimers with sub nm gaps [1, 38, 39, 41–43, 54, 55, 95–97, 122, 159, 182, 183] have demonstrated that, when efficient, quantum tunneling through the potential barrier separating nanoparticles, strongly modifies the optical response of the entire system. Under tunneling

conditions, the near field enhancement in the gap is reduced, absorption resonances owing to plasmonic modes of the capacitively coupled dimer are progressively attenuated, and charge transfer plasmon modes of the conductively coupled dimer emerge prior to the direct geometrical contact between the surfaces, as we widely discused in the last two chapters. In the tunneling regime, the conductivity (or, equivalently, conductance) across the junction is a key parameter defining the optical properties of the nanostructure. So far, the tunneling through the junction, and thus the plasmonic response, has been modified by changing the width of the gap[54, 95, 96, 182] or by using plasmonic gaps bridged by self assembled molecular layers[97, 159]. We develop a completely new strategy and show that the bias voltage dependence of the electron tunneling through narrow gaps can be used for active electrical control of the plasmonic response of the embedding metallic nanostructures. Indeed, similar to scanning tunneling microscopy[184–186] at DC, the tunneling barrier and thus the conductance through the junction can be controlled not only by the variation of the junction size, but also by an applied bias.

5.2. Model and qualitative aspects

Fig. 5.1 sketches the concept of the proposed control strategy. As shown in Fig. 5.1(a), in the geometrical tuning of the plasmon response, change of the width of the gap modifies the tunneling barrier and thus the conductance of the junction. For the fixed geometry, as shown in Fig. 5.1(b), the modification the tunneling barrier can be produced applying bias between metal nanoparticles separated by narrow gaps. As a consequence, the conductance across the junction at optical frequencies, and therefore the plasmonic modes of the nanostructure, can be modified in a controllable way. This allows to achieve an active and flexible control of the optical response of the system at the fast (typically ps 10^{-12}s) time scales needed to bias the system.

In order to demonstrate the sought controllable modification of the optical response, we perform a proof-of-principle calculation for two representative systems characterised by the presence of a narrow plasmonic gap: (i) the cylindrical core-shell nanomatryoshka (NM), and (ii) the spherical plasmonic dimer, as schematically shown in Fig 5.2(e) and (f), respectively. The NM (R_1, R_2, R_3) consists of an infinite cylindrical metallic core of radius R_1, and a coaxial cylindrical metallic shell characterized by an internal radius R_2 and external radius R_3, using the standard notations introduced in Chapter.3. The spherical plasmonic dimer is formed by two identical spherical metallic particles of radius

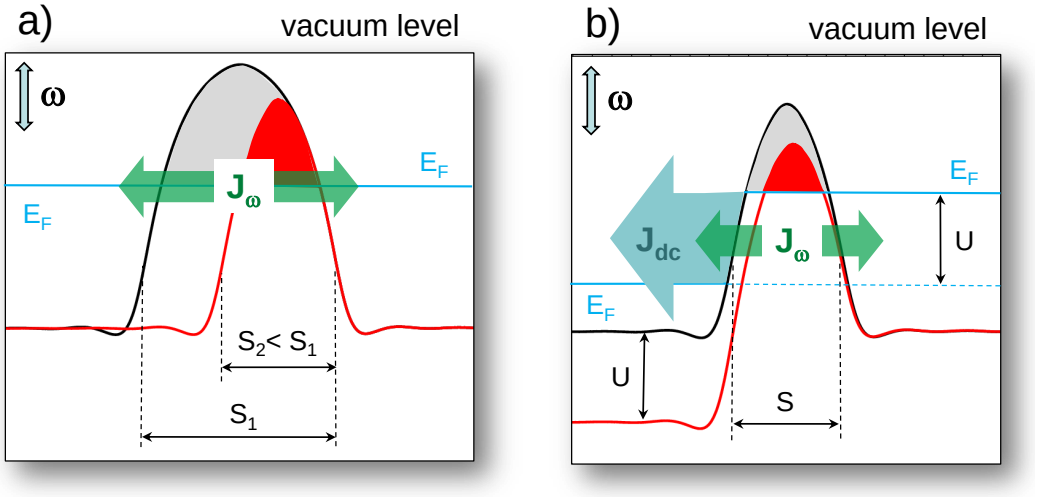

FIGURE 5.1: Schematic representation of the concept underlying the active control strategy. The evolution of the tunneling barrier separating two metal surfaces across the junction is shown for two situations. a) The junction width is reduced from S_1 to S_2. The Fermi levels E_F of the left and right leads are aligned (shown with blue lines). b) A bias U is applied to the left lead, while the width of the junction S is kept fixed. The shaded gray (red) area represents the tunneling barrier for the electrons at the Fermi energy of the right lead before (after) modification of the tunneling barrier by the reduction of the width of the junction in panel a), or by the applied bias in panel b). The presence of the incident electromagnetic field at frequency ω induces a modulation of the one-elecron potentials, as represented with the vertical arrow on the top left corner of the panels. Horizontal green and blue arrows show, respectively, the AC current J_ω due to the optical potential, and the dc current J_{DC} due to applied bias U.

R separated by a narrow gap of width S. Both systems exhibit distinctive plasmonic modes characterized by the optical fields strongly enhanced in the gap. These modes are thus particularly sensitive to the tunneling through the junction [3, 38, 39]. Indeed, when the tunneling current is established it partially neutralizes the induced charges of opposite sign at facing surfaces across the junction, thus altering the near fields and electromagnetic couplings between the individual parts of the composite structure.

We identify the plasmon resonances sensitive to the AC current across the gap for the cases of the nanomatryoshka and the dimer in their absorbance spectra showed in Fig. 5.2(a) and Fig. 5.2(b). We use classical electromagnetic calculations in the quasistatic approximation, in order to obtain these spectra. This approach is well justified because the relevant system sizes are much smaller that the wavelength of the incident electromagnetic wave, and because the tunneling is negligible for the geometries with 8.5 Å wide gaps as considered in Fig. 5.2. Without loss of generality a vacuum gap is

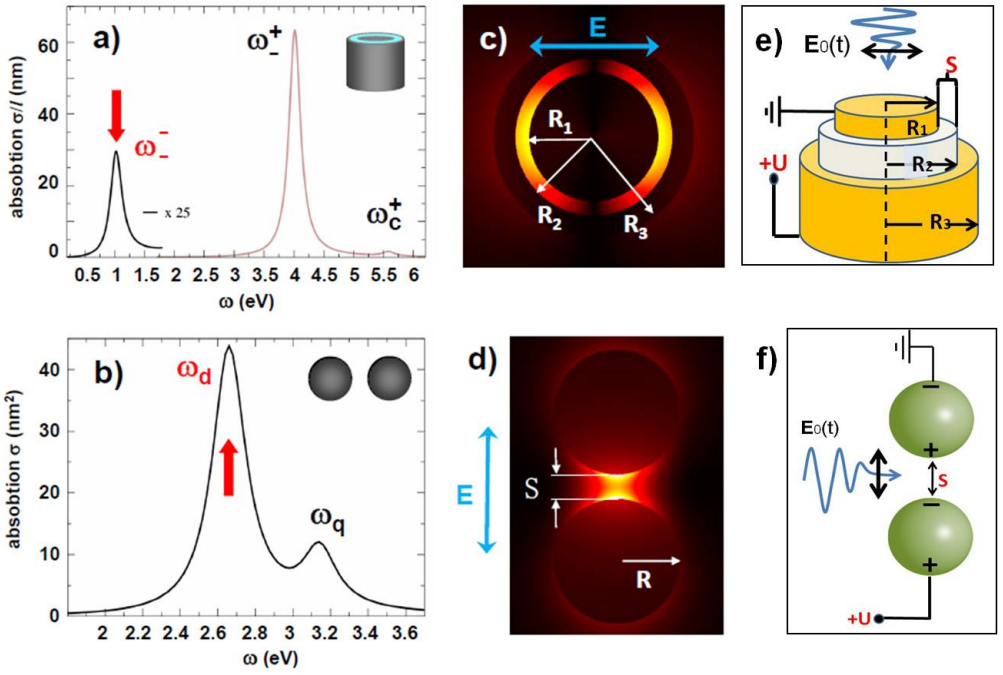

FIGURE 5.2: Systems studied. Panels a), c): optical response of a cylindrical core-shell NM characterized by the radius of the core R_1, and internal R_2 and external R_3 radii of the shell. Results are shown for the ($R_1 = 39.2$ Å, $R_2 = 47.7$ Å, $R_3 = 61$ Å) NM with the core shell gap $S = R_2 - R_1 = 8.5$ Å. Panels b), d) show the same information for a plasmonic dimer formed by the two spherical nanoparticles with radius $R = 21.7$ Å separated by the gap of the width $S = 8.5$ Å. Panel a) shows the absorption cross section per unit length σ/l for cylindrical NM. The absorption resonances are labelled according to the underlying plasmonic modes. ω_-^-: bonding hybridized plasmon, ω_-^+: resonance with core character, and ω_c^+: nonbonding mode with shell character. Panel c) shows the near field distribution for an incident plane wave polarised as sketched with blue arrow and resonant with the ω_-^- mode of the NM. Panel b) shows the absorption cross section σ for the spherical dimer. The absorption resonances are labelled according to the underlying plasmonic modes. ω_d: bonding dipolar plasmon, ω_q the bonding quadrupolar plasmon. Panel d) shows the near field distribution calculated for an incident plane wave polarised as sketched with the blue arrow and at resonance with the ω_d plasmon mode. In the panels a) and b) the resonances most sensitive to tunneling and thus subject to active control are marked with red arrows. Panels e) and f) sketch the cylindrical and spherical dimer systems under bias, respectively.

assumed in all calculations, nevertheless the possibilities offered by the dielectric filling of the gap are discussed below in this Chapter. In the case of the cylindrical NM [Fig. 5.2(a)], the gap plasmon most sensitive to the tunneling is a bonding hybridized mode ω_{-}^{-} associated with the low energy absorption resonance as already discussed in Chapter. 3. For the spherical dimer [Fig. 5.2(b)], the gap plasmon most sensitive to the tunneling is a bonding dipole plasmon ω_d widely discussed in the literature [1, 38, 39, 41, 183]. This mode is associated with the main absorption peak. The intensities of the resonant near fields for the ω_{-}^{-} and ω_d gap plasmon modes of the NM and spherical dimer are shown in Fig. 5.2(c) and Fig. 5.2(d). As pointed out, these absorption resonances marked with red arrow in Fig. 5.2 are very sensitivity to electron tunneling and thus offer a great opportunity to exploit our concept of quantum control with an applied bias.

5.3. TDDFT framework

We use the Kohn-Sham (KS) scheme within Time Dependent Density Functional Theory (TDDFT) to perform the quantum-mechanical study of the electron dynamics triggered in plasmonic nanoobjects by an external perturbation. Along with calculation of the linear response TDDFT allows to follow the real time evolution of the electron densities currents and fields in the system. The TDDFT is a well established state-of-the-art *ab initio* approach for the treatment of both linear and nonlinear response to optical excitations in molecules, clusters, and solids[124, 187, 188]. The cylindrical core-shell nanomatryushka (NM), as well as spherical dimer (SD) are treated within the jellium model (JM) detailed for these geometries in earlier publications [39, 42, 189]. The ionic cores are represented by uniform background density of positive charge $n_+ = \left(\frac{4\pi}{3}\ r_{\rm s}^3\right)^{-1}$ (we use atomic units unless otherwise stated). The Wigner-Seitz radius $r_{\rm s}$ is set equal to 4 a_0 (Bohr radius a_0=0.53 Å) corresponding to the Na metal which is a prototype system for the jellium description. In the case of the (R_1, R_2, R_3) cylindrical nanomatryoshka (NM) we use variable R_1, and fixed $R_2 = 90$ a_0 ($\simeq$ 47.7 nm), and $R_3 = 115$ a_0 ($\simeq$ 6.1 nm). Here, to define the structure we use the same notations as in Ref. [3] and descibed in Chapter. 3. Thus, depending on the geometry, the system comprises up to 620 conduction electrons per unit length. In the case of the spherical dimer each nanoparticle has a closed shell structure and consists of $N_{\rm e} = 1074$ electrons. The cluster radius is $R = N_{\rm e}^{1/3}\ r_{\rm s} = 40.96$ a_0 ($\simeq$ 21.7 Å). In all cases considered here the Fermi energy of the

ground state system is $E_{\mathrm{F}} \approx -2.9$ eV with respect to the vacuum level.

Within the TDDFT the time-dependent electron density is given by

$$n(\mathbf{r},t) = \sum_{j\in occ} |\psi_j(\mathbf{r},t)|^2 \tag{5.1}$$

with the summation running over all occupied KS orbitals $\psi_j(\mathbf{r},t)$. The time evolution of KS orbitals is given by the time-dependent Scrödinger equation:

$$i\frac{\partial\psi_j(\mathbf{r},t)}{\partial t} = \{\mathbb{T} + V_{\mathrm{eff}}(\mathbf{r},t;n(\mathbf{r},t))\}\,\psi_j(\mathbf{r},t). \tag{5.2}$$

Here, $\mathbb{T} = -\frac{1}{2}\Delta$ is the kinetic energy operator, and $V_{\mathrm{eff}}(\mathbf{r},t;n(\mathbf{r},t))$ is the effective KS potential that depends on the electron density. It is thus generally time-dependent through the time-dependence of $n(\mathbf{r},t)$. $V_{\mathrm{eff}}(\mathbf{r},t;n(\mathbf{r},t))$ comprises three terms:

$$V_{\mathrm{eff}}(\mathbf{r},t;n(\mathbf{r},t) = V_{\mathrm{H}}(\mathbf{r},t;n(\mathbf{r},t)) + V_{\mathrm{xc}}(\mathbf{r},t;n(\mathbf{r},t)) + V_{\mathrm{ext}}(\mathbf{r},t). \tag{5.3}$$

The first term in Eq. (5.3) is the Hartree potential for the electron interaction with total charge density $n_+ - n(\mathbf{r},t)$. We use the non-retarded approximation which should be valid considering the electric field polarisation and small radii of the NM and SD considered here. The second term in Eq. (5.3) is the exchange correlation potential. We use the adiabatic local density approximation (ALDA) described in [124, 188, 190] with exchange correlation kernel of O. Gunnarsson and B. I. Lundqvist [191]. Finally, the last term describes external perturbation which can be the electromagnetic field and/or applied bias. With KS orbitals represented on a mesh in cylindrical coordinates, Eqs. (5.2) are solved using real-time propagation similar to that used in the one-electron wave packet propagation in cylindrical coordinates as detailed in [192, 193].

The linear properties are obtained from the response to a weak impulsive potential. To this end we set: $V_{\mathrm{ext}}(\mathbf{r},t) = \gamma\hat{p}\mathbf{r}\delta(t)$, where γ is a small constant. The unit length vector $\hat{p}$ defines the polarization direction of the incident linearly polarized plane wave, so that $\hat{p}\mathbf{r}$ is the coordinate along the polarization direction. For the cylindrical core-shell NM $\hat{p}$ is perpendicular to the symmetry axis, and it is along the symmetry axis for the spherical dimer. The Fourier time-to-frequency transform of the near fields and of the induced dipole moment allows us to calculate the frequency-resolved fields in the plasmonic gap as well as the optical absorption cross-section given by $\sigma(\omega) = \frac{4\pi\omega}{c}\mathrm{Im}\{\alpha(\omega)\}$. Here

$\alpha(\omega)$ is the dipolar polarizability of the system. To converge the results, an artificial frequency broadening of 0.15 eV is used, as typical for the TDDFT calculations on small systems [38, 39, 122, 194]. For the small system sizes considered here the absorption and extinction cross-section can be considered to be equal.

The initial conditions for the time dependent Eqs. (5.2), $\psi_j^0(\mathbf{r}) \equiv \psi_j(\mathbf{r}, t = 0)$, correspond to the K-S orbitals of the ground-state system, which implies that prior to using TDDFT one performs the standard density functional theory (DFT) study. The K-S orbitals $\psi_j^0(\mathbf{r})$ satisfy the stationary Kohn Sham equations:

$$\begin{aligned} \left\{T + V_{\text{eff}}^0(\mathbf{r}; n)\right\} \psi_j^0(\mathbf{r}) &= E_j \psi_j^0(\mathbf{r}), \\ n(\mathbf{r}) &= \sum_{j \in occ} \left|\psi_j^0(\mathbf{r})\right|^2 \end{aligned} \tag{5.4}$$

where E_j is the energy of the K-S orbital. The effective potential

$$V_{\text{eff}}^0(\mathbf{r}; n) = V_{\text{H}}^0(\mathbf{r}; n) + V_{\text{xc}}^0(\mathbf{r}; n) \tag{5.5}$$

is time independent. We use superscript ^{0} to refer to the ground state system.

While the ground state electronic properties of the spherical dimer have been shown in number of publications [38, 39, 122, 194], the NM is much less discussed [3]. In Fig. 5.3 we show the ground state electron densities and effective potentials V_{eff} calculated with DFT for the cylindrical NM with geometry given by (R_1, 90 a_0, 115 a_0) or, equivalently, ($R_1, R_2 = 47.7$ Å$, R_3 = 61$ Å). Results are presented for two values of the core radii $R_1 = 60$ a_0 (31.8 Å), and $R_1 = 82$ a_0 (43.5 Å) corresponding to the gap size $S = R_2 - R_1$ equal to $S = 30$ a_0 (15.9 Å) and $S = 8$ a_0 (4.2 Å) respectively. In the first case the potential barrier between the core and the shell is wide and the core and the shell are coupled only capacitively with negligible tunneling through the gap. In the second case, the tunneling contact through the narrow potential barrier is established. Along with evolution of the potential barrier, one can also notice an extension of the electron density profile beyond the jellium edge. This is particularly well seen for the external surface of the NM, where the electron density extends outside the boundary located at $R_3 =$ 115 a_0 (61 Å). The spill out of the electron density outside the nanoobject boundaries results in a red shift of the dipolar plasmon frequency as compared to the prediction of the classical theory [56, 122, 195]. Thus, for the individual spherical nanocluster

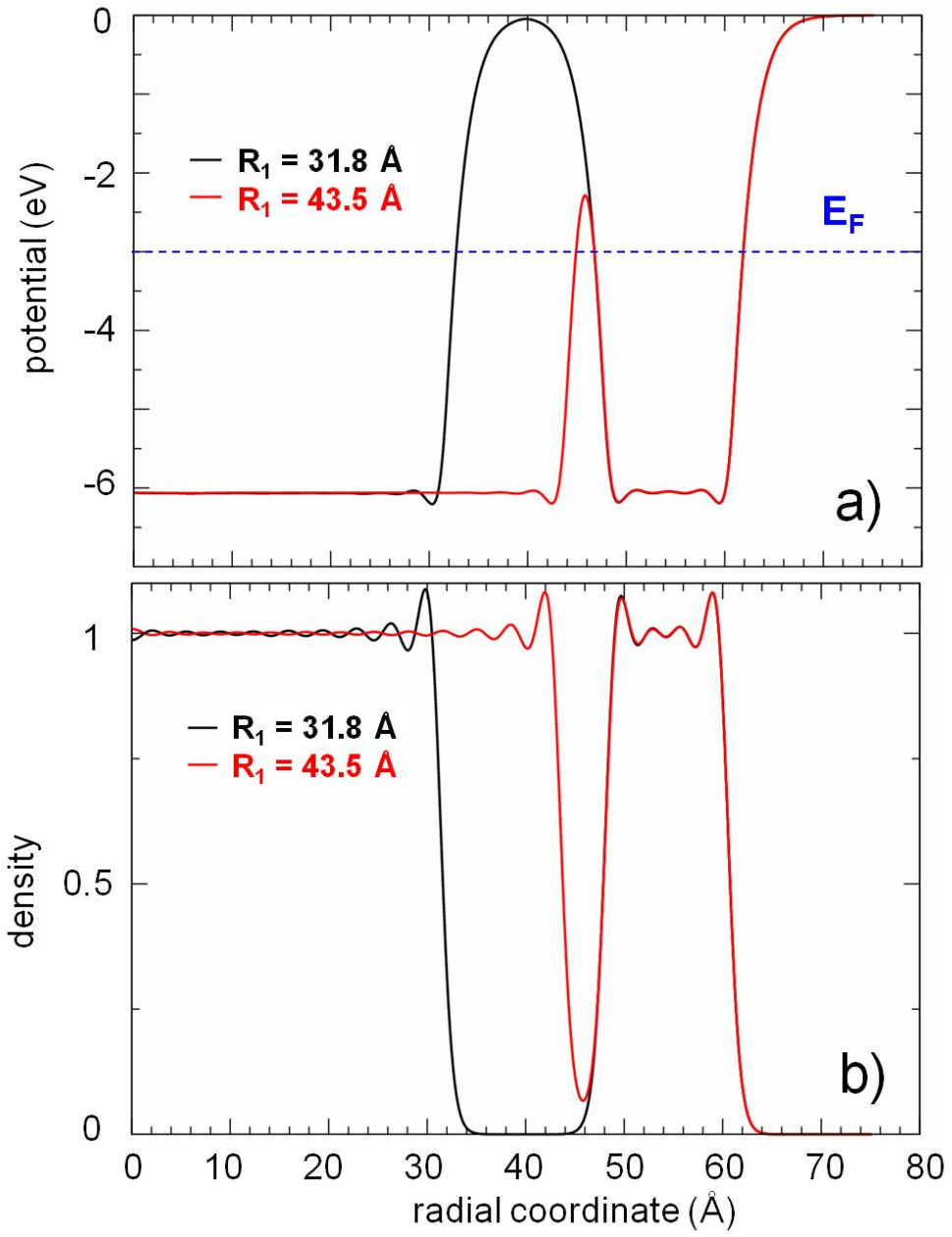

FIGURE 5.3: Effective one-electron potential (a), and ground state electron density (b) of the (R_1, $R_2 = 47.7$ Å, $R_3 = 61$ Å) cylindrical NM. Results are shown as function of the radial coordinate. Black lines: the NM with core radius $R_1 = 31.8$ Å and gap size $S = 15.9$ Å; Red lines: the NM with core radius $R_1 = 43.5$ Å and gap size $S = 4.2$ Å. The Fermi level is shown with dashed blue line in the panel (a).

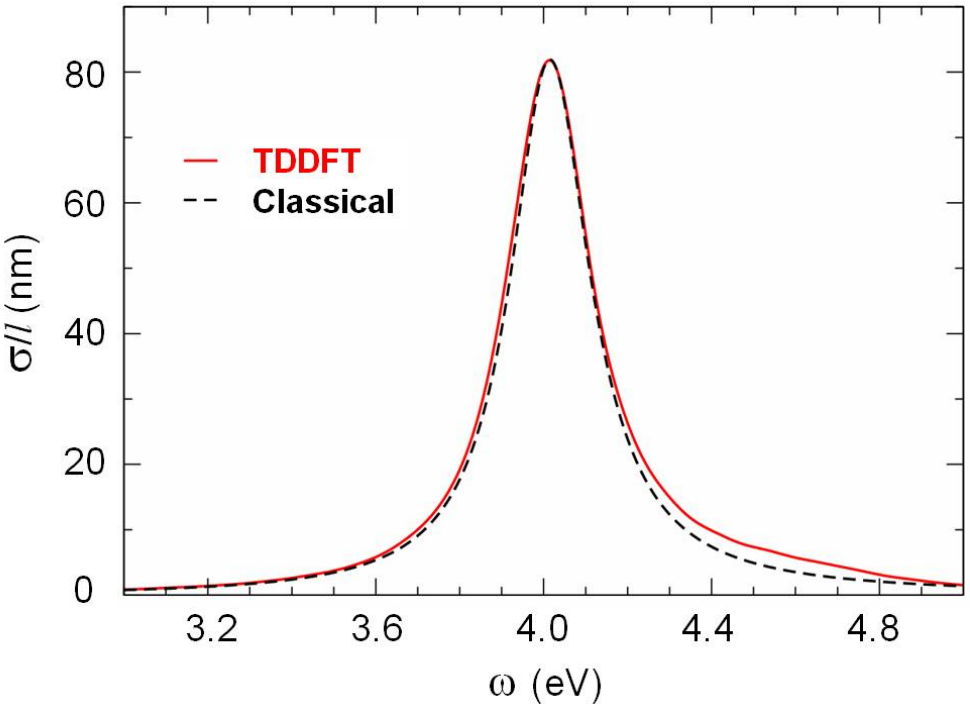

FIGURE 5.4: Frequency dependent absorption cross section per unit length for the infinite cylinder with radius = 61 Å. The incident plane wave is linearly polarised with electric field vector perpendicular to the cylinder axis. The quantum TDDFT calculations (red line) are compared with classical calculations (black dashed line). Classical theory uses Drude model for the dielectric function of Na with parameters adjusted to TDDFT result.

with radius $R = 40.96$ a_0 (21.7 Å) the maximum of the dipolar plasmon resonance in absorption spectra is reached at the frequency $\omega_{\rm sph} = 2.98$ eV. This is lower than the frequency of the quasistatic Mie resonance for the sphere $\omega_{\rm sph}^{class} = \omega_p/\sqrt{3} = 3.4$ eV. Here $\omega_p = \sqrt{4\pi n_+} = 5.89$ eV is the Drude plasma frequency of Na. Similarly, for the individual cylinder with radius $R = R_3 = 115$ a_0 (61 Å) the dipolar plasmon resonance in absorption spectra shown in Fig. 5.4 appears at $\omega_{\rm cyll} = 4.02$ eV which is lower than the classical value $\omega_{\rm cyll}^{class} = \omega_p/\sqrt{2} = 4.16$ eV.

5.3.1. Tunneling effects

To study the quantum tunneling effects in this canonical structures, the TDDFT calculations are compared with classical electromagnetic theory where the dielectric function of Na is described within the Drude model (DM), given by Eq. 1.2. The attenuation and the plasma frequency are, respectively, $\eta = 0.218$ eV and $\omega_{\rm p} = 5.16$ eV. The latter

is lower than the nominal Drude frequency 5.89 eV for Na metal. This choice of parameters allows to account for the spill out effects and plasmon line broadening because of the decay into electron-hole one-particle excitations [196]. The good agreement with TDDFT calculations for the individual nanowire is then reached as shown in Fig. 5.4 (similar agreement is reached for the individual nanosphere).

Provided good agreement between benchmark results for the individual nanoobjects, the main differences between the TDDFT and classical Drude calculations for plasmonic dimer or core-shell NM can be then attributed to electron tunneling. For the narrow gaps the electron tunneling strongly modifies optical response of the core shell NM and SD as follows from Fig. 5.5. In the panel a) of the Figure we show the absorption cross section per unit length of the cylindrical NM. The frequency range corresponds to the low energy bonding hybridized resonance ω_{-}^{-}. When the width of the gap reduces below 5.5 Å the tunneling current becomes strong enough leading to partial neutralization of the plasmon induced charges across the gap. As the gap width reduces, the tunneling efficiency grows, and the ω_{-}^{-} resonance broadens and progressively disappears. For the gap size $S = 4$ Å the corresponding plasmon mode is quenched. Similar behaviour is calculated for the bonding dipole plasmon of the spherical dimer. For the gap size below 4 Å the plasmon resonance in the absorption cross section becomes broadened by the tunneling effects, and it basically disappears for $S = 2$ Å. Notably, as compared to the NM, the smaller gap size is needed in the case of the spherical dimer to reach the same tunneling efficiency. Indeed, the NM is characterised by the extended contact between the core and the shell where the tunneling current flows transversally through the entire core-shell gap. This is while in the case of the spherical dimer the tunneling current is confined to the narrow contact region around the symmetry axis of the dimer.

5.3.2. TDDFT approach for the systems under applied bias.

To achieve the control of the plasmon response while keeping the applied bias low, we reduce the gap size down to 6 Å where tunneling effects, albeit weak, do appear. The optical response of the ground state systems and that of the system under bias are obtained from the quantum mechanical Time Dependent Density Functional Theory (TDDFT)[188] calculations. The presence of the applied bias implies that the DC current flows through the gap. This situation represents a real challenge for the TDDFT

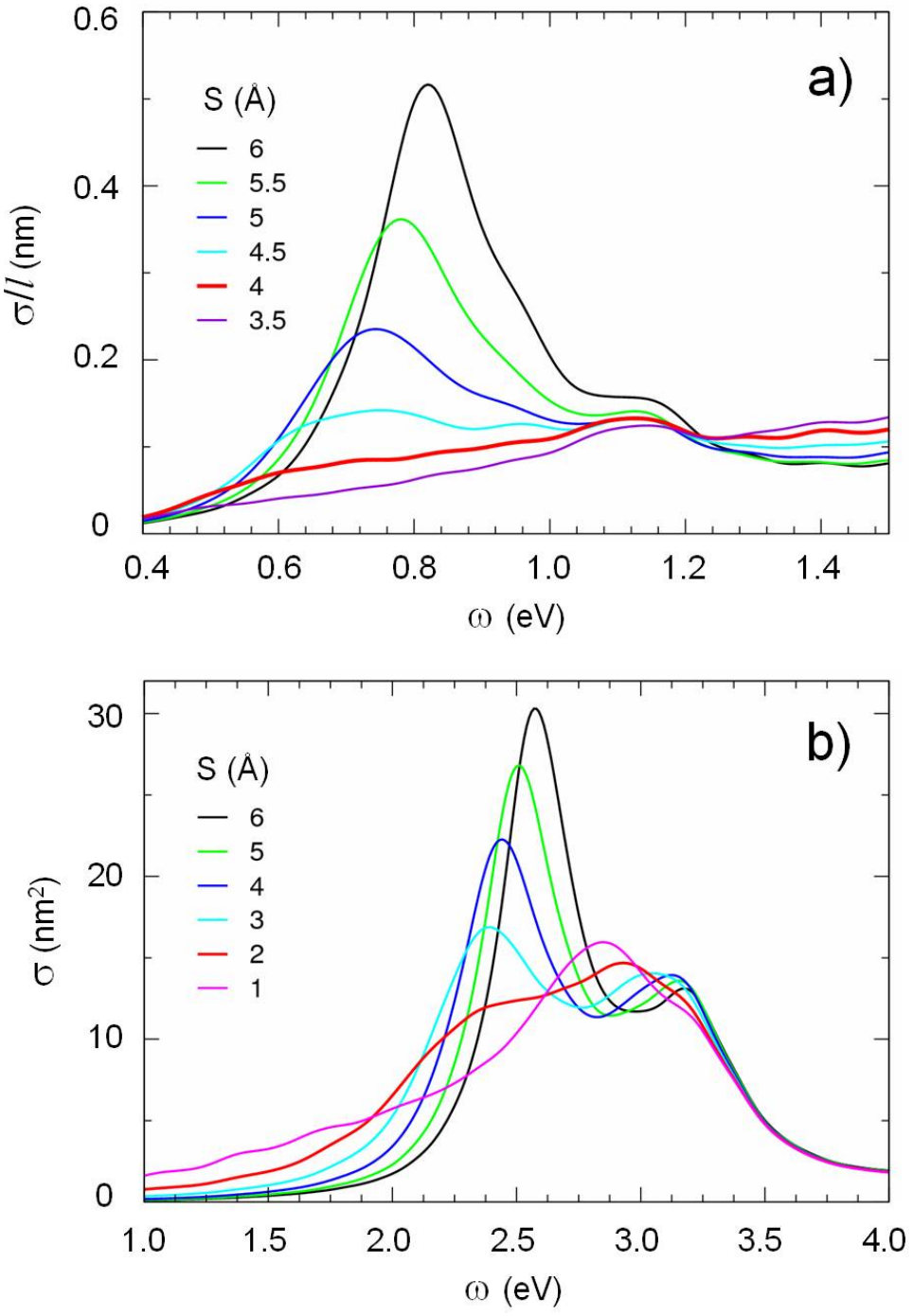

FIGURE 5.5: Absorption spectra calculated with TDDFT for cylindrical (R_1, R_2 = 47.7 Å, R_3 = 61 Å) NM [panel a)], and R = 21.7 Å spherical dimer [panel b)]. The incident plane wave is linearly polarised with electric field vector perpendicular to the NM axis [panel a)], and parallel to the dimer axis connecting nanoparticle centers [panel b)]. Results are shown for different sizes of plasmonic gap as indicated in the insets.

calculations performed here for a finite size system with a fixed number of electrons. Several methods have been proposed in literature [197–199] in order to obtain the transitory steady state regime needed for the calculation of the absorption spectra. We used two approaches and concluded on their near equivalency. (i) The first approach one consists in calculating the ground state of the system in the presence of an external potential. The system is polarized by the charge transfer between nanoparticles, and removal of the external potential triggers the tunneling current. (ii) The second approach consist in applying bias directly to the ground state of the non-polarized system.

In the case of the core shell NM we used the following strategy. First, we used the stationary DFT to calculate the KS orbitals and an electron density of the system under the action of the time-independent external potential V^b_{ext}.

$$\begin{aligned} \left\{T + V^b_{\text{eff}}(\mathbf{r}; n)\right\} \psi^b_j(\mathbf{r}) &= E_j \psi^b_j(\mathbf{r}), \\ n(\mathbf{r}) &= \sum_{j \in occ} \left|\psi^b_j(\mathbf{r})\right|^2 \end{aligned} \tag{5.6}$$

where $V^b_{\text{eff}} = V^b_{\text{H}} + V^b_{\text{xc}} + V^b_{\text{ext}}$, and the external potential is given by

$$\begin{aligned} V^b_{\text{ext}} &= V_0, \ \rho < R_1, \\ V^b_{\text{ext}} &= V_0 \frac{\ln(\rho/R_2)}{\ln(R_1/R_2)}, \ R_1 \leq \rho \leq R_2, \\ V^b_{\text{ext}} &= 0, \ R_2 < \rho, \end{aligned} \tag{5.7}$$

here (ρ, ϕ, z) are the cylindrical coordinates. Superscript b indicates that the DFT calculations were performed in the presence of an external time-independent potential. The bias is applied to the core, and the shell is assumed to be grounded. For $V_0 > 0$ the polarisation of the system is linked with electron transfer from the core to the shell. The induced density screens the applied DC field so that the final total self-consistent potential is very close to that of the ground state system without an external perturbation $V^b_{\text{eff}} \approx V^0_{\text{eff}}$ as we illustrate in Fig. 5.6 a). This is because the electron density of the system is changed only slightly by the applied potential. Indeed, the potential of the charged cylinder is $V_Q = 2Q \ln(\rho)$, where Q is the charge per unit length. Then for the (78 a_0, 90 a_0, 115 a_0) NM geometry [(41.3 Å, 47.7 Å, 61 Å)] the transfer of one electron (out of 285) per 1 a_0 length results in the 7.8 eV bias between the core and the shell. Thus, as a consequence of the screening we have:

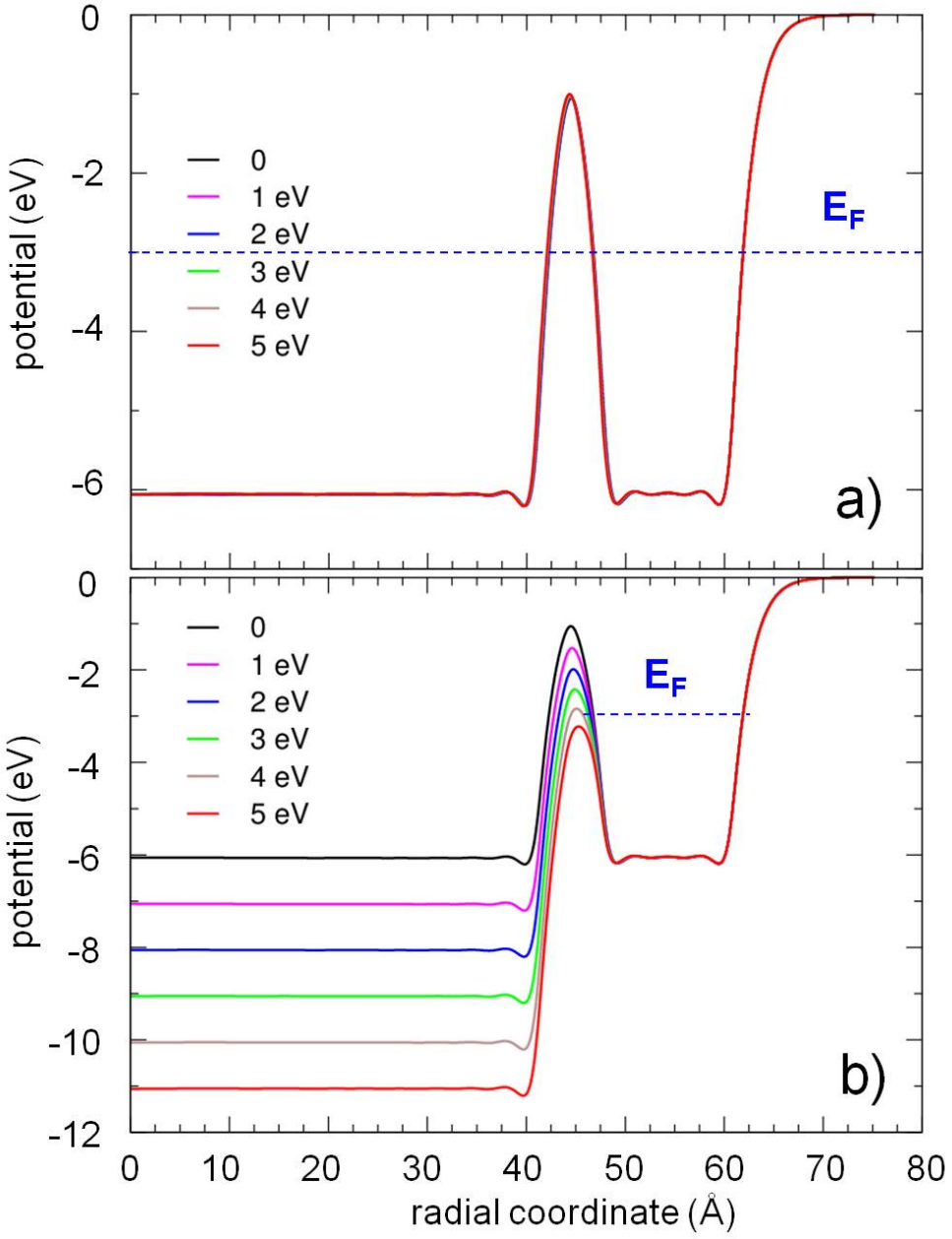

FIGURE 5.6: a) Effective one-electron potentials V^b_{eff} obtained from the self-consistent DFT calculations for the (41.3 Å, 47.7 Å, 61 Å) NM under applied external potential given by Eq. (5.7). Calculations were performed for different amplitudes V_0 of the applied external potential as explained in the insert. b) Hartree and exchange-correlation contribution $V^b_{\text{H}} + V^b_{\text{xc}}$ to the total V^b_{eff} potential calculated for different magnitude V_0 of the applied external potential as explained in the insert. Dashed lines show position of the Fermi level of the system.

$$V_{\rm H}^b + V_{\rm xc}^b \approx V_{\rm eff}^0 - V_{\rm ext}^b, \tag{5.8}$$

where the effective potential of the ground state system without an applied bias, $V_{\rm eff}^0$, is given by Eq. (5.5). We obtain that the sum of the Hartree and exchange-correlation contributions to the self-consistent potential calculated in the presence of the $V_{\rm ext}^b$ reproduces the situation where the $-V_{\rm ext}^b$ potential is applied to the ground state system. This corresponds to the V_0 bias applied to the core. Indeed, the V_0 bias results in the $\bar{e}V_0 = -V_0$ potential acting on the core electrons ($\bar{e} = -1$ is the electron charge). The effective one-electron potential obtained with different magnitude V_0 of the external potential is shown in Fig. 5.6 b). It is worth noting that inspection of the figure clearly shows that the tunneling barrier between the core and the shell is reduced by applied bias. For V_0 above 4 eV, the electrons at the Fermi level of the shell can escape into the core via an efficient over-the-barrier transition. For the reasons, explained below we will denote V_0 as *targeted bias*.

Once the self-consistent solution of Eq. (5.6) with external potential $V_{\rm ext}^b$ given by Eq. (5.7) has been obtained with DFT, the stationary KS orbitals $\psi_j^b(\mathbf{r})$ are used as initial states for the second, TDDFT step of the study. The time dependent KS equations Eq. (5.2) and Eq. (5.3) are solved with time-dependent potential

$$V_{\rm ext}(t) = V_{\rm ext}^b \ \exp\left[-(2.5t/T_0)^2\right], \tag{5.9}$$

where $V_{\rm ext}^b$ is given by Eq. (5.7). Starting from $t = 0$, the external potential $V_{\rm ext}^b$ is progressively removed and becomes nearly zero at $T_0 = 7.5$ fs. For $t > T_0$ the dynamics of the density is driven by the time-dependent Hartree and exchange-correlation potentials, where the initial polarisation of the system produces the effect of the V_0 bias applied to the core (see Fig. 5.6 b)). The smooth in time switching off function given by the $\exp\left[-(2.5t/T_0)^2\right]$ is needed in order to avoid excitation of the electron density oscillations in the system. In Fig. 5.7 a) and b) we show the time evolution of the effective bias $U_{\rm eff}(t)$ and tunneling current density $J(t)$ through the middle of the $S = 6.4$ Å wide gap for the (41.3 Å, 47.7 Å, 61 Å) NM. The *effective bias* $U_{\rm eff}(t)$ is a function of time and it is defined as the difference between the one-electron potentials at the middle of the shell and at the center of the core, respectively. It is in general *different* from the *targeted bias* V_0 imposed in the static DFT calculations. The positive current corresponds to the electron transfer from the shell to the core.

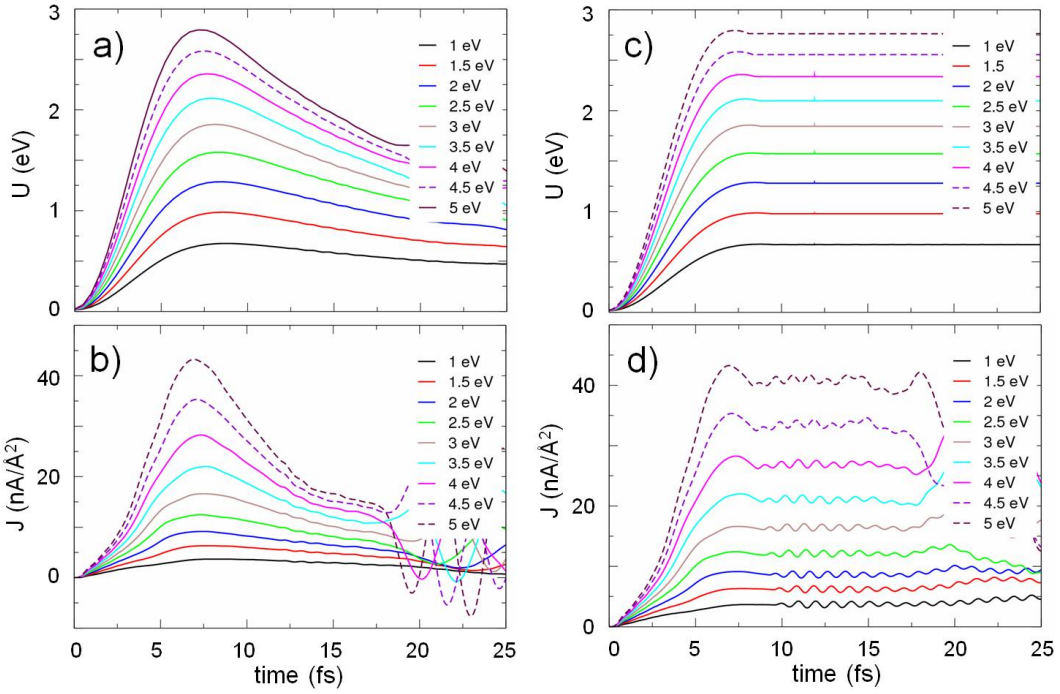

FIGURE 5.7: TDDFT calculations for the electron dynamics of the (41.3 Å, 47.7 Å, 61 Å) cylindrical NM. Progressive removal of the external potential $V^b_{\rm ext}$ triggers the time evolution of the effective bias $U_{\rm eff}(t)$ [panels a) and c)], and density $J(t)$ of the tunneling current through the middle of the core-shell gap [panels b) and d)]. Results are shown for different amplitude of the targeted bias V_0 as explained in the inserts. Panels a) and b) show the calculations where no stabilization of the effective bias has been used. Panels c) and d) correspond to the stabilized case (further details are given in the text).

At $t = T_0$ the $V^b_{\rm ext} \approx 0$, and both $U_{\rm eff}(t)$ and $J(t)$ reach maximum. Observe that the effective bias $U_{\rm eff}(T_0)$ is lower than V_0. This is because within the time interval $0 \leq t \leq T_0$ the initial charge separation between the core and the shell has been partially neutralized by the tunneling current through the gap. At larger times the polarisation of the system is further reduced because of the tunneling current, and $U_{\rm eff}(t)$ decreases reflecting equilibration of the Fermi levels of the core and the shell. The latter, in turn, leads to the reduction of $J(t)$. Considering that in the polarised system the charge of the core is $Q(t)$, the potential difference between the core and the shell is given by $\Delta\Phi = 2Q \ln[R_2/R_1]$. Since the current $I(t) = -dQ(t)/dt$ we can write:

$$\frac{dU_{\rm eff}}{dt} \approx \frac{d\Delta\Phi}{dt} = -2\pi \, \frac{R_1 + R_2}{2} J(t) \ln[R_2/R_1] \, . \tag{5.10}$$

The current in its turn depends on the applied bias via $J = GU_{\rm eff}$, where $G = dJ/dU$ is the conductance of the junction. The low bias conductance G is independent of U, and

the linear dependence of J (and of I) on U_{eff} leads to the solution of Eq. (5.10) given by exponential decay of the initial polarisation.

For the effective bias values below 1 eV the tunneling current is low, and the charge separation between the core and the shell can be maintained for a relatively long time. Therefore, we obtain quasi steady-state situation with nearly constant tunneling current over large time interval ($\sim$ 10 - 15 fs). For the higher V_0 (and U_{eff}) the tunneling current is strongly increased. Because of the large tunneling current the polarization of the system appreciably varies with time for $t > T_0$ and so does the tunneling current. No steady state regime is reached and the calculation of the optical response becomes not an easy task in this case. Additionally, the current density $J(t)$ features an oscillating structure at large times as seen in Fig. 5.7 b). It can be attributed to the excitation of the collective plasmon modes due to the finite spectral width of the switching function.

Despite the difficulty to reach the steady state, we nonetheless have applied impulsive perturbation at $t = T_0$, and the frequency ω-dependent optical absorption cross section $\sigma(\omega)$ has been obtained as is the standard ground state TDDFT calculations. These results can be tentatively interpreted as corresponding to some average value of the bias within the $T_0 \leq t \lesssim T_0 + 15$ fs time interval determining convergence of the time-to-frequency Fourier transform.

To reach, at least transitory, the steady current even at relatively high bias we have performed the calculations where an effective bias $U_{\text{eff}}(t)$ is stabilized at constant level U for $t > T_0$. This is achieved by adding the correcting potential of the form given by Eq. (5.7) with an amplitude calculated dynamically so that $U_{\text{eff}}(t) = U_{\text{eff}}(T_0) \equiv U,\ t > T_0$. In Fig. 5.7 c) and d) we show the corresponding results for the effective bias and current, respectively. With the present choice of the parameters of the system, for V_0 below 4 eV ($U_{\text{eff}}(t)$ below $\sim$2.5 eV) the quasi steady-state is reached within the time interval $T_0 \leq t \lesssim T_0 + 15$ fs allowing calculation of the optical properties $\sigma(\omega)$ with impulsive perturbation. The relation between the targeted bias V_0 and the effectively reached steady state bias U can be deduced from Fig. 5.7 c), where approximate relation $U \sim V_0/2$ holds in overall. The steady state is transitory because at large times too much of the charge is transferred between the core and the shell so that the artificial potential correction becomes too large leading to unphysical variations of the current.

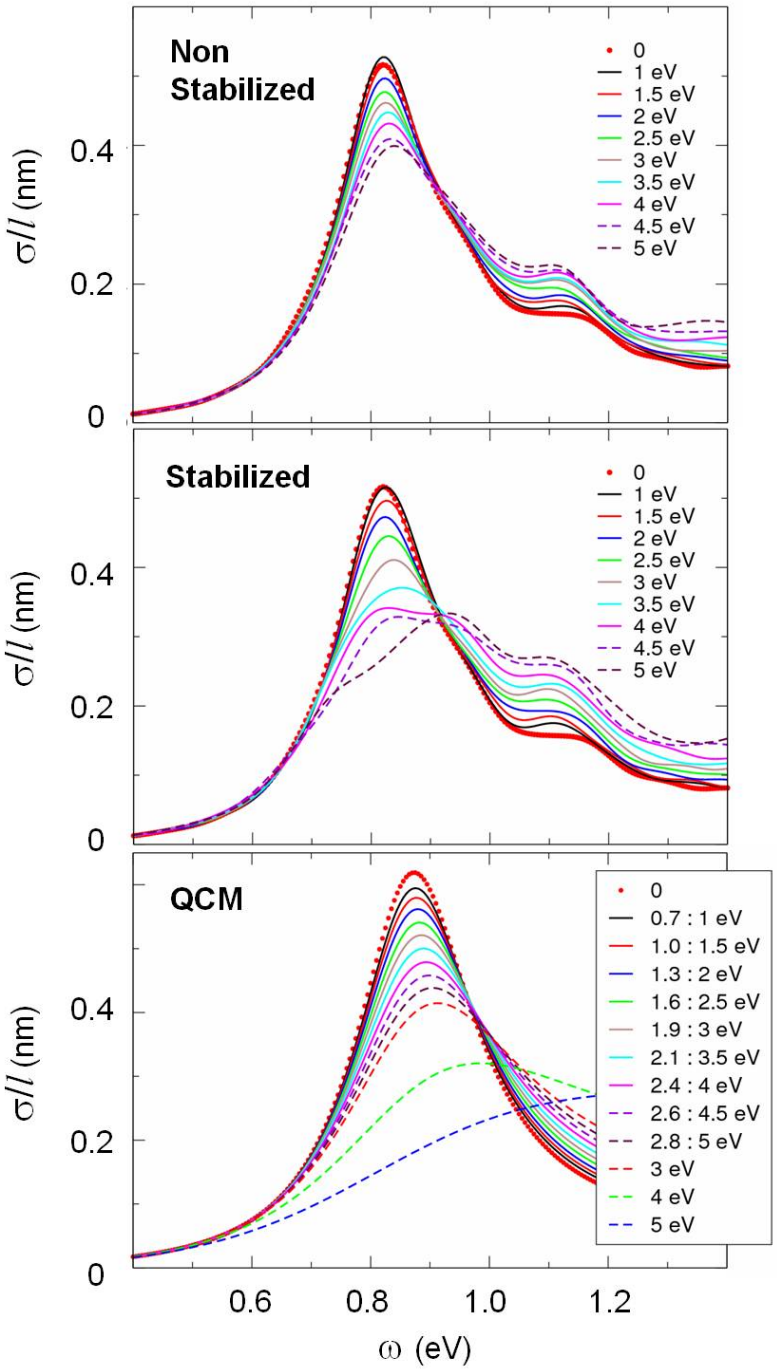

FIGURE 5.8: Absorption cross section per unit length of the (41.3 Å, 47.7 Å, 61 Å) cylindrical NM obtained from the TDDFT calculations with (Stabilized) and without (Non Stabilized) stabilization of the tunneling current and effective bias. We also show results of the classical electromagnetic calculations where the tunneling is accounted for with quantum corrected model QCM. Red dots are used in all panels to trace the reference result corresponding to the ground state system without any external potential. Colors are used to distinguish results obtained at different amplitude V_0 of the polarising potential (targeted bias). The relation between an effective stabilized bias U (first column) and the targeted bias V_0 (second column) is given in the inset of the panel with QCM results.

5.4. Control with applied bias.

In Fig. 5.8 we show the absorption spectra calculated with TDDFT for the (41.3 Å, 47.7 Å, 61 Å) cylindrical NM with the width of the core-shell gap reduced to $S = 6.4$ Å. The incident plane wave is polarized perpendicular to the symmetry axis of the cylindrical NM. Red dots show the reference result: absorption cross section of the ground state system without an applied bias. The frequency range covered by the data corresponds to the lowest energy bonding hybridized plasmon resonance ω_-^- which is most sensitive to the variations of the tunneling barrier. Different curves are labelled according to the targeted bias V_0. Indeed, for the non stabilized case the effective bias between the core and the shell varies upon $\sigma(\omega)$ calculation and thus it is ill-defined. The insert of the lowest panel of the figure showing the results obtained with quantum corrected model (discussed below) allows to connect V_0 and the bias U for which the $\sigma(\omega)$ is obtained in the stabilized TDDFT calculations.

As a main result of this thesis, the applied bias leads to the broadening of the plasmon resonance in absorption cross section, and to the reduction of the resonant absorption (see Fig. 5.8). The plasmon mode slightly blue shifts with increasing bias. These results can be explained as due to the bias induced reduction of the tunneling barrier so that the tunneling current increases and thus (i) resistive losses to the electron hole excitations are larger; (ii) capacitive coupling between the core and the shell is reduced because of the partial neutralisation of the plasmon-induced screening charges across the gap. These qualitative trends are robust and present in both (stabilized and non stabilized) TDDFT data showing 30-35 % variation of the maximum absorption for only some eV bias change. The variation is somewhat larger in the stabilised case. This is because, for the same initial V_0, it corresponds in average to the larger effective bias and so to the larger conductivity of the junction for $t > T_0$ time interval relevant for the calculation of $\sigma(\omega)$ (see Fig. 5.7).

To gain insight into the main physics underlying the TDDFT results let us consider a canonical system formed by a junction between two flat metal surfaces separated by a narrow gap of width S. We can use a quantum many-body approach developed for electron dynamics in metal-isulator-metal tunnel junctions in the presence of electromagnetic fields to describe linear and non-linear effects such as rectification[200]. Within the linear response, the presence in the junction of the optical field E_ω at frequency ω,

triggers a tunneling current at the same frequency. The amplitude of the dissipative component (in phase with the driving field) of this ac current density is given by:

$$J_\omega(U, V_\omega) = \frac{V_\omega}{2\omega} \left[J_{\rm dc}(U+\omega) - J_{\rm dc}(U-\omega) \right], \tag{5.11}$$

where U is the applied dc bias, $V_\omega \simeq SE_\omega$ is the optical bias in the junction, and $J_{\rm dc}(U \pm \omega)$ is the dc current at bias $U \pm \omega$. For slow variation of $J_{\rm dc}$ with U, we obtain the classical limit

$$J_\omega(U, V_\omega) = S \, \frac{dJ_{\rm dc}(U)}{dU} \, E_\omega, \tag{5.12}$$

which can be deduced by developing $J\left(U + SE_\omega \cos(\omega t)\right)$ in the Taylor series for $SE_\omega \ll U$. An increase of the applied bias leads to a lower tunneling barrier, thus the conductivity $\sigma(U, S) = S \; dJ_{\rm dc}/dU$ becomes larger resulting in a larger tunneling current at optical frequency J_ω. In the cases, where an increase of the tunneling current has been caused by the progressive reduction of the gap width S (with no applied bias), it was responsible for the attenuation of the gap plasmon resonance[38, 39, 42]. In the situation like here where a bias is applied (with fixed gap separation), the increasing tunneling current equally leads to a smaller absorption cross section at the plasmon gap resonance. The screening charges at the opposite sides of the junction are partially neutralised and the resonance is broadened as a result of the increased resistive losses. It is worth to mention that for larger gap size S, the tunneling probability decreases so that larger applied bias U is needed to reach the same tunneling current, and thus a similar degree of plasmon response modification.

5.5. Quantum corrected model. QCM.

To further verify the validity of the concept of bias-assisted tunneling at optical frequencies, we have also calculated the optical response of the cylindrical NM using the quantum corrected model (QCM)[1]. The permittivity of the Na core and Na shell is described with Drude model given by Eq. (1.2) with parameters adjusted to the TDDFT result for individual nanowire (nanosphere). The tunneling gap is described using a local effective dielectric function

$$\varepsilon_g(\mathrm{U}, S) = 1 + i\frac{4\pi\sigma_g(U, S)}{\omega}, \tag{5.13}$$

which includes the effect of the conductivity across the gap at optical frequencies, in such a way that the "quantum" relationship between the tunneling current and the optical field in the gap is correctly reproduced. The constant size of the gap S in this case allows to use the TDDFT results to define the parameters of the effective medium in the presence of the bias. To this end, within the simple approach widely applied to describe the optical rectification and frequency mixing in tunneling junctions, the total current density through the junction reads[89, 200]:

$$J_{\rm tot} = J_{\rm dc}(U,S) + J_{\rm opt} = J_{\rm dc}(U,S) + \frac{dJ_{\rm dc}(U,S)}{dU}\, U_{\rm opt}(\omega)\, e^{-i\omega t}. \tag{5.14}$$

Here $J_{\rm dc}(U,S)$ is the dc current due to applied bias U, $U_{\rm opt}(\omega)\, e^{-i\omega t}$ is the optical bias induced by electromagnetic field in the junction. The quantity $G(U,S) = \frac{dJ_{\rm dc}(U,S)}{dU}$ is the dc conductance of the junction. Since for the QCM model one is interested in the conductivity of the gap σ_g we recast Eq. (5.14) in the form:

$$J_{\rm tot} = J_{\rm dc}(U,S) + J_{\rm opt} = J_{\rm dc}(U,S) + \frac{dJ_{\rm dc}(U,S)}{dU}\frac{dU}{dE}\, E_{\rm opt}(\omega)\, e^{-i\omega t}, \tag{5.15}$$

where $E = U/S$ is the radial component of the dc field in the gap because of the applied bias U, and $E_{\rm opt}(\omega)$ is the optical field in the gap. The quantity

$$\sigma_g(U,S) = S\, \frac{dJ_{\rm dc}(U,S)}{dU}, \tag{5.16}$$

is then the sought conductivity of the gap.

The current-voltage characteristic of the junction is presented in Fig. 5.9 for the (41.3 Å, 47.7 Å, 61 Å) cylindrical NM discussed in the text. $J(U,S)$ is obtained from the stabilized current and effective bias values reported in panels c) and d) of Fig. 5.7. The red curve shows an analytical fit to the TDDFT data. It is given by the equation $J(U,S) = 0.00332U\ e^{0.548\ U}$, where U is measured in eV and current density in nA/Å^2. The analytical fit greatly simplifies calculation of the differential conductance of the junction dJ/dU, and extrapolation to large U - values, where the TDDFT calculations are not available.

The QCM results obtained with parametrisation of the tunneling gap as described above and with no further parameter adjustment are shown in the lowest panel of Fig. 5.8. The good quantitative agreement of plasmon peaks intensity and broadening when compared

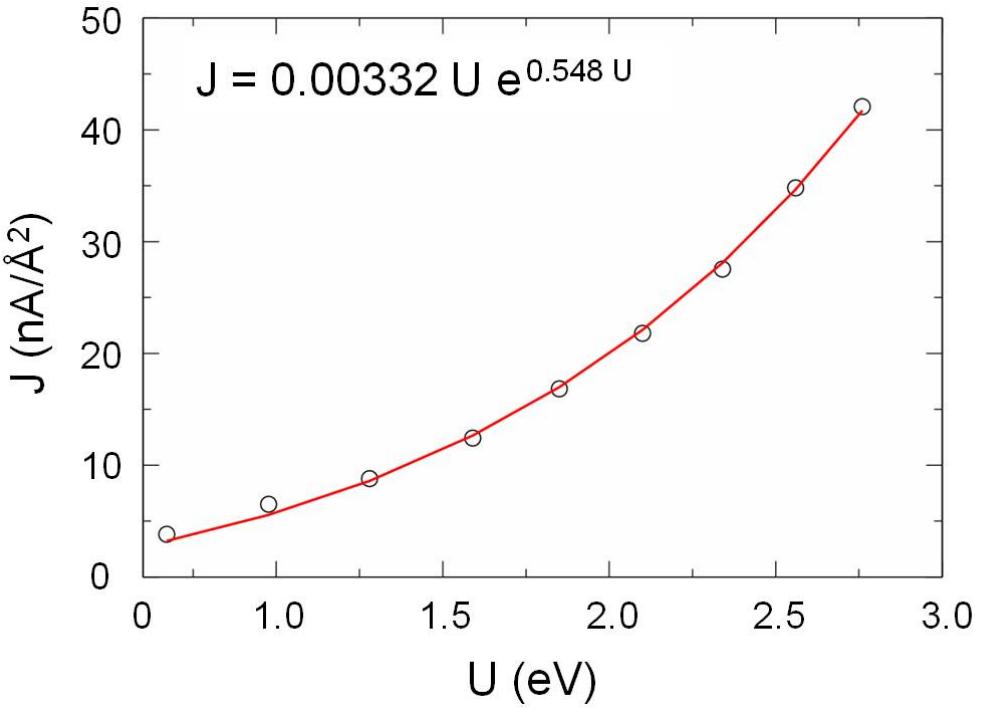

FIGURE 5.9: Dependence of the tunneling current density on the applied bias for the (41.3 Å, 47.7 Å, 61 Å) cylindrical NM. Dots stand for the TDDFT data obtained from panels c) and d) of Fig 5.7, and solid line is an analytical fit with equation indicated in the insert.

with the TDDFT results indicates that the bias-induced variation of the conductivity across the junction is at the origin of the change of the absorption cross section. Indeed, applied bias can produce various changes in the system which might lead to the modification of the plasmon modes: (i) Change of the potential well ensuring the electron confinement; (ii) Change of the non-local screening because of the change of electron density at facing surfaces across the gap; (iii) Change of the tunneling barrier and thus of the tunneling current across the junction. The QCM accounts only for the last effect, and it appears sufficient to describe the TDDFT data.

Using QCM we could also calculate absorption spectra for the bias U as high as 3, 4, and 5 eV which is *technically impossible with present full quantum TDDFT approach*. The tunneling current between the core and the shell is too strong in this case leading to the fast charge equilibration in the system so that no steady state can be reached. The QCM results in lowest panel of Fig. 5.8 predict quenching of the plasmon resonance for the applied bias above 4 eV.

5.6. Time dependence of the induced dipole

The difficulty to obtain the steady state regime for the extraction of the absorption spectra calls for consistency checks in order to provide further support for the interpretation of the TDDFT results. Broadening of the plasmon resonance in optical response with increasing bias indicates an increased plasmon coupling to the electron-hole binary excitations because of the larger tunneling probability. In terms of electrical engineering, the higher barrier conductivity leads to larger resistive losses[200–202]. The broadening of the resonance peak in the frequency domain corresponds, in the time domain, to faster coherence loss and decay of the plasmon mode. To illustrate the dynamics of the plasmon resonance we show in Fig. 5.10 a) the time evolution of the induced dipole excited in the (41.3 Å, 47.7 Å, 61 Å) cylindrical NM by the incident infra-red pulse. The NM is initially in the ground state. No bias is applied. The incident pulse is polarised perpendicular to the symmetry axis and its electric field is given by:

$$E_{\mathrm{IR}}(t) = E_0 \ \cos(\omega_{\mathrm{IR}}) \ \exp\left[-\left(\frac{t-3T_{\mathrm{IR}}}{T_{\mathrm{IR}}}\right)^2\right], \tag{5.17}$$

with $\omega_{\mathrm{IR}} = 0.82$ eV at resonance with bonding hybridized plasmon ω_-^- of the NM, and duration of the pulse $2T_{\mathrm{IR}} = 20$ fs. The $E_{\mathrm{IR}}(t)$ is shown with red dashed line in Fig. 5.10 a). Essentially, the incident field excites the plasmon mode and the corresponding density oscillation persist long time after the termination of the incident pulse. This is illustrated with black line showing result obtained for the isolated NM in vacuum in absence of the applied bias. One can observe slight Rabi oscillations for $t > 80$ fs originating from the interference between plasmon and electron hole excitations[126].

At the time $T_0 = 59$ fs the bias is switched on, i.e. the external potential expressed by Eq. (5.7) with negative V_0 is applied to the system, resulting initially in the effective bias $U = -V_0$ as shown on Fig. 5.10 b). The suddenly applied bias leads to the population and coherence decay of the collective plasmon oscillations as manifested from the comparison with $U = 0$ result (black line) in Fig. 5.10 a). This is fully consistent with broadening and loss of intensity of the ω_-^- resonance in absorption spectra. Because of the electron tunneling and polarisation of the system, the applied field is progressively screened, and the potential energy difference between the core and the shell decays in time. For the highest applied bias the tunneling current is strongest, and $U(t)$ quickly relaxes from initial value of 5 eV to much lower value of $\sim 2.5 - 3$ eV. For these lower values of effective bias the tunneling current is relatively small. The energy alignment of the

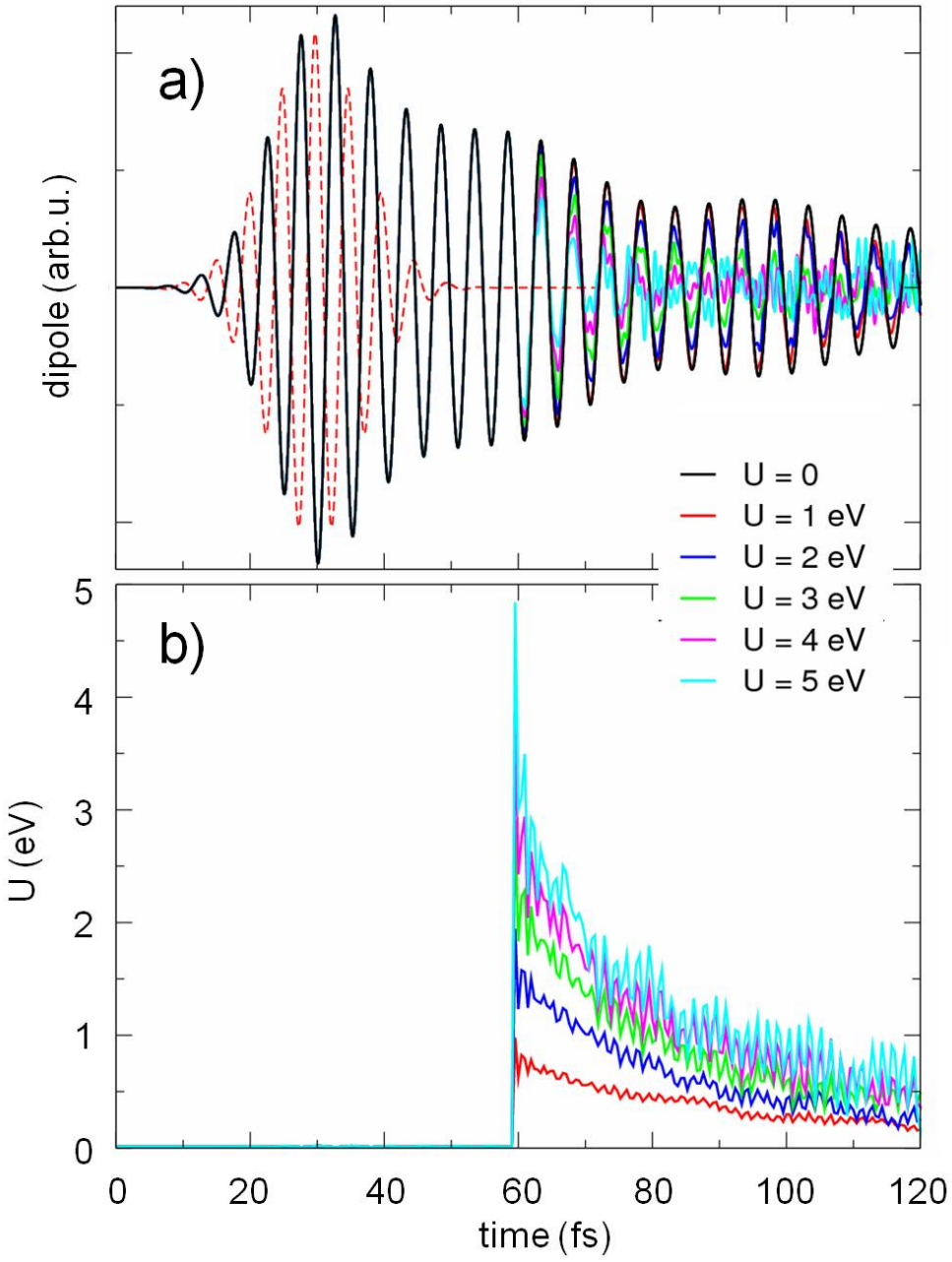

FIGURE 5.10: The time evolution of the induced dipole $P(t)$ [panel a)] and effective bias $U(t)$ [panel b)] calculated with TDDFT for the (41.3 Å, 47.7 Å, 61 Å) cylindrical NM. Initially the non-perturbed ground state system is subjected to the IR pulse resonant with ω_-^- plasmon mode and polarized perpendicular to the NM axis. After the termination of the pulse, at $T_0 = 59$ fs the positive bias U is applied to the core while the shell is grounded. Different curves correspond to the results obtained with different U-values as explained in the insert.

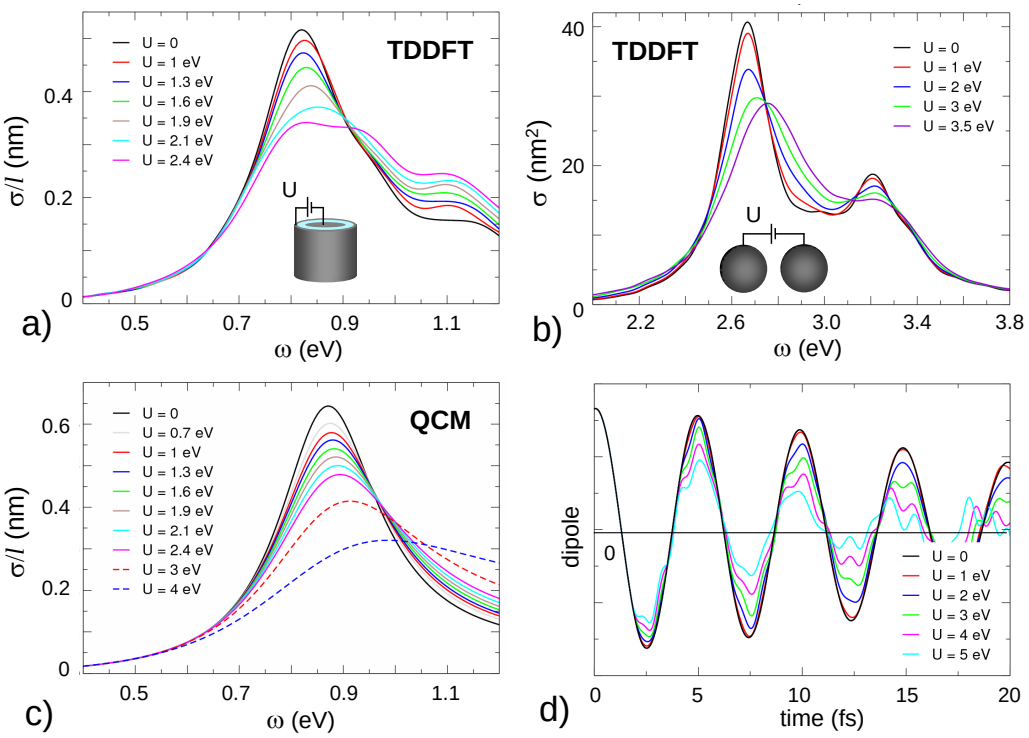

FIGURE 5.11: Effect of an applied bias on the plasmonic modes of the cylindrical NM and the plasmonic dimer. Panels a), b): TDDFT results for the absorption spectra of the (41.3 Å, 47.7 Å, 61 Å) cylindrical NM and of the plasmonic dimer formed by $R = 21.7$ Å spherical nanoparticles separated by a gap of width $S = 6.4$ Å. For the NM, the absorption cross section per unit length, σ/l, calculated with TDDFT, is compared with the results of the classical calculations within the quantum corrected model (QCM) shown in panel c). Panel d): time evolution of the dipole induced in the NM of panel (a) by an incident pulse of light resonant with ω_-^- plasmon mode, and linearly polarised in the direction perpendicular to the symmetry axis. Long times following the termination of the incident electromagnetic pulse are shown. At $t = 2$ fs the bias is applied to the system. In each panel the calculations have been performed for different values of the applied bias, as detailed in the inserts.

Fermi levels of the core and the shell with exponential decay of $U(t)$ proceeds on longer time scales. Oscillating structure of the $U(t)$ curve is caused by the excitations in the system produced by the sudden change of the potential at $t = T_0$. In particular, the higher energy ω_-^+ plasmon mode with core character[4] is excited.

5.7. Summary of main results and conclusions

In order to get a crystal clear idea of the proposed active control strategy with an applied bias we summarize in Fig. 5.11 the main results obtained in this chapter. In Fig. 5.11(a)

we show the absorption spectra calculated with TDDFT for a cylindrical NM with the width of the core-shell gap of $S = 6.4$ Å. The incident plane wave is polarized perpendicular to the symmetry axis of the cylindrical NM. For the sake of completeness we show in Fig. 5.11(b) results obtained by the Orsay team (D.C. Marinica and A. G. Borisov) for the absorption spectra for a spherical plasmonic dimer with the same gap width ($S = 6.4$ Å). The incident plane wave is polarized along the symmetry axis of the dimer. The calculations have been performed for different values of the stabilised bias U applied between the core and the shell of the cylindrical NM or between the nanoparticles forming the dimer as depicted in the insets of Fig. 5.11(a) and (b).

- When the bias across the gap is applied, a considerable decrease of the resonance absorption peak is produced for both geometries. This is the central result of this chapter. Within the studied U range $0 < U < 3$ eV we calculate ∼30 % variation of the maximum of the absorption cross section primarily because of the broadening of the plasmonic resonance. Thus, even a moderate change of the DC bias applied allows to appreciably modify the intensity of the plasmon response.
- The TDDFT results are retrieved with classical electromagnetic calculations using QCM as shown in Fig. 5.11(c) for cylindrical NM. Since tunneling is the only effect accounted for in QCM, good agreement between the TDDFT and QCM results indicate that this is indeed the main physical mechanism behind the bias induced change in plasmon responce. At high applied bias, where the TDDFT calculations can not be performed, the QCM predicts the quenching of the ω_{-}^{-} resonance for U above 4 eV.
- For the bonding dipole resonance of the spherical dimer as shown in Fig. 5.11(b), the peak in absorption cross section notably blue shifts with increasing U. This result is consistent with the reduction of the capacitive coupling across the gap because of the neutralization of the plasmon induced screening charges as has been discussed in the case of molecular shunted junctions[159].

The dependence of the absorption cross section on the applied bias opens the path to controllable modification of the plasmon dynamics in the system. This is illustrated in Fig. 5.11(d) where we show the time evolution of the dipole induced in the core shell cylindrical gap by the external Gaussian electromagnetic pulse resonant with the gap plasmon mode. After the termination of the pulse, the time evolution of the induced

dipole is given by the decaying oscillations at the plasmon frequency ω_{-}^{-}, as shown with a black line in the figure for the case in the absence of bias. We compare this reference result with the calculations of the response when the bias between the core and the shell has been switched "on" at $t = 2$ fs. The larger the applied bias is, the faster the decay and dephasing of the collective plasmon oscillation in the system due to the increase of the electron tunneling. This result, monitored in the time domain, is equivalent to the broadening of the absorption cross section when the bias is applied, observed in the frequency domain response of panels (a), (b), and (c) of Fig. 5.11.

In conclusion, we have proposed a novel strategy for active control of junction plasmon resonances based on the application of a bias across the gap. The physical origin of the effect is a bias-induced change of the electron tunneling barrier which in turn controls the conductive coupling between the two nanostructures. The feasibility of the approach has been demonstrated with proof-of-principle calculations based on the quantum mechanical time-dependent density functional theory. While we here considered vacuum gaps, filling the plasmonic gap with dielectric materials such as oxides will also modify the tunneling barrier. This effect may be useful in practical realizations of the proposed device since it introduces additional tuning modalities. Thus, the lowering of the tunneling barrier offers the possibility to reach the sought control for broader gaps. Further extensions of this concept may include molecular linkers with conductance windows allowing for 'on'/'off' switch functionalities.

Quantum active control of plasmons, as demonstrated here, is inherently a fast (ps) process allowing operation at the time scales of modern electronics, reversible, and progressive tuning of the plasmon resonances. This opens appealing perspectives for the development of tunable absorbers for solar energy harvesting, control of the information transfer in plasmonic waveguides, and manipulation of plasmon-exciton couplings. Our concept of electrical control of light in metallic nanostructures thus provides a new platform for many practical applications in photonics and optoelectronics.

Chapter 6

Quantum Plasmonics and charged clusters dynamics

In this chapter, using the TDDFT we performed full quantum calculations of the optical response of the charged spherical clusters. We have obtained that, because the system stays neutral in the bulk, and the extra-charge is localized at the surface of the cluster, the dipolar plasmon mode displays only small frequency shift linked with change of the electron spill-out from the nanoparticle boundaries [7]. For the negatively charged clusters, we have also addressed the issue of the decay of the negative charge via resonant electron transfer from the cluster orbitals into the continuum of propagating states above vacuum level. Indeed, even small (relative to the total number of electrons in the system) negative charge raises the Fermi level of the cluster above the vacuum level and renders the system unstable. The excess of the electron population decays with characteristic time constants that can be fully understood using an analytical study based on the WKB method, similar to the studies of the alpha-decay. Our results on the charged clusters allow to critically reinterpret the experimental data obtained with electrochemistry, where the shift of the plasmon resonances has been attributed to the charging effects. Based on our results, we tentatively propose that the frequency shift of plasmon resonances is related with change of the dielectric environment in vicinity of the cluster.

6.1. Introduction

As we have already discussed in the introductory part of Chapter. 5, there is a continuous effort in the plasmonic community to achieve a control of the optical response of the nanostructures not only via the proper design of these nanostructures [203, 204], but actively. For example, by electrically driving liquid crystals containing plasmonic particles [205]. The modulation of the frequencies of plasmon resonances has been also achieved in electrochemistry appliying bias between the nanoparticles and electrolyte or by adding chemical reductants to a colloidal nanoparticle solution [179, 180, 206–210].

In some cases the plasmon wavelength shift of 10 nm per eV of applied potential has been reported [211]. By analogy with 2D planar systems such as graphene [53, 178, 212–214] it is very tempting to explain the observed shift of the plasmon frequency as a result of the charge doping of the nanoparticles [206]. Indeed, since the bulk plasmon frequency is given by $\omega_p = \sqrt{\frac{ne^2}{\varepsilon_0 m}}$, and e.g. dipolar plasmon resonance for the spherical nanoparticle is at frequency $\omega_{\mathrm{DP}} = \omega_p/\sqrt{3}$ one would expect that the change in the conduction electron density Δn would automatically lead to the frequency shift of the localised plasmon resonance with $\Delta\omega_p/\omega_p \sim \Delta n/n$. However, the situation is much more complex than it seems at a first glance. (i) Because of the high density of the conduction electrons in metal Δn should be also large which implies strong charging of the system resulting in high electrostatic potentials [178]. (ii) The negative charge Q of the cluster of radius R leads to the electrostatic potential $|Q|/R$ acting on the electrons in the cluster, so that the Fermi energy E_F of the system is rased by the same amount, which can lead to the electron loss into the continuum of propagating states above vacuum level for $|Q|/R > \Phi$, where Φ is the work function of the nanostructure. (iii) In difference to the 2D planar structures, in virtue of Gauss theorem, in the 3D metallic objects the volume stays neutral. The screening charges reside at the surface within the narrow layer of the width given by the screening length r_s (Wigner-Zeitz radius of the metal). It is not obvious that such a narrow layer of surface charge might lead to the"expected" shift the plasmon frequency.

The main goal of this chapter is to study the electron dynamics and plasmon modes of small charged metallic clusters, where using the TDDFT calculations allows to reveal the role of different effects discussed above in the optical response of these nanostructures. Below we describe spherical sodium and silver clusters with sizes $\sim$ 2 nm as has been

used in this study, and present the ground state properties of these neutral and charged systems as obtained in the density functional theory calculations (DFT). The static DFT results provide an input for the TDDFT study of the electron dynamics and optical response as function of the cluster charge. As well we use TDDFT to address the electron losses for the negatively charged clusters. Finally, we conclude underlying the consequences that our results can have for the interpretation of the electrochemical experiments.

6.2. Model and computational aspects

The sodium and silver spherical nanoparticles studied here are described using jellium metal (JM) approximation, where the positive ion cores are not treated explicitly, but represented with uniform positive background charge of the density $n_+ = (4\pi r_s^3/3)^{-1}$. The Wigner-Seitz radius (or the screening length of the free electron gas) r_s equals to 4 a_0 for sodium, and 3.02 a_0 for silver[1]. In the ground state (neutral system) both clusters have a closed shell structure and contain 2018 valence electrons, so that the positive background charge is also $Q_+ = 2018$ which results in the cluster radius $R = 50.6$ a_0 (2.67 nm) for sodium, and $R = 38.2$ a_0 (2.06 nm) for silver. Despite its simplicity, the JM correctly captures the collective plasmon modes of conduction electrons, and it has demonstrated a good predictive power in the description of quantum effects in individual nanoparticles and in narrow gaps [54, 55, 122]. For sodium, which is the prototype of the free electron metal, the JM performs particularly well in the description of the interaction of the optical pulse with nanosized objects. For silver, the contribution of the localized d-electrons to the screening has to be taken into account in order to correctly reproduce frequencies of the localised plasmon mode(s) [127, 128]. This is achieved via the introduction of a polarizable background [38] characterised by the non-dispersive dielectric constant $\varepsilon_\infty = 4.58$. For the neutral sodium cluster we calculate the work function $\Phi_{Na} = 3$ eV in good agreement with earlier studies on such systems [215–217]. For the silver cluster, in order to reproduce the experimentally measured work function of silver $\Phi_{Ag} = 4.65$ eV [218], an additional attractive potential of 3 eV is imposed inside cluster (the so-called stabilized jellium model [219]).

Prior to the TDDFT studies of the electron dynamics in the neutral and charged clusters, their ground state properties have been determined with static density functional theory DFT calculations. The Kohn-Sham scheme of the DFT is used [220], where

[1] the Bohr radius $a_0 = 0.053$ nm

the electron density is given by that of the non-interacting system $n(\vec{r}) = \sum_j |\psi_j(\vec{r})|^2$. The summation runs over all occupied Kohn-Sham orbitals $\psi_j(\vec{r})$, and $\psi_j(\vec{r})$ obey the stationary Schrödinger equations

$$\left(\mathbb{T} + V_{\rm xc}(\vec{r}; n) + V_{\rm H}(\vec{r}; n) + V_{\rm st}(\vec{r})\right) \psi_j(\vec{r}) = E_j \psi_j(\vec{r}). \tag{6.1}$$

In Eq. (6.1), $\mathbb{T}$ is the kinetic energy operator, $V_{\rm xc}(\vec{r}; n)$ is the exchange-correlation potential derived within the local density (LDA) from the exchange-correlation functional of Gunnarson and Lundqvist [130], and $V_{\rm H}(\vec{r}; n)$ is the Hartree potential calculated from the charge density $N_+ - n$. The exchange-correlation and Hartree potentials are equivalent to those introduced in the context of the TDDFT with only difference that the time-dependence is absent in the static calculations. Finally, $V_{\rm st}(\vec{r})$ is the stabilizing potential used only in case of Ag clusters.

6.3. Ground state properties

In Fig. 6.1 we show the ground state electronic density calculated with DFT for the charged Na and Ag clusters. Results are presented for different values of the cluster charge Q. Within the range of the cluster charges considered here, with exception of the largest positive cluster charge $Q = +20$, the valence electron density is not strongly affected by the charging. Generally it is close to 1 (in units of the background positive charge density n_+), and features Friedel oscillations because of the reflection of the electron wave at nanoparticle boundaries. One also clearly observes the spill out of the electron density outside cluster boundaries with spatial extension of this effect slightly larger for Na because of the lower work function and smaller electron confinement in the potential well of the nanoparticle.

To reveal the actual location of the extra charges we analyse in Fig. 6.2 the change of the ground-state electron density $\Delta n(r) = n_Q(r) - n_0(r)$ induced by the charge Q added to the cluster. Here $n_Q(r)$ is the electron density of the cluster with charge $Q(r)$, $n_0(r)$ is the ground state electron density, and r is the radial coordinate. As particularly obvious from panels e) and f) of this figure, the extra charge added to the cluster resides mainly in the surface layer of the width given by the screening radius r_s. Indeed, the charge inside the sphere of radius r is given by $\int_0^r 4\pi r'^2 \Delta n(r') dr'$. It is almost zero for

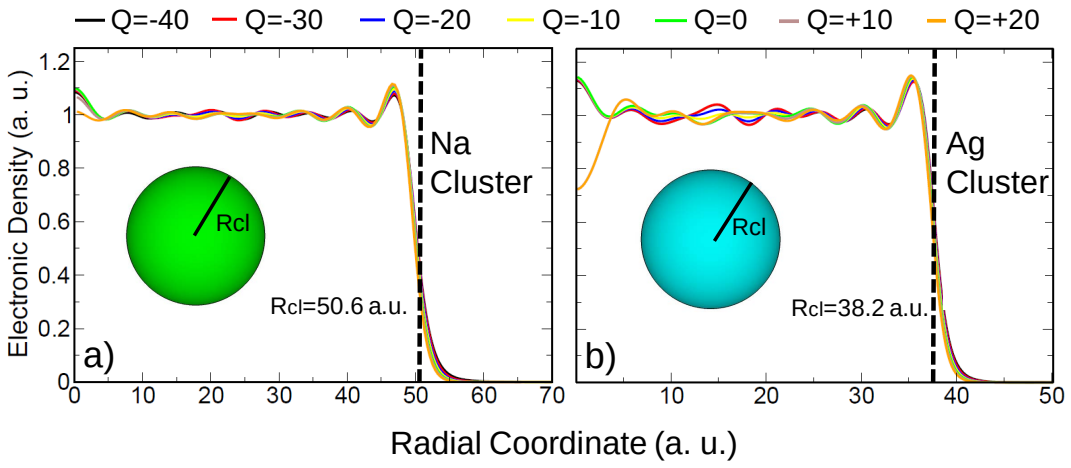

FIGURE 6.1: DFT results for the ground state electronic density of the neutral and charged metallic clusters. The density (in units of the positive background charge density n_+ is shown as function of the radial coordinate measured from the center of the cluster. Panel a) shows the results for sodium and panel b) for silver. The dashed vertical line, indicates the cluster edge ($R_{cl}^{Na} = 50.6$a.u.$= 2.67$nm and $R_{cl}^{Ag} = 38.9$a.u.$=$ 2.06nm). Different colors are used to distinguish results obtained for different charge of the clusters as explained at the top of each panel.

$r < R_c$, and it quickly reaches the nominal value of Q for $r \simeq R_c + r_s$. This result can be easily understood from the Gauss theorem in electrostatics. The excess charge in some volume area of the cluster would lead to the electric fields through the surface enclosing this volume area. In response to electric fields the conduction electrons which are quasi-free inside the cluster, will move until the fields are screened, or equivalently the excess charge is compensated. Thus, aside from the possible finite size effects the electron density in the bulk stays largely unaffected by charging of the cluster and all the excess charge is accumulated in the thin surface layer.

A charge Q located at the surface of the cluster of radius R_c, creates for the electrons inside the cluster an additional constant potential $V = -Q/R_c$. Thus adding 20 electrons to the Ag cluster already containing 2018 electrons (1 % change in the total number of electrons), leads to the 14 eV potential for the electrons at the cluster surface. The electrons outside the cluster and located at a radial distance r from its center experience the $-Q/r$ Coulomb potential. Based on these simple considerations we can make an

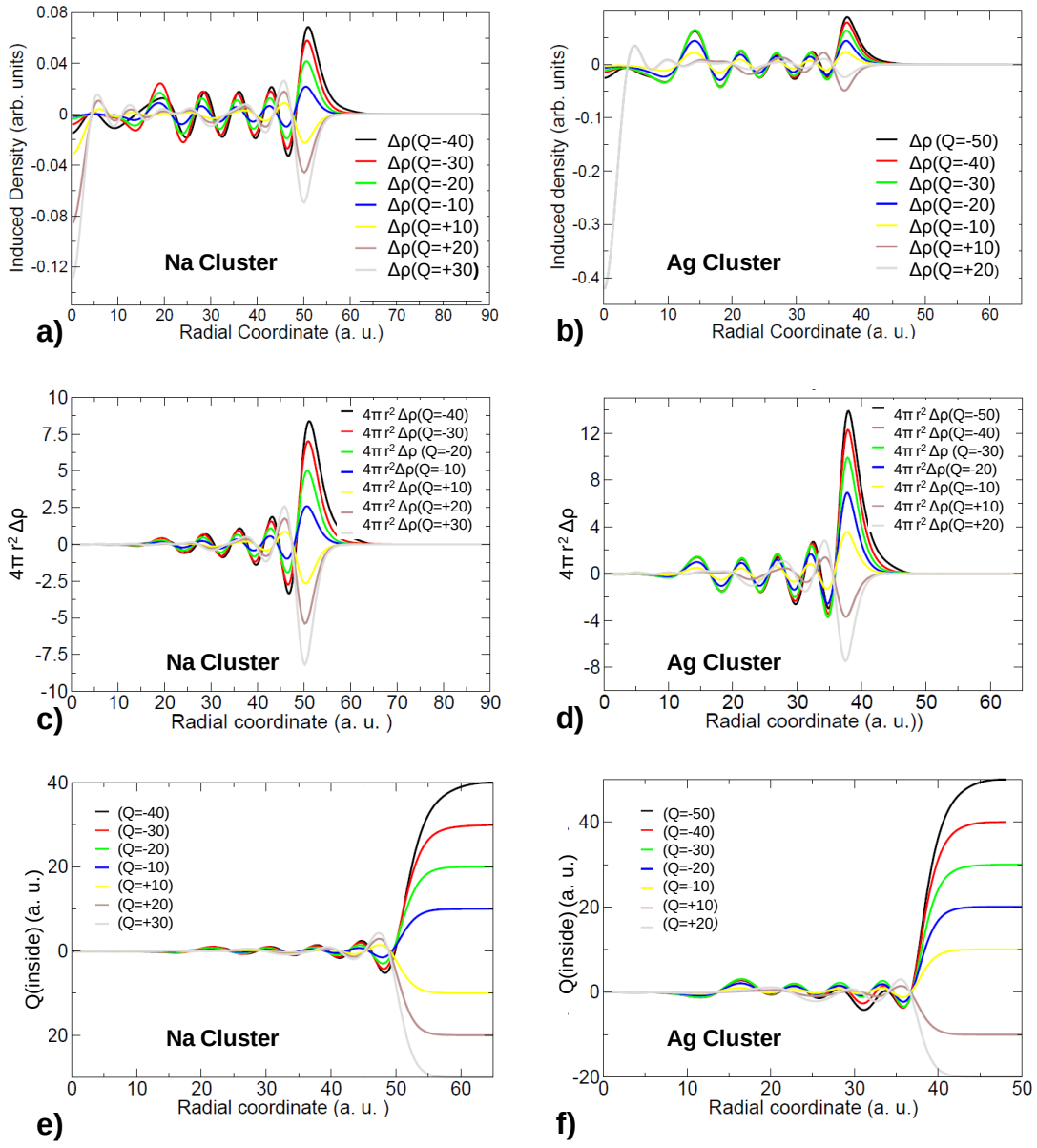

FIGURE 6.2: Induced density as function of the radial coordinate r for different values of the cluster charge as calculated with DFT for sodium [panel a)] and silver [panel b)] clusters. Panels c) and d): the charge induced at the surface of the sphere of radius r: $4\pi r^2 \Delta n(r)$ as a function of the radial coordinate for charged sodium c) and silver d) clusters. Panels e) (sodium) and f) (silver): the charge inside the sphere of radius r: $\int_0^r 4\pi r'^2 \Delta n(r') dr'$ as function of r.

estimate for the Fermi energy E_F of the charged cluster as:

$$E_F^Q = -\Phi - Q/R_c, \tag{6.2}$$

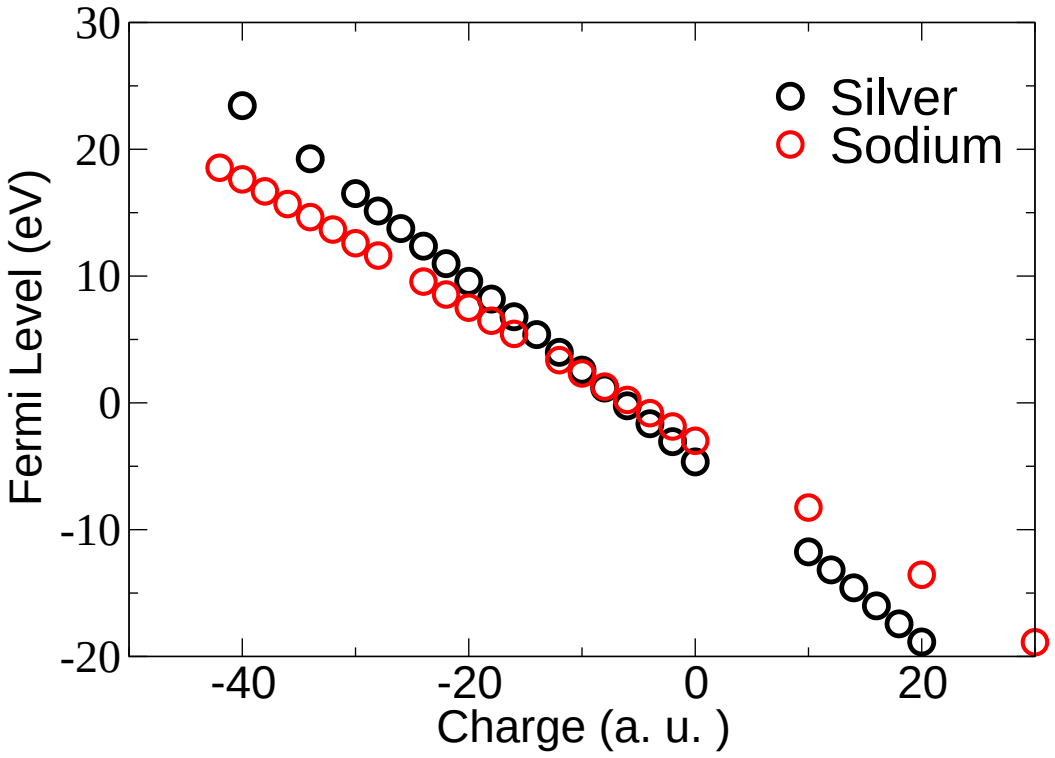

FIGURE 6.3: Energy of the Fermi level E_F (eV) as function of the cluster charge. The DFT ground state calculations have been performed for Na (red circles) and Ag (black circles) clusters a explained in the text. Straight lines of the corresponding color show analytical dependence given by Eq. 6.2.

where Φ is the work function of the *neutral* cluster. Alternatively the work function is given by

$$\Phi^Q = \Phi + Q/R_c, \tag{6.3}$$

i.e. negative charge decreases the work function of the nanoparticle, and, alternatively, the positive charge increases the electron binding. For the affinity level of the singly charged clusters one should rather use $A = -\Phi + 0.5/R_c$ as can be obtained considering the work to add the extra charge -1 to the neutral system [215, 216]. For multicharged clusters considering charge variation $-|Q| \to -|Q| - 1$ this approach leads to Eq. 6.2. To illustrate the effect of the cluster charge on the electron binding we show in Fig. 6.3 the Fermi energies of the clusters of different charge obtained in DFT ground state calculations.

The negatively charged cluster becomes unstable for the critical charge when $E_F^Q \geq 0$, i.e. when $Q < Q_{\rm cr}$ given by

$$Q_{\rm cr} = -\Phi R_c. \tag{6.4}$$

When the number of the extra electrons added to the cluster exceeds $|Q_{\rm cr}|$ (the cluster charge is $Q_{\rm cr} + q$ where $q < 0$), the Fermi level is promoted above the vacuum level. The electronic population of the cluster decays via energy-conserving resonant electron transfer into the continuum of vacuum states through the potential barrier separating two classically allowed regions of motion: inside cluster $r \leq R_c$ and in vacuum $R_{ext} \leq r$ as we show in Fig. 6.4. Assuming that an electron far enough from the charged cluster experiences the Coulomb potential $-Q/r$, and using Eq. 6.2 R_{ext} can be obtained from:

$$E_F^Q = -\Phi - \frac{Q}{R_c} = \frac{-Q}{R_{ext}}, \tag{6.5}$$

so that

$$R_{ext} = \frac{Q}{\Phi + Q/R_c} = \frac{R_c}{1 - \Phi R_c/|Q|}. \tag{6.6}$$

As a result of the population decay, the cluster charge would relax to $Q_{\rm cr}$, where the Fermi level is brought to the vacuum level and the system becomes stable. Taking into account that the number of electrons already present in the cluster N_e is given by $N_e = [R_c/r_s]^3$, the relative change of the charge allowed before the onset of the electron population decay is given by:

$$|Q_{\rm cr}|/N_e = \Phi R_c/\left[R_c/r_s\right]^3, \tag{6.7}$$

so that finally

$$|Q_{\rm cr}|/N_e = \Phi\ r_s^3/R_c^2. \tag{6.8}$$

Thus, the relative number of electrons that can be added to the neutral cluster before the onset of the electron population decay decreases as R_c^2. The larger is the cluster, the less electrons in relative terms it can admit. For the 2018 electron clusters studied here, the $Q_{\rm cr}$ is -5.6 for Na and -6.5 for Ag. This implies that the system becomes unstable when only 6 (7) electrons are added to the Na(Ag) cluster which represents less then 0.4 % variation of the total number of electrons. We note in passing that, for the positively charged clusters, accumulation of the non-screened ions at the cluster surface leads to the so-called Coulomb explosion where the ions are ejected from the crystal lattice sites into the vacuum [221–223]. Description of this process requires to consider the heavy

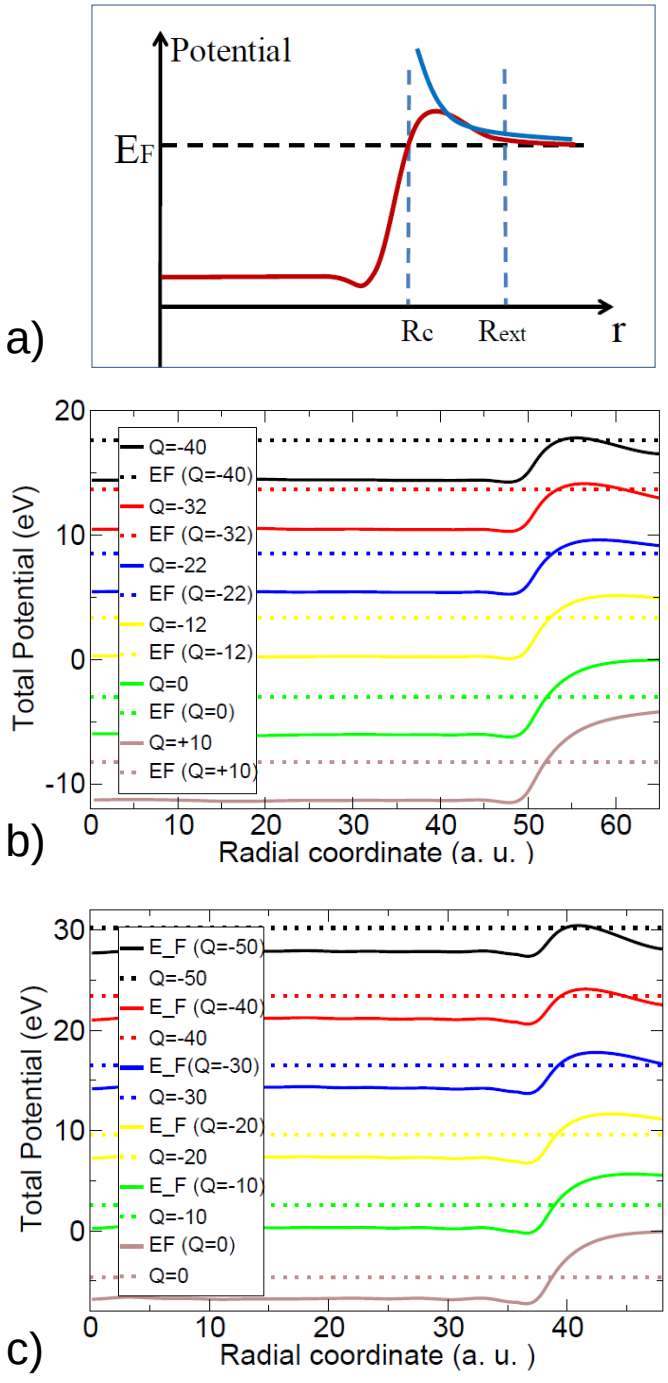

FIGURE 6.4: a) Schematic representation of the effective one-electron potentials for a small metallic negatively charged cluster. DFT result: red line. Pure Coulomb barrier $|Q|/r$: blue line. Horizontal dashed line shows energy of the Fermi level modified by the cluster charge. The dashed vertical lines, represent the limits of the classically allowed regions of the electron motion (turning points), which are the cluster radius R_c and the limit R_{ext} given by the $|Q|/r$ Coulomb barrier. For $R_c < r < R_{ext}$ an electron is in the tunneling regime. Panels b) (Sodium) and c) (Silver) show the effective one-electron potentials (continuous lines) and Fermi level energies (dashed lines) calculated with DFT for the charged clusters as explained in the inserts.

particle dynamics and has not been attempted here.

The fact that only limited number of electrons that can be added to the cluster before the electron population starts to decay require some special treatments if one wants to look at the ground state properties of the"overcharged" clusters. To obtain the results discussed above for negative charge $Q < Q_{\rm cr}$ we performed the DFT ground state calculations for the restricted geometry, where the size of the computational mesh is set such that the covered range of the radial coordinates $r < R_{ext}$. $r \geq R_{ext}$ corresponds to the region of the classically allowed motion outside cluster for the electron with Fermi energy, as shown in Fig. 6.4. This allows to restrain electrons to inside cluster and to converge the ground state calculations even for the negative charges exceeding the threshold value.

6.4. Absorption cross-section

In order to calculate the absorption cross-section of the charged clusters under the presence of an electromagnetic wave, we use the Kohn-Sham (KS) formulation of the time dependent density functional theory [129] detailed in the previous Chapter. The $\psi_j(\vec{r})$ orbitals obtained in the DFT ground state study are used as an initial states for the solution of the time-dependent equations describing the electron density dynamics in the system in response to the impulsive perturbation. For the"overcharged" clusters with negative charge $Q < Q_{\rm cr}$ the computational mesh has been restricted to $r < R_{ext}$ which allows to stabilize the system and avoid the population decay.

In Fig. 6.5 we present the TDDFT results for the the time evolution of induced dipoles and optical response of the charged Na [panels a) and c)] and Ag [panels b) and d)] clusters. As follows from our results, the charging of the cluster affects both the energy and width of the plasmon resonance, albeit in a very moderate way as has been also reported in Ref. [178]. Stronger effects are produced (i) by the negative charges, and (ii) for the Na cluster with lower work function and thus larger electron density spill out into the vacuum. In general, the removal of the electrons from the cluster (*positively charged clusters*) leads to the *blue shift* of the plasmon resonance frequency, and the plasmon resonance becomes narrower and better defined. Adding electrons to the cluster (*negatively charged clusters*) leads to the *red shift* of the plasmon resonance. These results are in full accord with earlier experimental and theoretical data reported in

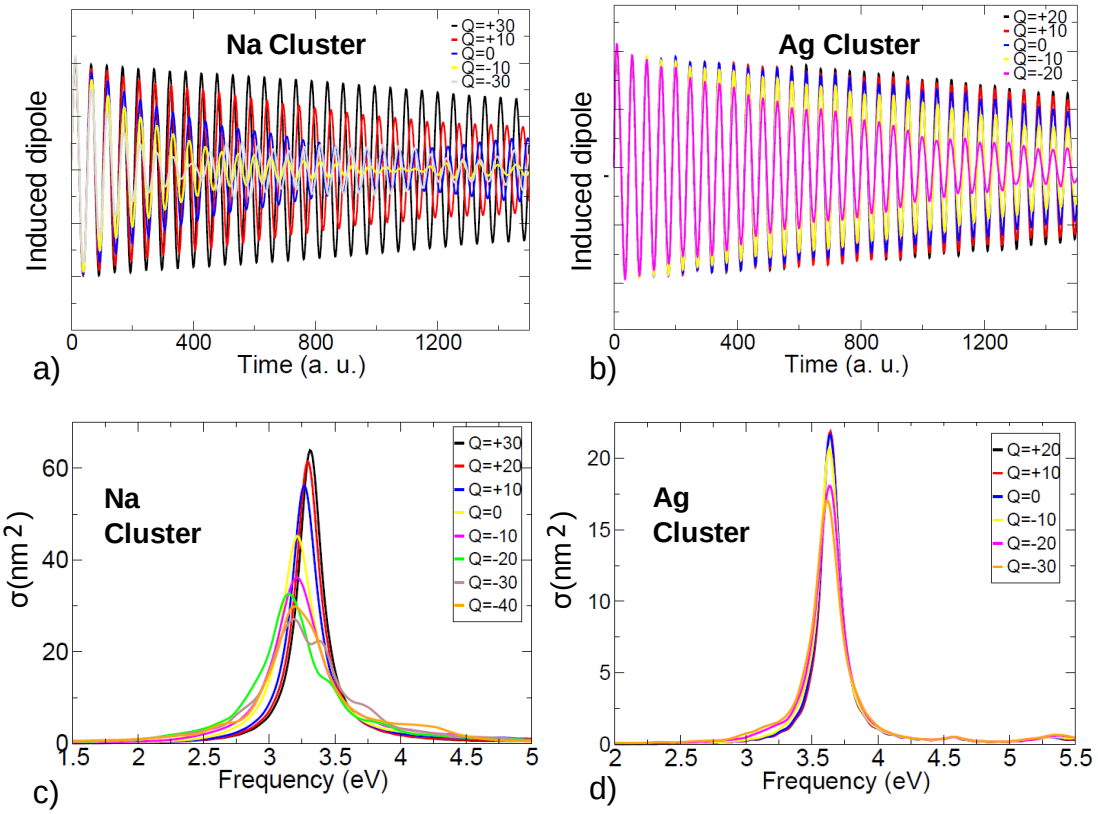

FIGURE 6.5: TDDFT calculations of the optical response of the charged clusters. Panels a) (sodium) and b) (silver) show the time evolution of the dipole induced in the charged cluster by the impulsive perturbation. Panels c) and d) show the corresponding absorption spectra. Different colors are used for the results obtained with different cluster charges as indicated in the insets.

cluster physics [195, 224–229], and are opposed to the assumptions frequently made in the explanation of the photochemical data, where negative/positive charge on the cluster is supposed to blue/red shift the plasmon resonance through the overall increase/decrease of the electron density n.

As has been shown in the theory of dynamic screening [56, 230–232], the shift of the dipolar plasmon frequency from the classical Mie value given by $\omega_p/\sqrt{3}$ is proportional to the position of the dynamically induced screening charges with respect to the cluster boundary. For positively charged cluster the electrons are tighter bound in the strong attractive potential well. The spill out of the electron density outside cluster boundaries decreases leading to the blue shift of the dipolar plasmon frequency as compared to that for the neutral cluster. At variance, for the negatively charged clusters, the electron density protrudes further away from the cluster boundaries because of the reduced binding

so that the dipolar plasmon redshifts.

The broadening of the absorption resonance for the negatively charged clusters as seen in the optical absorption cross section in Fig. 6.5c) and Fig. 6.5d) reflects faster decay of the underlying plasmon mode, as clearly seen in the time domain dynamics of the induced dipoles in Fig. 6.5a) and Fig. 6.5b). The increase of the decay rate is associated with increased coupling between plasmon and continuum of the one-particle electron-hole excitations, where along with the hot electron production inside cluster, the hot electron produced by the plasmon decay can be emitted from the cluster [233]. Considering the work function of silver ($\Phi = 4.65$ eV) and sodium ($\Phi = 3.$ eV) clusters addressed in this work, the dipolar plasmon decay with electron emission is impossible for silver, and concerns only the electrons within ~ 0.2 eV energy range from the Fermi level for sodium cluster. However, the Fermi level E_F^Q of the negatively charged cluster ($Q < 0$) approaches the vacuum level as expressed with Eq. 6.2. As a result, the probability of the plasmon decay with electron emission grows. Alternatively, the positive charge ($Q > 0$) the overall binding energy of the cluster electrons increases and these are tighter confined within cluster boundaries.

6.5. TDDFT study of the electron population decay in negatively charged clusters

6.5.1. Analytical expressions

As explained above, for the negatively charged clusters, when the negative charge exceeds $Q_{\rm cr}$ by $q = Q - Q_{\rm cr}$, the extra charge q decays because of the electron escape into the continuum. Prior to the discussion of the results of the TDDFT studies of this effect let us outline some simple theoretical considerations which ease understanding of the numerical data. The WentzeI-Kramers-Brillouin (WKB) approximation allows reliable estimation of the decay rate of the population of the cluster electronic states close to the Fermi level E_F via resonant (energy conserving) tunneling through the potential barrier located at $R_c \leq r \leq R_{ext}$ shown in Fig. 6.4. The probability of the barrier penetration and so the decay rate Γ is proportional to $\Gamma \sim \exp(-2\gamma)$, where the γ parameter is given by:

$$\gamma = \int_{R_c}^{R_{ext}} \sqrt{2\left[\frac{|Q|}{r} - E_F\right]}\, dr. \tag{6.9}$$

Here we made an approximation assuming that the $-Q/r$ dependence of the potential acting on tunneling electron holds over the entire classically forbidden region $R_c \leq r \leq R_{ext}$. This allows to use the derivations well developed in the theory of alpha-decay [234]. Eq. 6.9 can be rearranged into the form

$$\gamma = \sqrt{2E_F} \int_{R_c}^{R_{ext}} \sqrt{\frac{|Q|}{E_F}\frac{1}{r} - 1}\; dr. \tag{6.10}$$

Using $\frac{|Q|}{E_F} = R_{ext}$ [Eq. (6.5)], we finally obtain the main working equation defining the penetration constant.

$$\gamma = \sqrt{2E_F} \int_{R_c}^{R_{ext}} \sqrt{\frac{R_{ext}}{r} - 1}\; dr. \tag{6.11}$$

Since $r \leq R_{ext}$, we can use the variable change $r = R_{ext}\ \sin^2(\psi)$ and transform Eq. (6.11) to:

$$\gamma = 2R_{ext}\ \sqrt{2E_F} \int_{\arcsin\left[\sqrt{R_c/R_{ext}}\right]}^{\pi/2} \cos^2(\psi)\ d\psi \tag{6.12}$$

Finally, we obtain the sought penetration factor γ as

$$\gamma = R_{ext}\sqrt{2E_F}\left[\pi/2 - \arcsin\left(\sqrt{R_c/R_{ext}}\right) - \sqrt{R_c/R_{ext}}\sqrt{1 - R_c/R_{ext}}\right], \tag{6.13}$$

where the external radius R_{ext} is given by eq. (6.6).

Analytical derivation given by Eq. 6.13 allows discussion of the threshold behaviour of the population decay for $E_F \to 0^+$, where the decay rate is small and it is difficult to obtain from the full quantum TDDFT calculations. In this case the cluster charge is given by $Q = Q_{\rm cr} + q$ ($q \to 0^-$), and $R_c/R_{ext} << 1$ [see Eq. 6.5]. Using asymptotic expansion we obtain

$$\gamma = R_{ext}\sqrt{2E_F}\left[\pi/2 - \sqrt{R_c/R_{ext}} - (1 - R_c/2R_{ext})\ \sqrt{R_c/R_{ext}}\right]. \tag{6.14}$$

Keeping the terms of the same order with respect to R_c/R_{ext} leads to

$$\gamma = R_{ext}\sqrt{2E_F}\left[\pi/2 - 2\sqrt{R_c/R_{ext}}\right]. \tag{6.15}$$

Since $E_F = |Q|/R_{ext}$ Eq. (6.15) further simplifies to

$$\gamma = \sqrt{2QR_{ext}}\left[\pi/2 - 2\sqrt{R_c/R_{ext}}\right]. \tag{6.16}$$

For $R_{ext} \to \infty$ the leading term is

$$\gamma = \frac{\pi}{\sqrt{2}}\sqrt{QR_{ext}}. \tag{6.17}$$

Recaling that the external radius, is given by Eq. 6.6 and taking $Q = Q_{\rm cr} + q$, we obtain for R_{ext}

$$R_{ext} = \frac{Q_{\rm cr}}{q}\ R_c. \tag{6.18}$$

and

$$\gamma = \frac{\pi}{\sqrt{2}}\ |Q_{\rm cr}|\ \left(\frac{R_c}{|q|}\right)^{1/2}. \tag{6.19}$$

Therefore, since the charge population decay rate is given by $\Gamma = \Gamma_0 \exp\left[-2\gamma\right]$, we obtain

$$\Gamma = \Gamma_0 \exp\left[-\sqrt{2}\pi\ |Q_{\rm cr}|\ \left(\frac{R_c}{|q|}\right)^{1/2}\right], \tag{6.20}$$

where $|Q_{\rm cr}| = \Phi R_c$, is the difference between the total cluster charge and the threshold charge for the onset of decay $Q_{\rm cr}$, and Γ_0 is a parameter that can be determined comparing predictions of Eq. 6.20 and TDDFT results.

6.5.2. TDDFT results

In the TDDFT studies of the electron population decay for the negatively charged clusters, the $\psi_j(\vec{r})$ orbitals obtained in the DFT ground state calculations on restricted-size mesh are used as an initial states for the time propagation. However, in difference to the calculation of the absorption cross-section, the confinement constraint has been lifted off at the time moment $t = 0$ by providing the mesh size extending to $r \gg R_{ext}$. The negative charge of the cluster can then decay via electron escape into the vacuum. In Fig. 6.6.a) and in Fig. 6.6.b) we show the the time evolution of the cluster charge $Q(t)$ or of the excess charge defined as $q(t) = Q(t) - Q_{\rm cr}$ calculated for Na and Ag clusters. For the highly charged clusters ($Q \sim -50$), about 20 electrons are lost in less then 2000 a.u. of time (50 fs). The cluster charge drops, and the population decay slows down approaching time constants characteristic for the low initial charges. Indeed, the smaller is the cluster excess charge $|q(t)|$, the higher is the potential barrier separating potential well inside cluster from vacuum region. This results in the lower population decay rate Γ which is then a function of the time-dependent excess charge.

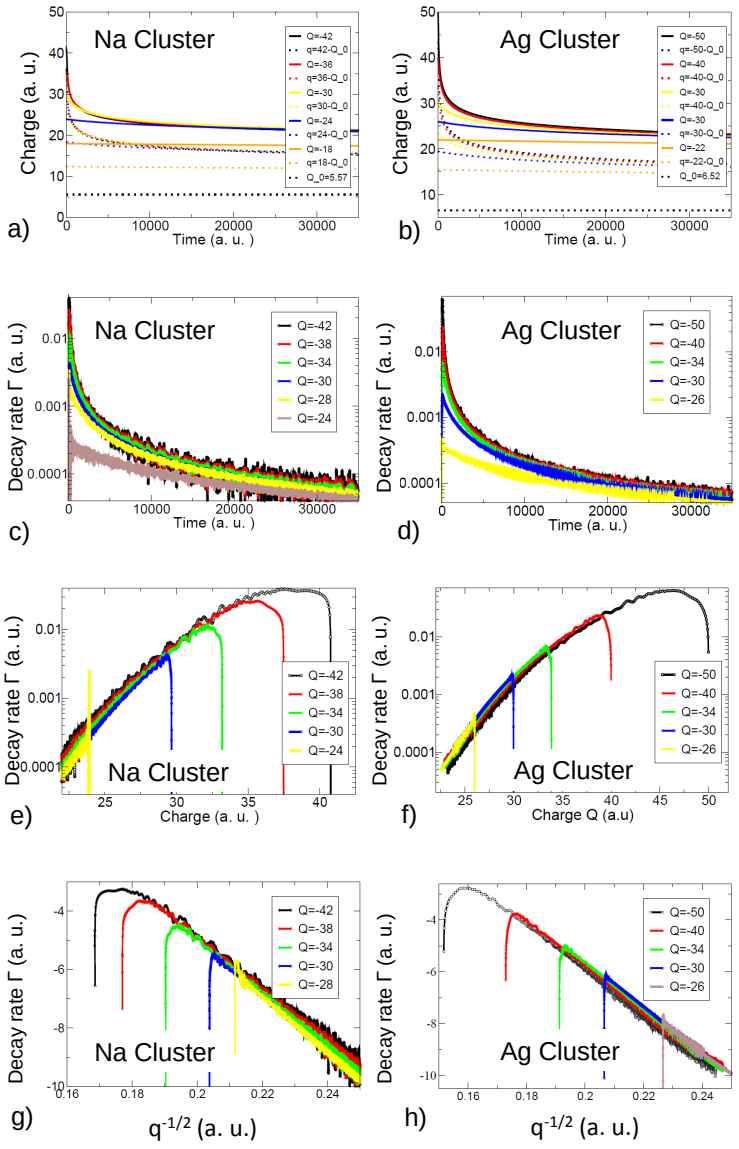

FIGURE 6.6: TDDFT analysis of the negative charge decay in small sodium (left column) and silver (right column) negatively charged clusters. Panels a) and b) time-evolution of the cluster charge Q(t) (solid lines) and excess charge above the decay threshold $q(t) = Q(t) - Q_{\rm cr}$ (dashed lines). Absolute values of the charges are shown. Different colors are used to display the results obtained with different initial charge $Q(t = 0)$ (excess charge $q(t = 0)$) as explained in the inserts. $t = 0$ is the instant of time when the computational constraints are released and system is allowed to decay. The threshold charge $|Q_{\rm cr}|$ is shown in black dashed line at the bottom of the panels. Panels c) and d): the time-dependence of the excess charge population decay rates as extracted from the data presented in panels a) and b) of this figure. Different colors are used to represent the results obtained with different initial cluster charge s explained in the inserts. Panels e) and f): the same as c) and d) but the results are shown as function of the instantaneous cluster charge $|Q(t)|$ Panels g) and h): analysis of the validity of the analytical approach: the logarithm of the instantaneous decay rate $ln(\Gamma(t))$ is shown as function of $\sqrt{1/|q(t)|}$. for different values of the initial cluster charge.

The analysis of the population decay rate Γ is presented in panels c) - h) of Fig. 6.6. Assuming the exponential decay of the excess charge, we introduce the instantaneous decay rate $\Gamma(t)$:

$$\frac{dq(t)}{dt} = -\Gamma(t)q(t). \tag{6.21}$$

From Eq. 6.21 it follows that

$$\Gamma(t) = -\frac{1}{q(t)}\frac{dq(t)}{dt}. \tag{6.22}$$

We use this equation to obtain $\Gamma(t)$ from the charge dynamics calculated with TDDFT (see Fig 6.6.c) and Fig 6.6.d). The decay rate is in overall slower for low initial charges and it also slows down in time as soon as the cluster becomes less charged. When the decay rate Γ is plotted as function of the instantaneous charge (see Fig 6.6.e) and Fig 6.6.f) results obtained with different initial cluster charges $Q(t=0)$ fall into unique universal curve. Thus, the potential barrier for electron tunneling and thus the decay rate is determined by the (instantaneous) cluster charge. The features at the short propagation times arise because the exponential decay needs some time to set in as known from the studies of the decaying quasi-stationary states [235].

In Fig 6.6.g) and Fig 6.6.h) the $\ln(\Gamma)$ is shown as function of the square root of the excess charge $\sqrt{|q(t)|}$. The same linear dependence is obtained irrespective from the initial cluster charge. This is inline with prediction of the semiclassical treatment given by Eq. 6.20. In e.g. case of silver clusters, the fit to the TDDFT results assuming

$$\Gamma = \Gamma_0 \exp\left[-\frac{B}{\sqrt{|q|}}\right] \tag{6.23}$$

gives (in atomic units) $B = 189$ which matches extremely well the

$$\Gamma = \Gamma_0 \exp\left[-\frac{178}{\sqrt{|q|}}\right] \tag{6.24}$$

dependence obtained from Eq. 6.20 with $R_c = 38.16$ a_0 and $Q_{cr} = 6.52$ a.u. Similar good agreement is obtained for Na clusters, where B=207 as obtained from the linear fit to the results in Fig 6.6.g has to be compared with $\sqrt{2R_c}\pi\ |Q_{cr}| = 176$. With the validity of the semiclassical approach established by comparison with TDDFT results, we can use Eq. 6.20 to analyse the evolution of the population decay rates for the clusters of varying size. Since the exponential function is proportional to $R_c^{3/2}/|q|^{1/2}$ the population decay rate can be expected to be similar for the charged clusters with $|q| \propto R_c^3$. Since

the number of electrons in the cluster N_e is also proportional to the cluster volume, we obtain that clusters characterized by $q/N_e = const$ should have similar time scales for the population relaxation. Using results shown in Fig 6.6a) and in Fig 6.6b) we conclude that half of the excess charge representing 2 % of the total number of electrons will be lost in 50 fs following the charging event. Thus, addition of small amount of electron representing only some percent of the total amount of the valence electrons in the nanoparticle renders the system highly unstable.

6.6. Summary and Conclussions

Using the TDDFT calculations on the charged clusters we have demonstrated in this chapter that the surface plasmon modes of small spherical clusters are only mildly sensitive to electron doping and do not present significant frequency shifts as has been also found in Ref. [178]. This is because the electron density in the cluster volume can not be changed and the excess charge is accumulated at the surface of the cluster.

In sheer contrast with an idea widely spread in the electrochemistry community, we show that the negative charge leads to the red shift of the plasmon frequency and the positive charge leads to the blue shift of the plasmon frequency. This result can be understood within the theory of the dynamical screening as a consequence of the change of the electron spill out from the cluster boundaries.

We have also shown that even small (relative to the total number of electrons in the system) negative charge rises Fermi level of the cluster above the vacuum level and renders the system unstable. The extra charge of the cluster decays with characteristic time scales of some tens of fs that can be fully understood using an analytical study based on the WKB method, similar to the studies of the alpha-decay. This limits the possibility to charge the system and the larger is the cluster, the smaller amount of the negative charge Q it can admit relative to the total number of electrons in the cluster N_e. Our results indicate that $|Q|/N_e < 1\%$.

Our results on the charged clusters allow to critically reinterpret many of the experimental data obtained with electrochemistry, where the shift of the plasmon resonances has been

often attributed to the volume charging effects [206–209]. Based on our results, we tentatively propose an alternative explanation where the change of the dielectric environment in immediate vicinity of the cluster should be responsible for the observed shift of the plasmon fequency, as has been also conjectured in Refs. [236–238]

Chapter 7

General Summary

The main aim of this chapter is to summarize the most important contents and original contributions made in this thesis.

7.1. Analytical and numerical methods

In this thesis work, we have addressed several analytical and numerical methods to describe the optical response of sub-nanometric systems. These methods are listed as follows:

1. **Classical electrodynamics and solution of Maxwell's equations in metallic systems.**
    - **Finite Element Method (FEM):**, implemented in the COMSOL Multyphysics package [34], which allows to find approximate solutions to systems of partial differential equations (Maxwel'sl equations) describing the interaction of light with metal systems. In our case, we use this powerful numerical tool to study systems of tens of nanometers size.

- **Boundary Element Method (BEM):**, implemented in a home-made code[1], basically permits to solve Maxwell's equations formulated as integral equations. We use this method in plasmonic extended gaps, where a high symmetry is desirable.

2. **Quantum methods to solve metallic systems in the nano and sub-nanometric regime.**

   - **Time-Dependent Density Functional Theory (TDDFT):** this formalism allows a quantum description of the density dynamics of hundreds to thousands of electrons in metallic nano-systems represented by a free-electron model (jellium). One can thus address nanoparticles, clusters or even hybrid nanostructures subjected to an external time-dependent potential[2].
   - **Quantum Corrected Model (QCM):** within this model, it is possible to describe the conductivity of a subnanometric cavity treating the junction as an effective medium, mimicking quantum tunneling within the classical local dielectric theory.

7.2. Studied Systems

We used the methods mentioned above to investigate the optical properties, confinement, tunneling process and in general the plasmonic behaviour of the following systems:

1. **Single nanoparticles**
   Where we have studied:

   - Confinement potential effects on the optical response of small metal nanoparticles.
   - Finite size effects in subnanometric spherical particles.

2. **Core-shell systems (cylindrical and spherical nanomatryoshkas) and plasmonic dimers**
   In these hybrid nanotructures we have studied:

[1] developed by Javier Aizpurua from the Theory of Nanophotonics Group at Materials Physics Center, Donostia-San Sebastian, España and Javier García de Abajo from nanophotonics theory group at Institut de Ciènces Fotòniques

[2] The codes used to this purpose, where gently shared by Andrei Borisov and Codruta Marinica from the Institut des Sciences Molèculaires d'Orsay, Universite Paris Sud, France.

- The physics of the plasmon coupling and the near-field enhancements in the plasmonic cavities formed in their junctions.
- The regime where quantum effects like tunneling become important.
- A mechanism of active control of the conductive coupling in plasmonic gaps between metallic nanoparticles via the bias-induced change of the barrier for electron tunneling across the gap.

3. **Small charged cluster**
   We have performed full quantum calculations of the electron dynamics in small spherical charged clusters in order to study:
   - The optical response and the frequency shifts of the plasmon resonances as a function of the cluster charge.
   - Stability and charge excess decay in negatively charged clusters and the correspondence with analytical studies based on the WKB method.

7.3. Main results

The following original results are obtained in this thesis.

1. We have demonstrated the applicability of the quantum corrected model to the description of the optical properties and plasmonic modes in systems which show an extended tunneling contact region between metallic surfaces.

2. We obtained that when the core-shell gap (in Na nanomatryoshkas) is reduced below 5 Å, the optical response is determined by the quantum tunneling of conduction electrons across the potential barrier separating the core and the shell. Our results agree with earlier calculations on canonical systems like plasmonic dimers.

3. We have demonstrated that the quantum corrected model performs very well over a wide range of core-shell gap sizes and geometries.

4. Thus, we could apply the quantum corrected model to describe the experimental findings in gold nanomatryoshkas of tens of nm size, where full quantum calculations are currently not feasible. From the comparison between the experimental and theoretical data we could show that, in case of subnanometric gaps between

the core and the shell functionalised with self-assembled molecular layer(s), the tunneling through the latter determines the optical response of the nanostructure.

5. With TDDFT and QCM calculations we have demonstrated that the optical response of a plasmonic gap can be electrically controlled by an external DC bias. We could elucidate the mechanism underlying this effect which is the bias induced change of the electron tunneling conductance across the gap.

6. Our proof-of -principle calculations show that metal nanoparticle plasmonics can benefit from the reversibility, fast response time, and versatility of an active control strategy based on applied bias. This provides a new platform for many practical applications in optoelectronics and photonics.

7. Using TDDFT calculations we have demonstrated that the localised plasmon modes of small spherical clusters are only mildly sensitive to electron doping and do not present significant frequency shifts. Consistently with the theory of dynamical screening at surfaces, and in contrast to wide spread ideas, the negative charge of the cluster leads to a small red shift of the plasmon frequency and the positive charge leads to a small blue shift of the plasmon frequency.

8. We have demonstrated that even small, negative charge of the cluster, relative to the total number of electrons in small charged systems, rises the Fermi level above the vacuum level and renders the system unstable. The extra charge decays with characteristic time scales of some tens of fs. This, in fact, limits the possibility to charge the system. The larger the cluster is, the smaller amount of negative charge Q it can admit relative to the total number of electrons in the cluster N_e. Overall, $|Q|/N_e < 1\%$.

9. Our results on the charged clusters allow to critically reinterpret many of the experimental data obtained with electrochemistry, where the shift of the plasmon resonances has been often attributed to charging effects. Based on our results, we tentatively propose an alternative explanation based on the change of dielectric environment in immediate vicinity of the clusters as the main reason for plasmon shifts in electrochemical environments.

Appendix A

Quantum model for a free electron gas in a nanoparticle

A.1. Free electron gas in a cubic infinite box

In a simplified quantum model described by Genzel and Martin in [26], which is based on a set of free (valence) electrons confined in a box or cubic potential well with infinite sides, the electron wave function is well known and given by

$$\Psi_{hkl} = \left(\frac{8}{L^3}\right) \sin\left(\frac{h\pi x}{L}\right) \sin\left(\frac{k\pi y}{L}\right) \sin\left(\frac{l\pi z}{L}\right), \tag{A.1}$$

where L is the lenght of the potential well and the h, k, l are positive integers. For each wave function, the corresponding energy levels are given by

$$E_{h,k,l} = E_0(h^2 + k^2 + l^2) \tag{A.2}$$

with $E_0 = \frac{\pi^2\hbar^2}{2mL^2}$. In this model, the dielectric function of a single metal nanoparticle is given by

$$\varepsilon(\omega) = \varepsilon_\infty + \frac{\omega_p^2}{N} \sum_{i,f}^{m} \frac{s_{if}(F_i - F_f)}{\omega_{if}^2 - \omega^2 - i\omega\gamma_{if}}, \tag{A.3}$$

where ε_∞ corresponds to the interband contribution, N to the number of particles confined in the particle and the plasmon frequency ω_p is given in terms of the electronic

density n, the elemental electric charge e and the effective mass m^*,

$$\omega_p^2 = \frac{4\pi n e^2}{m^*}. \tag{A.4}$$

The terms s_{if}, ω_{if} and γ_{if} are respectively, the oscillator strenght, the eigen frequency and the damping for the dipole transition from a initial state i to another final state f. F_i and F_f are the values of the Fermi-Dirac distribution function for the initial and final states. The oscillator strenght has the standard dipolar form

$$s_{if} = \frac{2m\omega_{if}}{\hbar}|\langle f|z|i\rangle|^2. \tag{A.5}$$

The orthogonallity of the eigen-functions, gives the relation

$$\omega_{if} = \Delta l(2l + \Delta l)\frac{E_0}{\hbar} \tag{A.6}$$

and considering only transitions in a z direction, s_{if} can be written by

$$s_{if}^2 = \frac{64}{\pi^2}\frac{l^2(l+\Delta l)^2}{\Delta l^3(l+\Delta l)^3}\delta(h_i, h_f)\delta(k_i, k_f). \tag{A.7}$$

The number of dipole transitions in the sum of the dielectric function depends on the initial and final values of the quantum number l corresponding solely to initial states within the Fermi surface through final states just outside the Fermi surface. Considering the number of valence electrons in each nanoparticle N and taking only transitions with $\Delta l = 1$, the final expression obtained in [26] reads

$$\epsilon(\omega) = \epsilon_\infty + \omega_p^2 \sum_{\Delta l}^{1,3,\ldots} \sum_{l}^{l_F} \frac{S_{l,\Delta l}}{\omega_{l,\Delta l}^2 - \omega^2 - i\omega\gamma_{l,\Delta l}} \tag{A.8}$$

where

$$S_{l,\Delta l} = \frac{32}{\pi l_F}\frac{l^2(l+\Delta l)^2}{\Delta l^2(l+\Delta l)^2} \tag{A.9}$$

In other derivation made by Scholl *et. al.* in [55], the conduction electrons are considered as a free electron gas constrined by an infinite potential barriers at the physical edges of the particles. Details are showed in Chapter 2 They take the transition frequencies ω_{if} as the corresponding to the transitions of conduction electrons from occupied states i to unocupied states f inmediately outside of it. The dielectric function $\varepsilon(\omega)$ is given in terms of the constant plasmon bulk frequency ω_p , the damping (or scattering) frequency

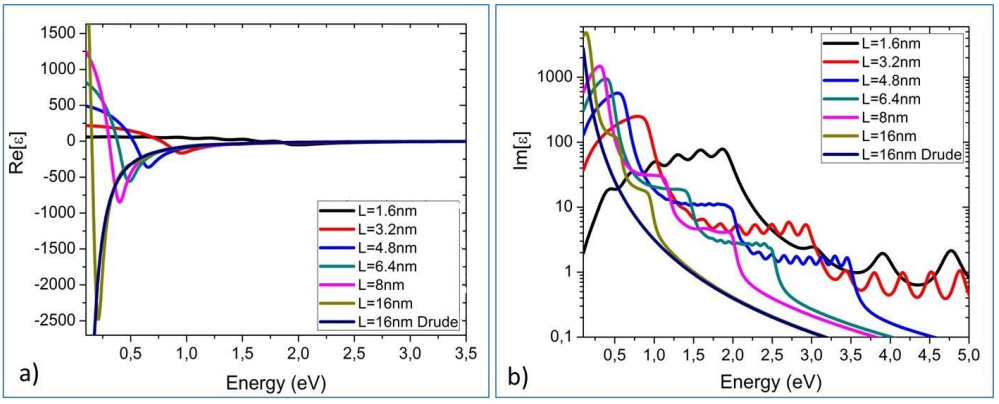

FIGURE A.1: a) Real and b) imaginary parts of the dielectric function for a silver nanoparticle of lenght $L = 1.6, 3.6, 4.8, 6.4, 8$ and 16 nm. Using an infinite cubic confinement potential.

dependent of the particle radius $\gamma(R) = \gamma_{bulk} + Av_F/R$ and the oscillator strenghts S_{if} in the form

$$\varepsilon(\omega) = \varepsilon_{IB} + \omega_p^2 \sum_i \sum_f \frac{S_{if}}{\omega_{if}^2 - \omega^2 - i\gamma\omega}. \tag{A.10}$$

In this expression, S_{if} and ω_{if} are given respectively by

$$S_{if} = \frac{2M\omega_{if}}{\hbar N} |\langle f|z|i\rangle|^2. \tag{A.11}$$

Where N is the number of conduction electrons in the nanoparticle and

$$\omega_{if} = \frac{E_f - E_i}{\hbar}. \tag{A.12}$$

If the conduction electrons are treated as particles in a infinite spherical well, the energy eigen-values will depend on the quantum numbers n (principal) and l (azimuthal) in the form:

$$E_{n,l} = \frac{\hbar^2\pi^2}{8MR^2}(2n + l + 2)^2, \tag{A.13}$$

with M the mass of the electron. Using Eq. (A.8), the real and imaginary parts of the dielectric function in terms of the the incident photon energy for nanoparticles with $L = 1.6, 3.6, 4.8, 6.4, 8$ and 16 nm (we can relate the lenght of the cube L with the radius of a nanosphere by the expresion $L = (\frac{4\pi}{3})^{1/3}R$), is showed in Fig. A.1 comparing with the classic Drude approach given by eq. (1.2) in the case of $L = 16$nm. We observe

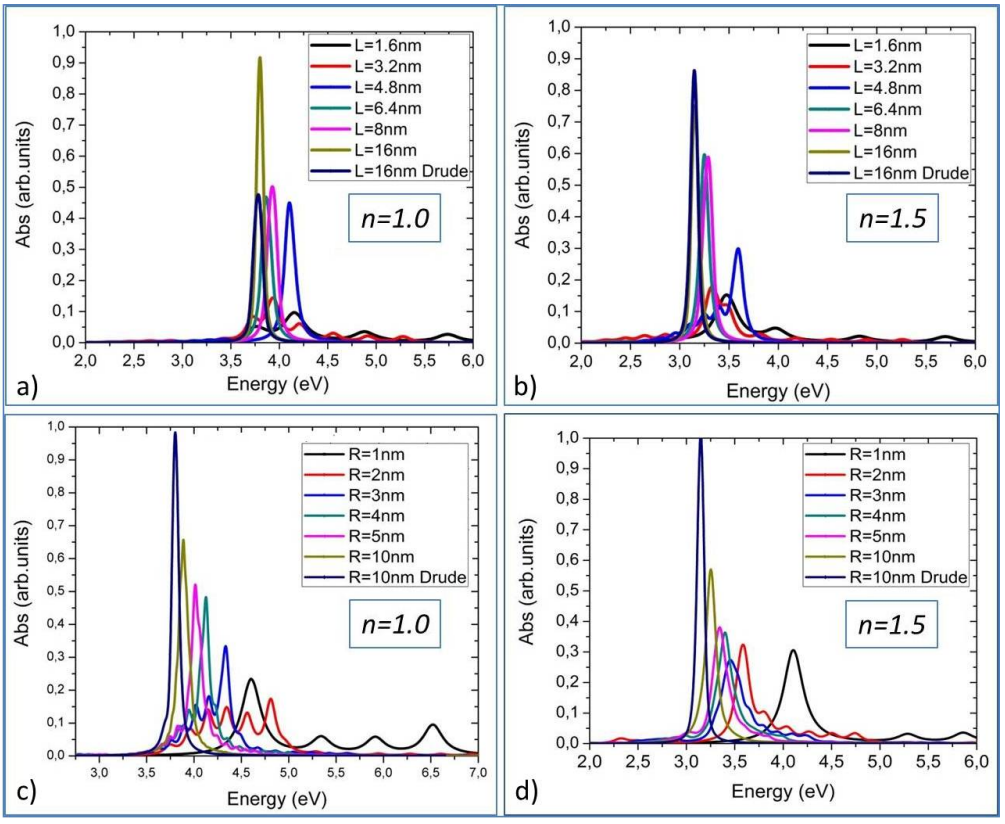

FIGURE A.2: Absorption spectra for a silver nanoparticle using the optical constants from the quantum model: Infinite cubic potential (a and b) and infinite spherical potential (c and d) for different particle sizes (L=1.6, 3.2, 4.8, 6.4, 8 and 16 nm and R=1, 2, 3, 4, 5 nm and 10 nm). The graphs a) and c) correspond to a refractive index of surrounding medium $n = 1.0$ and the graphs b) and d) to $n = 1.5$.

that the dielectric functions predicted by the quantum model disagree notably with the classical results in the range studied. The main difference is that both Re[ϵ] and Im[ϵ] exhibit a nonmonotic behavior according to the quantum model, versus the monotonic response using classical Drude theory. However, as the lenght reaches the limit of 16 nm, the agreement with the classical description is good.

To solve the problem of light-nanoparticle interaction, we use the analytical expressions of η and κ previously calculated for each particle size and confinement potential to solve the vector Maxwell equations numerically, by means of a standar finite element method (FEM). For an isolated silver particle with different sizes ($R = 1, 2, 3, 4, 5$ and 10 nm), we compare the solutions for the different sets of optical constants, which are taken as input parameters.

Figure A.2, shows the resonance value from each absorption spectra for both confinement potential (cubic and spherical), depending on the surrounding environment: air, with refractive index $n = 1.0$ and SiO_2 (glass) with $n = 1.5$, in which we observe that the LSPR in both spectra change significantly with this parameter, showing that in the glass case, the plasmon resonance values are more defined and follow a well marked tendency relative to real experiments (see [55] and [56]).

Bibliography

[1] Esteban, R.; Borisov, A. G.; Nordlander, P.; Aizpurua, J., "Bridging quantum and classical plasmonics with a quantum-corrected model," Nature Commun. **3,** 825 (2012).

[2] Esteban, R.; Zugarramurdi, A.; Zhang, P.; Nordlander, P.; Garcia-Vidal, F. J.; Borisov, A. G.; Aizpurua, J. A "Classical treatment of optical tunneling in plasmonic gaps: extending the quantum corrected model to practical situations". Faraday Discussions **178**, 151-183, 2015.

[3] Kulkarni, V.; Prodan, E.; Nordlander, P. "Quantum plasmonics: optical properties of a nanomatryoshka". Nano Lett. 2013, **13** (12), 5873-5879.

[4] Zapata, M.; Beltran, A. S. C.; Borisov, A. G.; Aizpurua, J., "Quantum effects in the optical response of extended plasmonic gaps: validation of the quantum corrected model in core-shell nanomatryoshkas". Optics Express, **23** (6), 8134, 2015.

[5] Lin, L.; Zapata, M.; Xiong, M.; Liu, Z.; Wang. S.; Xu, H.; Borisov, A. G.; Gu, H.; Nordlander, P.; Aizpurua, J.; Ye, J.; "Nanooptics of Plasmonic Nanomatryoshkas: Shrinking the Size of a Core-Shell Junction to Subnanometer." Nano Lett, **15** (10), 6419, 2015.

[6] Marinica, D. C.; Zapata, M.; Nordlander, P.; Kazansky, A. K.; Echenique, P. M.; Aizpurua, J.; Borisov, A. G.; "Active quantum plasmonics." Sci. Adv. **1**, e1501095 (2015).

[7] Zapata, M; Borisov. A. G.; Kazanski, A.; Aizpurua, J., "Quantum Plasmonics and charged cluster dynamics". Submitted to Langmuir.

[8] Stewart, M. E.; Anderton, C. R.; Thompson, L. B.; Maria, J.; Gray, S. K ; Rogers, J. A.; Nuzzo, R. G., "Nanostructured Plasmonic Sensors," Chem. Rev. **108,** 494–521 (2008).

[9] Goncalves, M. R., "Plasmonic nanoparticles: fabrication, simulation and experiments". J. Phys. D: Appl. Phys. **47**, 213001 (2014).

[10] Herreño-Fierro, C. A.; Patiño, E. J.; Armelles, G.; Cebollada, A., "Surface sensitivity of optical and magneto-optical and ellipsometric properties inmagnetoplasmonic nanodisks". App. Phys. Lett., **108,** 021109 (2016).

[11] Mie, G., "Beitrage zur Optik truber Medien, speziell kolloidaler Metalloesunge", Ann. Phys. **25**, 377 (1908).

[12] Ritchie, R. H., "Plasma Losses by Fast Electrons in Thin Films" *Phys. Rev*, **106**, 5, 1957

[13] Maier, S. A., "Plasmonics: Fundamentals and applications" Springer, 2007.

[14] Pelton, M.; Aizpurua, J.; Bryant, G. W., "Metal-nanoparticle plasmonics". Laser Photon. Rev. **2,** 136-159 (2008).

[15] Schuller, J. A.; Barnard, E. S.; Cai, W.; Jun, Y. C.; White, J. S.; Brongersma, M. L., "Plasmonics for extreme light concentration and manipulation". Nature Materials **9,** 193204 (2010)

[16] Alvarez-Puebla, R.; Liz-Marzán, L. M.; García de Abajo, F. J., "Light Concentration at the Nanometer Scale". J. Phys. Chem. Lett. **1**, 2428 (2010).

[17] Anker, J. N.; Hall, W. P.; Lyandres, O.; Shah, N. C.; Zhao, J.; Van Duyne, R. P., "Biosensing with plasmonic nanosensors", Nature Materials **7,** 442 (2008).

[18] Kinkhabwala, A.; Yu, Z.; Fan, S.; Avlasevich, Y.; Mullen, K.; Moerner, W. E., "Large single-molecule fluorescence enhancements produced by a bowtie nanoantenna" Nature Photonics **3**, 654 (2009).

[19] Xu, H.; Aizpurua, J.; Käll, M.; Apell, P., "Electro-magnetic Contributions to Single-Molecule Sensitivity in Surface-Enhanced Raman Scattering," Physical Review E, **62,** 3, 4318-4324, 2000.

[20] Lal, S.; Clare, S. E.; Halas. N. J., "Nanoshell-enabled photothermal cancer therapy: impending clinical impact" Accounts of chemical research **41,** 1842-1851 (2008).

[21] Gramotnev, D. K.; Bozhevolnyi, S. I.; "Plasmonics beyond the difraction limit", Nature Photonics **4**, 83 (2010)

[22] Akimov, A. V.; Mukherjee, A.; Yu, C. L.; Chang, D. E.; Zibrov, A. S.; Hemmer, P. R.; Park, H.; Lukin, M. D., "Generation of single optical plasmons in metallic nanowires coupled to quantum dots", Nature **450,** 402 (2007).

[23] Kauranen, M.; Zayats, A. V., "Nonlinear plasmonics" Nature Photonics **6**, 737 (2012).

[24] Baffou, G.; Quidant, R., "Nanoplasmonics for chemistry", Chem. Soc. Rev. **43**, 3898 (2014).

[25] Clavero, C. "Plasmon-induced hot-electron generation at nanoparticle/metal-oxide interfaces for photovoltaic and photocatalytic devices." Nature Photonics **8**, 95–103 (2014).

[26] Genzel L., Martin T. P. Kreibig U., "Dielectric function and plasma resonances of small metal particles", Z. Physik B, **21**, 339, 1975.

[27] I. Villo-Perez, Z. L. Miskovic and N. R. Arista.; "Trends in nanophysics". Springer Verlag Heidelberg, 2010.

[28] Puska. M. J. et al., "Electronic polarizability of small metal spheres", Phys. Rev. B, **31**, 6, 1985.

[29] Sönnichsen, C. Ph. D Dissertation, Munich University, 2001.

[30] Johnson, P. B.; Christy, R. W., "Optical Constants of the Noble Metals" Phys. Rev. B. **6**, 12, 4370 (1972)

[31] http://www.sspectra.com/sopra.html

[32] Bohren, C. F.; Huffman, D. R., "Absorption and Scattering of Light by Small Particles". John Wiley & Sons, Inc., New York, 1998.

[33] Poyli. M. A., "Theory and simulations of the optical response of novel nanomaterials from visible to teraherz". PhD. Thesis. Theory of Nanophotonics Group, Donostia International Physics Center, 2015.

[34] www.comsol.com

[35] Arias-Castro, J. C.; Camacho-Beltrán, A. S., "Surface Plasmon Resonance of a Few Particles Linear Arrays", Journal of Electromagnetic Analysis and Applications, 2011, **3,** 458-464

[36] Stockman, M. I., "Nanoplasmonics: The physics behind the applications", Physics Today **64** (2), 39 (2011).

[37] Nordlander, P.; Oubre, C.; Prodan, E.; Li, K.; Stockman, I.; " Plasmon Hybridization in Nanoparticle Dimers", Nano Lett. **4,** 5, 899 (2004).

[38] Zuloaga, J.; Prodan, E.; Nordlander, P., "Quantum description of the plasmon resonances of a nanoparticle dimer," Nano Lett. **9,** 887 (2009).

[39] Marinica, D. C.; Kazansky, A. K.; Nordlander, P.; Aizpurua, J.; Borisov, A. G., "Quantum Plasmonics: Nonlinear Effects in the Field Enhancement of a Plasmonic Nanoparticle Dimer," Nano Lett. **12,** 1333 (2012).

[40] Ciracì, C.; Pendry, J. B.; Smith, D. R., "Hydrodynamic Model for Plasmonics: A Macroscopic Approach to a Microscopic Problem"., ChemPhysChem **14**, 1109–1116 (2013)

[41] Stella, L.; Zhang, P.; García-Vidal, F. J.; Rubio, A.; Garcia-Gonzalez, P.; "Performance of Nonlocal Optics When Applied to Plasmonic Nanostructures," J. Phys. Chem. C **117,** 8941–8949 (2013).

[42] Teperik, T. V.; Nordlander, P.; Aizpurua, J.; Borisov, A.G., "Robust Subnanometric Plasmon Ruler by Rescaling of the Nonlocal Optical Response," Phys. Rev. Lett. **110,** 263901 (2013).

[43] Andersen, K.; Jensen, K. L.; Mortensen, N. A.; Thygesen, K. S., "Visualizing hybridized quantum plasmons in coupled nanowires: From classical to tunneling regime," Phys. Rev. B **87,** 235433 (2013).

[44] Aksu, S.; Huang, M.; Artar, A.; Yanik, A. A.; Selvarasah, S.; Dokmeci, M. R.; Altug, H., "Flexible Plasmonics on Unconventional and Nonplanar Substrates", Advanced Materials **23,** 4422 (2011).

[45] Huang, F.; Baumberg, J. J. ; "Actively tuned plasmons on elastomerically driven Au nanoparticle dimers." Nano Lett. **1**0, 1787 (2010)

[46] Khatua, S.; Chang, W.-S.; Swanglap, P.; Olson, J.; Link, S., "Active Modulation of Nanorod Plasmons", Nano Lett. **11,** 3797 (2011).

[47] Buchnev, O.; Ou, J. Y.; Kaczmarek, M.; Zheludev, N. I.; Fedotov, V. A.; "Electrooptical control in a plasmonic metamaterial hybridised with a liquid-crystal cell" Optics Express, **21,** 1633 (2013).

[48] Nikolajsen, T.; Leosson, K.; Bozhevolnyi, S. I.; "Surface plasmon polariton based modulators and switches operating at telecom wavelengths". Appl. Phys. Lett. **85,** 5833 (2004).

[49] Lereu, A. L.; Passian, A.; Goudonnet, J-P.; Thundat, T.; Ferrell, T. L.; "Optical modulation processes in thin films based on thermal effects of surface plasmons". Appl. Phys. Lett. **86,** 154101 (2005).

[50] Pacifici, D.; Lezec, H. J.; Atwater, H. A.; "All-optical modulation by plasmonic excitation of CdSe quantum dots" Nature Photonics **1,** 402 (2007).

[51] MacDonald, K. F.; Samson, Z. L.; Stockman, M. I.; Zheludev, N. I. "Ultrafast active plasmonics" Nature Photonics **3,** 55 (2009).

[52] Caspers, J. N.; Rotenberg, N.; Van Driel, H. M.; "Ultrafast silicon-based active plasmonics at telecom wavelengths", Optics Express **18,** 19761 (2010).

[53] Grigorenko, A. N.; Polini, M.; Novoselov, K. S., "Graphene plasmonics" Nature Photonics **6,** 749 (2012).

[54] Savage, K. J.; Hawkeye, M. M.; Esteban, R.; Borisov, A. G.; Aizpurua, J.; Baumberg, J. J., "Revealing the quantum regime in tunnelling plasmonics," Nature **491,** 574 (2012).

[55] Scholl, J.; Koh, A. L.; Dionne, J., "Quantum plasmon resonances of individual metallic nanoparticles", Nature, **483**, 421, 2012.

[56] Monreal, R. C.; Antosiewicz, T. J.; Apell, S. P., "Competition between surface screening and size quantization for surface plasmons in nanoparticles", New Journal of Physics **15**, 083044 (2013)

[57] In all our calculations, we use the standard set of parameters for silver taken from ref: [29, 30, 55] $\epsilon_\infty = 3.66$, $\omega_p = 9.01$eV, and $\gamma(R) = \gamma_{bulk} + \frac{Av_F}{R}$, with A=0.25 and $v_F = 1.4 \times 10^6 (m/s)$.

[58] Arfken, G. B.; Weber, H. J.; *Mathematical Methods for Physicists*, Harcourt/Academic Press (2001).

[59] He, Y.; Zeng, T.; "First principles study and model of dielectric functions of silver nanoparticles", J. Phys. Chem. C, **114**, 18023-18030 (2010).

[60] Wood, D., "Classical Size Dependence of the Work Function of Small Metallic Spheres", Phys. Rev. Lett. **46**, 11 (1981).

[61] We asume $f = 0.01$ value taken from ref. [55] and $\epsilon_m = 2.25$ corresponding to a nanosphere immersed in a glass matrix.

[62] Aćimović, S. S.; Kreuzer, M. P.; González, M. U.; Quidant, R., "Plasmon Near-Field Coupling in Metal Dimers as a Step toward Single-Molecule Sensing," ACS Nano **3,** 1231 (2009).

[63] Juluri, B. K.; Chaturvedi, N.; Hao, Q. Z.; Lu, M. Q;.Velegol, D.; Jensen, L.; Huang, T. J., "Scalable Manufacturing of Plasmonic Nanodisk Dimers and Cusp-Nanostructures Using Salting-out Quenching Method and Colloidal Lithography," ACS Nano **5,** 5838 (2011).

[64] Arielly, R.; Ofarim, A.; Noy, G.; Selzer, Y., "Accurate Determination of Plasmonic Fields in Molecular Junctions by Current Rectification at Optical Frequencies," Nano Lett. **11,** 2968 (2011).

[65] Kern, J.; Großmann, S.; Tarakina, N. V.; Häckel, T.; Emmerling, M.; Kamp, M.; Huang, J.-S.; Biagioni, P.; Prangsma, J. C.; Hecht, B., "Atomic-Scale Confinement of Resonant Optical Fields," Nano Lett. **12,** 5504 (2012).

[66] Duan, H.; Fernández-Domínguez, A. I.; Bosman, M.; Maier, S. A.; Yang, J. K. W., "Nanoplasmonics: Classical down to the Nanometer Scale," Nano Lett. **12,** 1683 (2012).

[67] Taylor, R. W.; Lee, T.-Ch.; Scherman, O. A.; Esteban, R.; Aizpurua, J.; Huang, F. M.; Baumberg, J. J.; Mahajan, S., "Precise Subnanometer Plasmonic Junctions for SERS within Gold Nanoparticle Assemblies Using Cucurbit[n]uril Glue", ACS Nano **5,** 3878 (2011).

[68] Danckwerts, M.; Novotny, L., "Optical Frequency Mixing at Coupled Gold Nanoparticles," Phys. Rev. Lett. **98,** 026104 (2007).

[69] Ward, D. R.; Hueser, F.; Pauly, F.; Cuevas, J. C.; Natelson, D., "Optical rectification and field enhancement in a plasmonic nanogap," Nature Nanotechnology **5,** 732 (2010).

[70] Jin, Y.; Jia, C.; Huang, S.-W.; O'Donnell, M.; Gao, X., "Multifunctional nanoparticles as coupled contrast agents," Nature Communications **1,** 41, (2010).

[71] Lim, D.-K.; Jeon, K.-S.; Hwang, J.-H.; Kim, H.; Kwon, S.; Suh, Y. D.; Nam, J.-M., "Highly uniform and reproducible surface-enhanced Raman scattering from

DNA-tailorable nanoparticles with 1-nm interior gap," Nature Nanotechnology **6,** 452–460 (2011).

[72] Kelly, L.; Coronado, E.; Zhao, L. L.; Schatz, G. C., "The Optical Properties of Metal Nanoparticles: The Influence of Size, Shape and Dielectric Environment," J. Phys. Chem. B **107,** 668 (2003).

[73] Halas, N. J.; Lal, S.; Chang, W.-S.; Link, S.; Nordlander, P., "Plasmons in Strongly Coupled Metallic Nanostructures," Chem. Rev. **111,** 3913 (2011).

[74] Pasquale, A. J.; Reinhard, B. M.; Negro, L. D.; "Engineering Photonic-Plasmonic Coupling in Metal Nanoparticle Necklaces," ACS Nano **5,** 6578 (2011).

[75] Quinten, M.; Leitner, A.; Krenn, J. R.; Aussenegg, F . R., "Electromagnetic energy transport via linear chains of silver nanoparticles," Opt. Lett. **23,** 1331 (1998).

[76] Maier, S. A.; Kik, P. G.; Atwater, H. A.; Meltzer, S.; Harel, E.; Koel, B. E.; Requicha, A. A. G., "Local detection of electromagnetic energy transport below the diffraction limit in metal nanoparticle plasmon waveguides," Nature Materials **2,** 229 (2003).

[77] Hao, E.; Schatz, G. C., "Electromagnetic fields around silver nanoparticles and dimers," J. Chem. Phys. **120,** 357 (2004).

[78] Romero, I.; Aizpurua, J.; Bryant, G. W., F. J. García de Abajo, "Plasmons in nearly touching metallic nanoparticles: singular response in the limit of touching dimers," Optics Express **14,** 9988 (2006).

[79] Jain, P. K.; El-Sayed, M. A., "Plasmonic coupling in noble metal nanostructures," Chem. Phys. Lett. **487,** 153 (2010).

[80] Xu, H.; Bjeneld, E.; Käll, M.; Börjesson, L., "Spectroscopy of Single Hemoglobin Molecules by Surface Enhanced Raman Scattering," Phys. Rev. Lett. **83,** 4357 (1999).

[81] Talley, C. E.; Jackson, J. B.; Oubre, C.; Grady, N. K.; Hollars, C. W.; Lane, S. M.; Huser, T. R.; Nordlander, P.; Halas, N. J., "Surface-Enhanced Raman Scattering from Individual Au Nanoparticles and Nanoparticle Dimer Substrates," Nano Lett. **5,** 1569 (2005).

[82] Theiss, J.; Pavaskar, P.; Echternach, P. M.; Muller, R. E.; Cronin, S. B., "Plasmonic Nanoparticle Arrays with Nanometer Separation for High-Performance SERS Substrates," Nano Lett. **10,** 2749 (2010).

[83] Fazio, B.; D'Andrea, C.; Bonaccorso, F.; Irrera, A.; Calogero, G.; Vasi, C.; Gucciardi, P. G.; Allegrini, M.; Toma, A.; Chiappe, D.; Martella, C.; de Mongeot, F. B., "Re-radiation Enhancement in Polarized Surface-Enhanced Resonant Raman Scattering of Randomly Oriented Molecules on Self-Organized Gold Nanowires," ACS Nano **5,** 5945 (2011).

[84] Gunnarsson, L.; Rindzevicius, T.; Prikulis, J.; Kasemo, B.; Käll, M.; Zou, S.; Schatz, G. C., "Confined Plasmons in Nanofabricated Single Silver Particle Pairs: Experimental Observations of Strong Interparticle Interactions," J. Phys. Chem. B **109,** 1079 (2005).

[85] Jain, P. K.; Huang, W.; El-Sayed, M. A., "On the Universal Scaling Behavior of the Distance Decay of Plasmon Coupling in Metal Nanoparticle Pairs: A Plasmon Ruler Equation," Nano Lett. **7,** 2080 (2007).

[86] Hill, R. T.; Mock, J. J.; Hucknall, A.; Wolter, S. D.; Jokerst, N. M.; Smith, D. R.; Chilkoti, A., "Plasmon Ruler with Angstrom Length Resolution," ACS Nano **6,** 9237 (2012).

[87] Ben, X.; Park, H. S., "Size-Dependent Validity Bounds on the Universal Plasmon Ruler for Metal Nanostructure Dimers," J. Phys. Chem. C **116,** 18944 (2012).

[88] Liu, N.; Hentschel, M.; Weiss, T.; Alivisatos, A. P.; Giessen, H.; "Three-Dimensional Plasmon Rulers," Science **332,** 1407 (2011).

[89] Stolz, A.; Berthelot, J.; Mennemanteuil, M-M; Colas des Francs, G.; Markey, L.; Meunier, V.; Bouhelier, A., "Nonlinear Photon-Assisted Tunneling Transport in Optical Gap Antennas," Nano Lett. **14,** 2330-2338, (2014).

[90] Berthelot, J.; Bachelier, G.; Song, M.; Rai, P.; Colas des Francs,G.; Dereux, A.; Bouhelier, A., "Silencing and enhancement of second-harmonic generation in optical gap antennas," Optics Express **20,** 10498 (2012).

[91] Hanke, T.; Krauss, G.; Träutlein, D.; Wild, B.; Bratschitsch, R.; Leitenstorfer, A., "Efficient Nonlinear Light Emission of Single Gold Optical Antennas Driven by Few-Cycle Near-Infrared Pulses," Phys. Rev. Lett. **103**, 257404 (2009).

[92] Palomba, S.; Danckwerts, M.; Novotny, L.; "Nonlinear plasmonics with gold nanoparticle antennas", J. Opt. A:Pure Appl. Opt. **11**, 114030 (2009).

[93] Cai, W.; Vasudev, A. P.; Brongersma, M. L.; "Electrically Controlled Nonlinear Generation of Light with Plasmonics," Science **333**, 1720 (2011).

[94] Bouhelier, A.; Beversluis, M.; Hartschuh, A.; Novotny, L., "Near-field second-harmonic generation induced by local field enhancement," Phys. Rev. Lett. **90**, 013903 (2003).

[95] Hajisalem, G.; Nezami, M. S.; Gordon, R., "Probing the Quantum Tunneling Limit of Plasmonic Enhancement by Third Harmonic Generation," Nano Lett. **14,** 6651—6654 (2014).

[96] Zhu, W.; Crozier, K. B., "Quantum mechanical limit to plasmonic enhancement as observed by surface-enhanced Raman scattering," Nature Communications **5,** 5228 (2014).

[97] Tan, S. F.; Wu, L.; Yang, J. K. W.; Bai, P.; Bosman, M.; Nijhuis, C. A., "Quantum Plasmon Resonances Controlled by Molecular Tunnel Junctions," Science **343,** 1496–1499 (2014).

[98] Esteban, R.; Aguirregabiria, G.; Borisov, A. G.; Wang, Y. M.; Nordlander, P.; Bryant, G. W.; Aizpurua, J., "The morphology of narrow gaps modifies the plasmonic response," ACS Photonics. **2,** 295-305 (2015).

[99] Zuloaga, J.; Prodan, E.; Nordlander, P., "Quantum Plasmonics: Optical Properties and Tunability of Metallic Nanorods," ACS Nano **4,** 5269 (2010).

[100] Teperik, T. V.; Nordlander, P.; Aizpurua, J.; Borisov, A. G., "Quantum effects and nonlocality in strongly coupled plasmonic nanowire dimers," Optics Express **21,** 27306-27325 (2013).

[101] Atay, T.; Song, J.-H.; Nurmikko, A. V., "Strongly Interacting Plasmon Nanoparticle Pairs: From Dipole-Dipole Interaction to Conductively Coupled Regime," Nano Lett. **4,** 1627 (2004).

[102] Marhaba, S.; Bachelier, G.; Bonnet, Ch.; Broyer, M.; Cottancin, E.; Grillet, N.; Lerme, J.; Vialle, J.-L.; Pellarin, M., "Surface plasmon resonance of single gold nanodimers near the conductive contact limit," J. Phys. Chem. C **113,** 4349 (2009).

[103] Schnell, M.; Garcia-Etxarri, A.; Huber, A. J.; Crozier, K.; Aizpurua, J.; Hillenbrand, R."Controlling the near-field oscillations of loaded plasmonic nanoantennas," Nature Photonics **3,** 287 (2009).

[104] Pérez-González, O.; Zabala, N.; Borisov, A. G.; Halas, N. J.; Nordlander, P.; Aizpurua, J., "Optical spectroscopy of conductive junctions in plasmonic cavities," Nano Lett. **10,** 3090 (2010).

[105] Pérez-González, O.; Zabala, N.; Aizpurua, J., "Optical characterization of charge transfer and bonding dimer plasmons in linked interparticle gaps," New J. Phys. **13,** 083013 (2011).

[106] Alvarez-Puebla, R.; Liz-Marzán, L. M.; García de Abajo, F. J., "Light concentration at the nanometer scale," J. Phys. Chem. Lett. **1,** 2428 (2010).

[107] David, C.; García de Abajo, F. J., "Spatial nonlocality in the optical response of metal nanoparticles," J. Phys. Chem. C **115,** 19470 (2011).

[108] Toscano, G.; Raza, S.; Jauho, A.-P.; Mortensen, N. A.; Wubs, M., "Modified field enhancement and extinction by plasmonic nanowire dimers due to nonlocal response," Optics Express **20,** 4176 (2012).

[109] Toscano, G.; Raza, S.; Xiao, S.; Wubs, M.; Jauho, A.-P.; Bozhevolnyi, S. I.; Mortensen, N. A., "Surface-enhanced Raman spectroscopy (SERS): nonlocal limitations," Opt. Lett. **37,** 2538 (2012).

[110] Luo, Y.; Fernandez-Dominguez, A. I.; Wiener, A.; Maier, S. A.; Pendry, J. B., "Surface Plasmons and Nonlocality: A Simple Model," Phys. Rev. Lett. **111,** 093901 (2013).

[111] Toscano, G.; Rockstuhl, C.; Evers, F.; Xu, H.; Mortensen, N. A.; Wubs, M.; "Self-consistent hydrodynamic approach to nanoplasmonics: Resonance shifts and spill-out effects," arXiv:1408.5862 [physics.optics].

[112] Jackson, J. D. "Classical electrodynamics," 3rd edition (Wiley, New York 1999).

[113] Gao, S.; Li, P.; Li, F., "Geometrical parameters controlled focusing and enhancing near field in infinite circular metal-dielectric multilayered cylinder," Appl. Phys. Lett. **102,** 123107 (2013).

[114] Hu, Y.; Flemming, R. C.; Drezek, R. A., "Optical properties of gold-silica-gold multilayer nanoshells," Optics Express **16,** 19579 (2008).

[115] Bardhan, R.; Mukherjee, S.; Mirin, N. A.; Levit, S. D.; Nordlander, P.; Halas, N. J., "Nanosphere-in-a-Nanoshell: A Simple Nanomatryoshka," J. Phys. Chem. C **114,** 7378–7383 (2010).

[116] Qian, J.; Wang, W.; Li, Y.; Xu, J.; Sun, Q., "Optical Extinction Properties of Perforated Gold-Silica-Gold Multilayer Nanoshells," J. Phys. Chem. C **116,** 10349–10355 (2012).

[117] Peña-Rodríguez, O.; Rivera, A.; Campoy-Quiles, M.; Pal, U., "Tunable Fano resonance in symmetric multilayered gold nanoshells," Nanoscale **5,** 209-216 (2013).

[118] Hsu, C. W.; DeLacy, B. G.; Johnson, S. G.; Joannopoulos, J. D.; Soljacic, M., "Theoretical Criteria for Scattering Dark States in Nanostructured Particles," Nano Letters **14,** 2783-2788 (2014).

[119] Ayala-Orozco, C.; Liu, J. G.; Knight, M. W.; Wang, Y.; Day, J. K.; Nordlander, P.; Halas, N. J., "Fluorescence Enhancement of Molecules Inside a Gold Nanomatryoshka," Nano Lett. **14,** 2926–2933 (2014).

[120] Román-Velázques, E.; Noguez, C., "Designing the plasmonic responce of shell nanoparticles: Spectral representation," J. Chem. Phys. **134,** 044116 (2011).

[121] Xu, H., "Multilayered metal core-shell nanostructures for inducing a large and tunable optical field," Phys. Rev. B **72,** 073405 (2005).

[122] Zhang, P.; Feist, J.; Rubio, A.; García-González, P.; García-Vidal, F. J., "Ab initio nanoplasmonics: The impact of atomic structure," Phys. Rev. B **90**, 161407(R) (2014).

[123] Yannouleas, C.; Vigezzi, E.; Broglia, R. A., "Evolution of the optical properties of alkali-metal microclusters towards the bulk: The matrix random-phase-approximation description," Phys. Rev. B **47,** 9849 (1993).

[124] Fennel,Th.; Meiwes-Broer, K.-H.; Tiggesbäumker, J.; Reinhard, P.-G.; Dinh, P. M.; Suraud, E., "Laser-driven nonlinear cluster dynamics", Rev. Mod. Phys. **82**, 1793-1842 (2010).

[125] Prodan, E.; Nordlander, P.; Halas, N. J., "Electronic Structure and Optical Properties of Gold Nanoshells," Nano Lett. **3,** 1411–1415 (2003).

[126] Prodan, E.; Nordlander, P.; Halas, N. J., "Effects of Dielectric Screening on the Optical Properties of Metallic Nanoshells," Chem. Phys. Lett. **368,** 94–101 (2003).

[127] Pitarke, J. M.; Silkin, V. M.; Chulkov, E. V.; Echenique, P. M., "Theory of surface plasmons and surface-plasmon polaritons," Rep. Prog. Phys. **70,** 1 (2007).

[128] Liebsch, A., "Surface-plasmon dispersion and size dependence of Mie resonance: Silver versus simple metals," Phys. Rev. B **48,** 11317 (1993).

[129] Marques, M. A. L.; Gross, E. K. U., "Time-Dependent Density Functional Theory," Ann. Rev. of Phys. Chem. **55,** 427 (2004).

[130] Gunnarson, O; Lundqvist, B. I., "Exchange and correlation in atoms, molecules, and solids by the spin-density-functional formalism," Phys. Rev. B **13,** 4274 (1976).

[131] Cottancin, E.; Celep, G.; Lermé, J.; Pellarin, M.; Huntzinger, J. R.; Vialle, J. L.; Broyer M. "Optical properties of noble metal clusters as function of the size: comparison between experiments and semi-quantal theory". Theor. Chem. Acc, **116,** 514, 2006.

[132] Hövel, H.; Fritz, S.; Hilger, A.; Kreibig, V; Vollmer, M., "Width of cluster plasmon resonances: Bulk dielectric functions and chemical interface damping," Phys. Rev. B **48,** 18178 (1993).

[133] Apell, P.; Penn, D. R., "Optical Properties of Small Metal Spheres: Surface Effects," Phys. Rev. Lett. **50,** 1316 (1983).

[134] Apell,P.; Ljungbert, Å., "Red shift of surface plasmons in small metal particles," Solid State Commun. **44,** 1367 (1982).

[135] Haberland, H. "Looking from both sides," Nature **494,** E1–E2 (2013).

[136] Hentschel, M.; Dregely, D.; Vogelgesang, R.; Giessen, H.; Liu, N., "Plasmonic Oligomers: The Role of Individual Particles in Collective Behavior," ACS Nano **5,** 2042 (2011).

[137] Ye, J.; Van Dorpe, P. "Plasmonic behaviors of gold dimers perturbed by a single nanoparticle in the gap." Nanoscale, **4**, (22), 7205-7211, 2012.

[138] Ye, J.; Wen, F. F.; Sobhani, H.; Lassiter, J. B.; Van Dorpe, P.; Nordlander, P.; Halas, N. J. "Plasmonic Nanoclusters: Near Field Properties of the Fano Resonance Interrogated with SERS. " Nano Lett., **1**2 (3), 1660-1667, 2012.

[139] Wen, F.; Ye, J.; Liu, N.; Van Dorpe, P.; Nordlander, P.; Halas, N. J. "Plasmon Transmutation: Inducing New Modes in Nanoclusters by Addling Dielectric Nanoparticles." Nano Lett, **1**2 (9), 5020-5026, 2012.

[140] Tame, M.; McEnery, K.; Ozdemir, S.; Lee, J.; Maier, S.; Kim, M. "Quantum plasmonics." Nat. Phys, **9** (6), 329-340, 2013.

[141] Wu, L.; Duan, H.; Bai, P.; Bosman, M.; Yang, J. K.; Li, E. "Fowler–Nordheim tunneling induced charge transfer plasmons between nearly touching nanoparticles". ACS Nano, **7** (1), 707-716, 2012

[142] Ciraci, C.; Hill, R.; Mock, J.; Urzhumov, Y.; Fernández-Domínguez, A.; Maier, S.; Pendry, J.; Chilkoti, A.; Smith, D. "Probing the ultimate limits of plasmonic enhancement". Science, **337** (6098), 1072-1074, 2012.

[143] Gandra, N.; Singamaneni, S. "Bilayered Raman Intense Gold Nanostructures with Hidden Tags (BRIGHTs) for High Resolution Bioimaging". Adv. Mater, **25** (7), 1022-1027, 2013.

[144] Lim, D.-K.; Jeon, K.-S.; Hwang, J.-H.; Kim, H.; Kwon, S.; Suh, Y. D.; Nam, J.-M. "Highly uniform and reproducible surface-enhanced Raman scattering from DNA-tailorable nanoparticles with 1-nm interior gap". Nat. Nanotechnol, **6** (7), 452-460, 2011.

[145] Oldenburg, S. J.; Averitt, R. D.; Westcott, S. L.; Halas, N. J. " Nanoengineering of optical resonances". Chem. Phys. Lett, **288** (2-4), 243-247, 1998.

[146] Nehl, C. L.; Grady, N. K.; Goodrich, G. P.; Tam, F.; Halas, N. J.; Hafner, J. H. "Scattering spectra of single gold nanoshells". Nano Lett, **4** (12), 2355-2359, 2004.

[147] Li, J. F.; Huang, Y. F.; Ding, Y.; Yang, Z. L.; Li, S. B.; Zhou, X. S.; Fan, F. R.; Zhang, W.; Zhou, Z. Y.; Wu, D. Y. "Shell-isolated nanoparticle-enhanced Raman spectroscopy". Nature, **464** (7287), 392-395, 2010

[148] Reed, M. A.; Zhou, C.; Muller, C.; Burgin, T.; Tour, J. "Conductance of a molecular junction". Science, **278** (5336), 252-254, 1997.

[149] Nitzan, A.; Ratner, M. A. "Electron transport in molecular wire junctions". Science, **300** (5624), 1384-1389, 2003.

[150] Tao, N. "Electron transport in molecular junctions". Nat. Nanotechnol, **1** (3), 173-181, 2006.

[151] Reddy, P.; Jang, S.-Y.; Segalman, R. A.; Majumdar, A. "Thermoelectricity in molecular junctions". Science, **315** (5818), 1568-1571, 2007.

[152] Xiao, X.; Xu, B.; Tao, N. J. "Measurement of single molecule conductance: Benzenedithiol and benzenedimethanethiol". Nano Lett, **4** (2), 267-271, 2004.

[153] Tsutsui, M.; Taniguchi, M.; Kawai, T. "Atomistic Mechanics and Formation Mechanism of Metal-Molecule-Metal Junctions". Nano Lett, **9** (6), 2433-2439, 2009.

[154] Strange, M.; Rostgaard, C.; Häkkinen, H.; Thygesen, K. S. "Self-consistent GW calculations of electronic transport in thiol and amine linked molecular junctions". Phys. Rev. B, **83** (11), 115108, 2011.

[155] Pontes, R. B.; Rocha, A. R.; Sanvito, S.; Fazzio, A.; da Silva, A. J. R. " Ab initio calculations of structural evolution and conductance of benzene-1, 4-dithiol on gold leads". ACS Nano, **5** (2), 795-804, 2011.

[156] Venkataraman, L.; Klare, J. E.; Nuckolls, C.; Hybertsen, M. S.; Steigerwald, M. L. "Dependence of single-molecule junction conductance on molecular conformation". Nature, **442** (7105), 904-907, 2006.

[157] Kiguchi, M.; Nakamura, H.; Takahashi, Y.; Takahashi, T.; Ohto, T. " Effect of anchoring group position on formation and conductance of a single disubstituted benzene molecule bridging Au electrodes: change of conductive molecular orbital and electron pathway". The Journal of Physical Chemistry C, **114** (50), 22254-22261, 2010.

[158] Kim, Y.; Pietsch, T.; Erbe, A.; Belzig, W.; Scheer, E. "Benzenedithiol: A broad-range single-channel molecular conductor." Nano Lett, **11** (9), 3734-3738, 2011.

[159] Benz, F.; Tserkezis, C.; Herrmann, L. O.; de Nijs, B.; Sanders, A.; Sigle, D. O.; Pukenas, L.; Evans, S. D.; Aizpurua, J.; Baumberg, J. J. "Nanooptics of Molecular-Shunted Plasmonic Nanojunctions". Nano Lett, **15** (1), 669-674, 2015.

[160] Love, J. C.; Estroff, L. A.; Kriebel, J. K.; Nuzzo, R. G.; Whitesides, G. M. "Self-assembled monolayers of thiolates on metals as a form of nanotechnology". Chemical reviews, **105** (4), 1103-1170, 2005.

[161] Garcia de Abajo, F. J.; Howie, A. "Retarded field calculation of electron energy loss in inhomogeneous dielectrics". Phys. Rev. B, **65** (11), 115418, 2002.

[162] Baer, R.; Seideman, T.; Ilani, S.; Neuhauser, D. "Ab initio study of the alternating current impedance of a molecular junction". The Journal of chemical physics, **120** (7), 3387-3396, 2004.

[163] Keller, A.; Atabek, O.; Ratner, M.; Mujica, V. "Laser-assisted conductance of molecular wires". Journal of Physics B: Atomic, Molecular and Optical Physics, **35** (24), 4981, 2002.

[164] Song, P.; Meng, S.; Nordlander, P.; Gao, S. "Quantum plasmonics: Symmetry-dependent plasmon-molecule coupling and quantized photoconductances". Phys. Rev. B, **86** (12), 121410, 2012.

[165] Ye, J.; Chen, C.; Lagae, L.; Maes, G.; Borghs, G.; Van Dorpe, P. "Strong location dependent surface enhanced Raman scattering on individual gold semishell and nanobowl particles". Physical Chemistry Chemical Physics, **12** (37), 11222-11224, 2010.

[166] Park, W.-H.; Kim, Z. H. "Charge transfer enhancement in the SERS of a single molecule". Nano Lett, **10** (10), 4040-4048, 2010.

[167] Matsuhita, R.; Horikawa, M.; Naitoh, Y.; Nakamura, H.; Kiguchi, M. "Conductance and SERS Measurement of Benzenedithiol Molecules Bridging Between Au Electrodes". The Journal of Physical Chemistry C, **117** (4), 1791-1795, 2013.

[168] Stewart, M. E., Anderton, C. R., Thompson, L. B., Maria, J., Gray, S. K., Rogers, J. A. & R. G. Nuzzo. "Nanostructured Plasmonic Sensors." Chem. Rev. **108**, 494–521 (2008).

[169] Gonçalves, M. R. "Plasmonic nanoparticles: fabrication, simulation and experiments." J. Phys. D: Appl. Phys. **47**, 213001 (2014).

[170] Jones, M. R., Osberg, K. D., Macfarlane, R. J., Langille, M. R. & Mirkin, C. A. "Templated techniques for the synthesis and assembly of plasmonic nanostructures." Chem. Rev. **111**, 3736–3827 (2011).

[171] Lindquist, N. C., Nagpal, P., McPeak, K. M., Norris, D. J. & Oh, S.-H. "Engineering metallic nanostructures for plasmonics and nanophotonics." Rep. Prog. Phys. **75**, 036501 (2012).

[172] Aksu, S., Huang, M., Artar, A., Yanik, A. A., Selvarasah, S., Dokmeci, M. R. & Altug, H. "Flexible plasmonics on unconventional and nonplanar substrates." Advanced Materials **23**, 4422–4430 (2011).

[173] Pala, R. A., Shimizu, K. T., Melosh, N. A. & Brongersma, M. L. "A nonvolatile plasmonic switch employing photochromic molecules." Nano Lett. **8**, 1506–1510 (2008).

[174] Zheng, Y. B., Yang, Y.-W., Jensen, L., Fang, L., Juluri, B. K., Flood, A. H., Weiss, P. S., Stoddart, J. F. & Huang, T. J. "Active molecular plasmonics: controlling plasmon resonances with molecular switches." Nano Lett. **9**, 819–825 (2009).

[175] Nikolajsen, T., Leosson, K. & Bozhevolnyi, S. I. "Surface plasmon polariton based modulators and switches operating at telecom wavelengths." Appl. Phys. Lett. **85**, 5833–5835 (2004).

[176] Ju, L., Geng, B., Horng, J., Girit, C., Martin, M., Hao, Z., Bechtel, H. A., Liang, X., Zettl, A., Ron Shen, Y. & Wang, F. "Graphene plasmonics for tunable terahertz metamaterials." Nature Nanotechnology **6**, 630–634 (2011).

[177] Koppens, F. H. L., Chang, D. E. & García de Abajo, F. J. "Graphene plasmonics: a platform for strong light–matter interactions." Nano Lett. **11**, 3370–3377 (2011).

[178] Manjavacas, A. & García de Abajo, F. J. "Tunable plasmons in atomically thin gold nanodisks." Nature Communications **5**, 3548 (2014).

[179] Li-Hua, S. et al, "Electrochemical Modulation of Photonic Metamaterials", Adv. Mater. **22**, 5173-5177 (2010)

[180] Dondapati, S. K. et al. "Voltage-Induced Adsorbate Damping of Single Gold Nanorod Plasmons in Aqueous Solution", Nano Lett. **12**, 1247-1252 (2012)

[181] Novo, C.; Funston,A. M.; Gooding, A. K.; Mulvaney, P., "Electrochemical Charging of Single Gold Nanorods," J. Am. Chem. Soc. **131**, 14664-14666 (2009)

[182] Kravtsov, V., Berweger, S., Atkin, J. M. & Raschke, M. B. "Control of plasmon emission and dynamics at the transition from classical to quantum coupling." Nano Lett. **14** (9), 5270-5275 (2014).

[183] Scholl, J. A.; García-Etxarri, A.; Koh, A. L.; Dionne, J. A.; "Observation of Quantum Tunneling between Two Plasmonic Nanoparticles", Nano Lett. **13**, 564–569 (2013)

[184] Simmons, J. G. "Generalized formula for the electric tunnel effect between similar electrodes separated by a thin insulating film." J. Appl. Phys. **34**, 1793-1803 (1963).

[185] Pitarke, J. M.; Flores, F.; & Echenique, P. M., "Tunneling spectroscopy: surface geometry and interface potential effects." Surf. Sci. **234**, 1–16 (1990).

[186] Garcia-Lekue, A.; Sánchez-Portal, D.; Arnau, A; Wang, L. W. "Plane-wave based electron tunneling through field emission resonance states." Phys. Rev. B **88**, 155441 (2013).

[187] Casida, M. E. "Journal of Molecular Structure": THEOCHEM **914**, 3–18 (2009).

[188] Marques, M. A. L. & Gross, E. K. U. "Time-dependent density functionl theory." Ann. Rev. Phys. Chem. **55**, 427–455 (2004).

[189] Quijada, M.; Borisov, A. G.; Nagy, I.; Diez Muiño, R.; and Echenique, P. M. "Time-dependent density-functional calculation of the stopping power for protons and antiprotons in metals", Phys. Rev. A **75**, 042902 (2007).

[190] Burke, K.; Werschnik, J.; & Gross, E. K. U., "Time-dependent density functional theory: past, present, and future." J. Chem. Phys. **123**, 062206 (2005).

[191] Gunnarsson, O. and Lundqvist, B. I., "Exchange and correlation in atoms, molecules, and solids by the spin-density-functional formalism", Phys. Rev. B **13**, 4274 (1976).

[192] Borisov, A. G.; Gauyacq, J. P.; Shabanov, S. V., "Wave packet propagation study of the charge transfer interaction in the F-Cu (111) and–Ag (111) systems", Surf. Sci. **487** (1), 243–257 (2001).

[193] Chulkov, E. V.; Borisov, A. G.; Gauyacq, J. P.; Sánchez-Portal, D.; Silkin, V. M.; Zhukov, V. P.; Echenique, P. M., "Electronic excitations in metals and at metal surfaces", Chem. Rev. **106** (10), 4160–4206 (2006).

[194] Barbry, M.; Koval, P.; Marchesin, F.; Esteban, R.; Borisov, A. G.; Aizpurua, J; Sánchez-Portal, D., "Atomistic near-field nanoplasmonics: reaching atomic-scale resolution in nanooptics". Nano Lett., Articles ASAP (As Soon As Publishable), Publication Date (Web): April 27, 2015 (Letter), DOI: 10.1021/acs.nanolett.5b00759

[195] Reiners, Th.; Haberland, H. "Plasmon Enhanced Electron and Atom Emission from a Spherical Sodium Cluster: Na_{91}", Phys. Rev. Lett. **77**, 2440 (1996)

[196] Lermé, J., "Size Evolution of the Surface Plasmon Resonance Damping in Silver Nanoparticles: Confinement and Dielectric Effects," J. Phys. Chem. C **115** (29), 14098-14110 (2011).

[197] Kurth S., *Fundamentals of Time-Dependent Density Functional Theory, Lecture Notes in Physics*, Eds. Marques, M. A. L., Maitra, N., Nogueira, F., Gross, E. K. U. & Rubio, A. Springer Vol. 837, (2012).

[198] Cini, M. "Time-dependent approach to electron transport through junctions: General theory and simple applications." Phys. Rev. B **22**, 5887 (1980).

[199] Evans, J. S. & Van Voorhis, T. "Dynamic current suppression and gate voltage response in metal-molecule-metal junctions." Nano Lett. **9**, 2671–2675 (2009).

[200] Tucker, J. R. & Feldman, M. J. "Quantum detection at millimeter wavelengths." Rev. Mod. Phys. **57**, 1055–1113 (1985).

[201] Pedersen, M. H. & Büttiker, M. "Scattering theory of photon-assisted electron transport." Phys. Rev. B **58**, 12993 (1998).

[202] Kaasbjerg, K. & Nitzan, A. "Theory of light emission from quantum noise in plasmonic contacts: above-threshold emission from higher-order electron-plasmon scattering." Phys. Rev. Lett. **114**, 126803 (2015).

[203] Boardman, A. D.; Grimalsky, V. V.; Kivshar, Y. S.; Koshevaya, S. V.; Lapine, M.; Litchinitser, N.M.; Malnev, V. N.; Noginov, M.; Rapoport, Y. G.; and Shalaev, V. M. "Active and tunable metamaterials. " Laser Photon. Rev. **10**, 00012 (2010).

[204] Liu, A. Q.; Zhu, W. M.; Tsai, D. P.; and Zheludev, N. I. "Micromachined tunable metamaterials: a review. " J. Opt. **14**, 114009 (2012).

[205] Chu, K. C.; Chao, C. Y.; Chen, Y. F.; Wu, Y. C; Chen, C. C. "Electrically controlled surface plasmon resonance frequency of gold nanorods." Appl. Phys. Lett. **89**, 103107 (2006).

[206] Mulvaney, P.; Pérez-Juste, J.; Giersig, M.; Liz-Marzán, L. M; Pecharromán, C., "Drastic surface plasmon mode shifts in gold nanorods due to electron charging" Plasmonics **1**, 61-66 (2006).

[207] Mulvaney. P "Surface plasmon spectroscopy of nanosized metal particles." Langmuir **12** 788 (1996)

[208] Henglein, A.; Mulvaney, P.; Linnert, T., "Chemistry of Agn Aggregates in Aqueous-Solution-Nonmetallic Oligomeric Clusters and Metallic Particles." Faraday Discuss **92** 31 (1991)

[209] Henglein, A.; Meisel, D. "Radiolytic Control of the Size of Colloidal Gold Nanoparticles." Langmuir **14** 7392 (1998)

[210] Lapsley, M. I.; Shahravan, A.; Hao, Q.; Juluri, B. K.; Giardinelli, S.; Lu, M.; Zhao, Y.; Chiang, I-K.; Matsoukas, T.; Huang, T. J.; "Shifts in plasmon resonance due to charging of a nanodisk array in argon plasma"; Appl. Phys. Lett. **1**00, 101903 (2012)

[211] Ung, T.; Giersig, M.; Dunstan, D.; Mulvaney, P.; "Spectroelectochemistry of Colloidal Silver." Langmuir **13** 1773 (1997)

[212] Jablan, M.; Buljan, H.; Soljacic, M., "Plasmonics in graphene at infrared frequencies." Phys. Rev. B **80**, 245435 (2009).

[213] Koppens, F. H. L.; Chang, D. E.; García de Abajo, F. J., "Graphene plasmonics: a platform for strong light-matter interactions". Nano Lett. **11**, 3370-3377 (2011).

[214] Fang, Z.; Thongrattanasiri, S.; Schlather, A.; Liu, Z.; Ma, L.; Wang, Y.; Ajayan, P. M.; Nordlander, P.; Halas, N. J.; García de Abajo, F. J., "Gated tunability and hybridization of localized plasmons in nanostructured graphene." ACS Nano **7**, 2388-2395 (2013).

[215] Brack, M. "The physics of simple metal clusters: self-consistent jellium model and semiclassical approaches", Rev. Mod. Phys. **65**, 677 (1993)

[216] de Heer, W. A. "The physics of simple metal clusters: experimental aspects and simple models" Rev. Mod. Phys. **65**, 611 (1993)

[217] Baletto, F.; Ferrando, R., "Structural properties of nano clusters: Energetic, thermodynamic, and kinetic effects", Rev. Mod. Phys. **77,** 371 (2005)

[218] Chulkov, E. V.; Silkin, V. M.; Echenique, P. M., "Image potential states on metal surfaces: binding energies and wave functions", Surf. Sci. **437**, 330-352 (1999).

[219] Perdew, J. P.; Tran, H. Q.; Smith, E. D., "Stabilized jellium: Structureless pseudopotential model for the cohesive and surface properties of metals", Phys. Rev. B **42,** 11627 (1990)

[220] Kohn, W.; Sham, L. J., "Self-Consistent Equations Including Exchange and Correlation Effects", Phys. Rev. **140**, A1133-A1138 (1965)

[221] Köller, L.; Schumacher, M.; Köhn, J.; Teuber, S.; Tiggesbäumker, J.; Meiwes-Broer, K. H., "Plasmon-Enhanced Multi-Ionization of Small Metal Clusters in Strong Femtosecond Laser Fields", Phys. Rev. Lett. **82**, 3783 (1999)

[222] Fennel, T.; Bertsch, G. F.; Meiwes-Broer, K.-H. "Ionization dynamics of simple metal clusters in intense fields by the Thomas-Fermi-Vlasov method", Eur. Phys. J. D **29**, 367—378 (2004)

[223] Fennel, Th.; Meiwes-Broer, K.-H.; Tiggesbäumker, J.; Reinhard, P.-G.; Dinh, P. M.; Suraud, E., "Laser-driven nonlinear cluster dynamics" Rev. Mod. Phys. **82**, 1793 (2010)

[224] Tiggesbäumker, J.; Köller, L.; Meiwes-Broer, K.-H., "Bound-free collective electron excitations in negatively charged silver clusters". Chem. Phys. Lett. **260**, 428 (1996)

[225] Schmitt, Ch.; Ellert, Ch.; Schmidt, M.; Haberland, H., "Doubly charged sodium clusters: plasmon response and photoproduction", Zeitschrift für Physik D Atoms, Molecules and Clusters **42**, 145–152 (1997)

[226] Dam, N.; Saunders, W. A., "Surface-plasmon absorption in singly and doubly charged potassium clusters", Phys. Rev. B **46**, 4205 (1992)

[227] Rubio, A.; Balbas, L. C.; Alonso, J. A.; "Influence of nonlocal exchange-correlation effects on the response properties of simple metal clusters". Phys. Rev. B **46**, 4891 (1992)

[228] Yannouleas, C., "Microscopic description of the surface dipole plasmon in large Na_N clusters ($950 \leq N \leq 12050$) Phys. Rev. B **58**, 6748 (1998)

[229] Pacheco, J. M.; Ekardt, W., "A new formulation of the dynamical response of many-electron systems and the photoabsorption cross section of small metal clusters", Zeitschrift für Physik D Atoms, Molecules and Clusters **24**, 65–69 (1992)

[230] Apell, P.; Penn, D. R., "Optical properties of small metal spheres: surface effects, " Phys. Rev. Lett. **50**, 1316–1319 (1983)

[231] Apell, P; Ljungbert, Å., "Red shift of surface plasmons in small metal particles", Solid State Commun. **44**, 1367–1369 (1982)

[232] Liebsch, A., "Surface-plasmon dispersion and size dependence of Mie resonance: silver versus simple metals, " Phys. Rev. B **48**, 11317-–11328 (1993)

[233] Manjavacas, A.; Liu, J. G.; Kulkarni, V.; Nordlander, P., "Plasmon-Induced Hot Carriers in Metallic Nanoparticles", ACS Nano **8**, 7630-7638 (2014)

[234] Buck, B.; Merchant, A. C.; Perez, S. M., "Ground state to ground state alpha decays of heavy even-even nuclei", J. Phys. G: Nucl. Part. Phys. **17**, 1223–1235 (1991)

[235] Nakazato, H.; Namiki, M.; Pascazio, S., "Temporal Behaviour of Quantum Mechanical Systems", Int. J. Mod. Phys. B **10**, 247 (1996)

[236] Daniels, J. K.; Chumanov, G., "Spectroelectrochemical studies of plasmon coupled silver nanoparticles", Journal of Electroanalytical Chemistry **575**, 203–209 (2005)

[237] König, T. A. F.; Ledin, P. A.; Kerszulis, J.; Mahmoud, M. A.; El-Sayed, M. A.; Reynolds, J. R.; Tsukruk, V. V., "Electrically Tunable Plasmonic Behavior of Nanocube–Polymer Nanomaterials Induced by a Redox-Active Electrochromic Polymer", ACS Nano **8**, 6182-6192 (2014)

[238] Mogensen, K. B.; Kneipp, K., "Size-Dependent Shifts of Plasmon Resonance in Silver Nanoparticle Films Using Controlled Dissolution: Monitoring the Onset of Surface Screening Effects". J. Phys. Chem. C **118**, 28075–28083 (2014)

Abbreviations

AC	**A**lternating **C**urrent
BEM	**B**oundary **E**lement **M**ethod
CNM	**C**ylindrical **N**ano **M**atryoshka
CT	**C**harge **T**ransfer
DC	**D**irect **C**urrent
DM	**D**rude **M**odel
EFF-EF	**E**nhancement **F**ield **F**actor
FEM	**F**inite **E**lement **M**ethod
HDM	**H**ydro **D**ynamic **M**odel
JM	**J**ellium **M**odel
LSP	**L**ocalized **S**urface **P**lasmon
LSPP	**L**ocalized **S**urface **P**lasmon **P**olariton
LSPR	**L**ocalized **S**urface **P**lasmon **R**esonance
ME	**M**axwell **E**quations
NM	**N**ano **M**atryoshka
NP	**N**ano **P**article
NPD	**N**ano **P**article **D**imer
PH	**P**lasmon **H**ybridization
QCM	**Q**uantum **C**orrected **M**odel
SERS	**S**urface **E**nhanced **R**aman **S**pectroscopy
TDDFT	**T**ime **D**ependent **D**ensity **F**unctional **T**heory
WKB	**W**entzel **K**ramers **B**rillouin **A**pproximation

List of publications

The articles published (or in preparation) during the period of this thesis are listed below:

Regular papers

1. "Quantum effects in the optical response of extended plasmonic gaps: validation of the quantum corrected model in core-shell nanomatryushkas" Zapata, M., Beltran, A. S. C., Borisov, A. G., Aizpurua, J. Opt. Express 2015,**23**, 8134-8149.

2. "Nanooptics of Plasmonic Nanomatryoshkas: Shrinking the Size of a Core-Shell Junction to Subnanometer." Lin. L, Zapata. M, Xiong. M, Liu. Z, Wang. S, Xu. H, Borisov. A. G., Gu. H, Nordlander. P, Aizpurua. J, and Jian Ye. Nano Lett., 2015, **15** (10), pp 6419–6428 [1]

3. "Active Quantum Plasmonics." D. C. Marinica, M. Zapata, P. Nordlander, A. K. Kazansky, P. M. Echenique, J. Aizpurua, A. G. Borisov. Sci. Adv.**1**, e1501095 (2015).

4. "Quantum Plasmonics and charged cluster dynamics." Zapata. M, Borisov. A. G, Kazanski. A. K. and Aizpurua. J. Submitted to Langmuir.

5. "Size change effect on the optical behavior of ultra small metal particles." Mario Zapata Herrera and Angela S. Camacho B. In preparation.

[1] Contribution equally to this work as first author.

6. “Quantum confinement effects on the dielectric function and near field enhancement in metallic nanoparticles”. M. Zapata Herrera, J. Florez, A. S. Camacho and H. Y. Ramirez. In preparation.

Divulgative papers:

1. “Plasmónica en el régimen subnanométrico”. Angela Camacho y Mario Zapata Herrera. Revista Digital Universitaria. 1 de septiembre de 2015, Vol. 16, Núm. 9. http://www.revista.unam.mx/vol.16/num9/art72/

Conferences

1. “Study of the geometrical dependence of plasmonics resonances Using Finite-Difference Time-Domain Method (FDTD)”. M. Zapata, J. C. Arias, A. Camacho and H. Garcia. XII Encuentro Nacional de Óptica y III Conferencia Andina y del Caribe en Óptica y sus Aplicaciones. Universidad del Atlántico, Barranquilla. September 5-9/2011.

2. “Artificial Plasmonic Molecules”. M. Zapata Herrera and A. Camacho. Nanosmat USA 2012. Tampa, Florida USA. March 2012.

3. “Quantum plasmon resonances and coupling of small nanoparticles”. M. Zapata-Herrera and A. Camacho. APS March Meeting 2013. Baltimore, Maryland, USA. March 2013.

4. “Localized Surface Plamons in very small nanoparticles”. 14th Conference on Physics of Light-Matter Coupling in Nanostructures. Hersonissos, Crete, Greece. May 2013.

5. “Effect of the confinement potential on the Localized Surface Plasmon Resonance of metallic small nanoparticles”. M. Zapata Herrera, J. Florez and A. Camacho. Semana de la Nanociencia y la Nanotecnología en Colombia Nanoantioquia 2013. Medellin, Colombia. Julio de 2013.

6. “Finite potential and nonlinear contribution effects in the Localized Surface Plasmon Resonances (LSPR) of small metallic nanoparticles”. M. Zapata Herrera and A. Camacho. XXV Congreso nacional de Física. Armenia, Colombia. Agosto de 2013.

Scientific visits

- Centro de Física de Materiales and Donostia International Physics Center, Universidad del País Vasco, Spain. May-August 2014.
- Universitè Paris Sud, France. September-December 2014.
- Centro de Física de Materiales and Donostia International Physics Center, Universidad del País Vasco, Spain. May-August 2015.
- Centro de Física de Materiales and Donostia International Physics Center, Universidad del País Vasco, Spain. November-December 2015.


UNIVERSITÉ
PARIS
SUD

ismo
Institut des sciences moléculaires d'Orsay

CFM
Materials Physics Center
Centro de Física de Materiales

COLCIENCIAS
COLOMBIA

Universidad de
los Andes